Role of Osteopontin in Right Ventricular Remodeling

Inaugural Dissertation

submitted to the

Faculty of Medicine in partial fulfillment of the requirements

for the PhD-Degree of the Faculties of Veterinary Medicine and

Medicine of the Justus Liebig University Giessen

by

Mamazhakypov, Argen

Of

Osh, Kyrgyzstan

Giessen 2019

From the Cardio-Pulmonary Institute (CPI) and Department of Pulmonary Pharmacotherapy

Director/Chairman: Prof. Dr. Ralph Schermuly

Faculty of Medicine of the Justus Liebig University Giessen

First Supervisor and Committee Member: Prof. Dr. Ralph Schermuly

Second Supervisor and Committee Member: Prof. Dr. Joachim Roth

Committee member (Chair): Prof. Dr. Klaus-Dieter Schlüter

Committee member: Prof. Dr. Ralf Kinscherf

Date of Doctoral Defense: 09.12.2019

1 TABLE OF CONTENTS

2 LIST OF TABLES

3 LIST OF FIGURES

LIST OF FIGURES

4 ABBREVIATIONS

Ang-II	Angiotensin-II
ANP	Atrial natriuretic peptide
BNP	Brain natriuretic peptide
CI	Cardiac index
CO	Cardiac output
Col1	Collagen 1
Col3	Collagen 3
COPD	Chronic obstructive pulmonary disease
DAPI	4',6-diamidino-2-phenylindole
ECG	Electrocardiogram
ECM	Extracellular matrix
ECs	Endothelial cells
EF	Ejection fraction
ET-1	Endothelin-1
HR	Heart rate
HOX	Hypoxia
IL	Interleukin
ITGA	Integrin alpha
ITGB	Integrin beta
LV	Left ventricle
LVEDP	Left ventricular end diastolic pressure
LVOT	Left ventricular outflow tract
LVOTd	Left ventricular outflow tract diameter
LVSP	Left ventricular systolic pressure
MCT	Monocrotaline
OPN	Osteopontin
O_2	Oxygen

ABBREVIATIONS

PAB	Pulmonary artery banding
PAH	Pulmonary arterial hypertension
PASMCs	Pulmonary artery smooth muscle cells
PAFBs	Pulmonary artery fibroblasts
PH	Pulmonary hypertension
PVR	Pulmonary vascular resistance
RA	Right atrium
ROS	Reactive oxygen species
rOPN	Recombinant osteopontin
RHC	Right heart catheterization
RV	Right ventricle
RVEDP	Right ventricular end diastolic pressure
RVID	Right ventricular internal dimension
RVOT	Right ventricular outflow tract
RVOTd	Right ventricular outflow tract diameter
RVSP	Right ventricular systolic pressure
RV S´	Right ventricular annulus systolic velocity
RVWT	Right ventricular wall thickness
S	Septum
SPP1	Secreted phosphoprotein 1
SU5416	1,3-dihydro-3-[(3,5-dimethyl-1H-pyrrol-2-yl) methylene]-2H-indol-2-one
SuHx	SU5416/hypoxia
TAPSE	Tricuspid annular plane systolic excursion
TDI	Tissue doppler imaging
TGF-β	Transforming growth factor-β
TL	Tibial Length
TNF-α	Transforming growth factor alpha
VEGFR2	Vascular endothelial growth factor receptor 2
VTI	Velocity time integral

5 INTRODUCTION

5.1 Pulmonary circulation and the right ventricle

5.1.1 Pulmonary vasculature and physiology

Pulmonary circulation represents low resistance, and low pressure system, anatomically consisting of pulmonary arteries, complex peri-alveolar network of capillaries and pulmonary venous vessels, connected in series, providing large surface area for accommodating large blood volume and gas exchange [1].

The anatomy and function of the pulmonary vascular system differs from the systemic circulation because the primary purpose of the pulmonary circulation is fundamentally different from the systemic circulation. Specifically, arterial vessels of the systemic circulation are designed to deliver nutrient- and oxygen-rich arterial blood to the tissues; while, pulmonary arteries are designed to saturate deoxygenated venous blood with alveolar oxygen that is eventually delivered to the peripheral tissues of the body *via* systemic circulation.

Pulmonary circulation receives entire right ventricular (RV) cardiac output (CO) during each cardiac cycle and delivers deoxygenated venous blood to the alveolar capillary system *via* the pulmonary artery tree for the gas exchange. Despite the enormous blood volume present in the pulmonary vasculature, the pulmonary circulation maintains a low pressure and a low resistance blood flow. These hemodynamic effects prevent fluid flux from the pulmonary capillaries into the pulmonary interstitial space. Another specific property of the pulmonary vasculature is that hypoxia causes pulmonary artery smooth muscle cell (PASMC) contraction leading to hypoxic pulmonary vasoconstriction (HPV), whereas hypoxia dilates the arterioles of the systemic circulation due to relaxation of smooth muscle cells. These and other hemodynamic properties of the pulmonary circulation are based partly on its unique anatomical structure as compared to the systemic circulation. While, the arterial tree of systemic circulation consists of a main artery with side branches, the pulmonary arterial tree resembles a system of short vessels continuously branching into several generations until forms extensive network of peri-alveolar capillaries [2, 3].

5.1.2 Right ventricular anatomy and function

Right ventricle (RV) is embryologically, morphologically, and functionally distinct from left ventricle (LV) [4]. Embryologically, the RV and LV develop from different origins. Specifically, the LV develops first, originating from the primary heart field; subsequently the RV develops from precursors cells in the secondary heart field [5]. Moreover, chamber-specific cardiomyocyte differentiation from myoblasts are also controlled with specific set of transcription factors. For example, RV cardiomyocyte differentiation is controlled by transcription factors, such as dHAND and MEF2C2; while, LV cardiomyocyte development is guided by Nkx2.5 and eHAND1 [6, 7].

Structurally, the shape of the RV is triangular when viewed from the side in longitudinal-section and crescentic when viewed in cross-section with a thin wall, as compared to the elliptically shaped concentric LV with thick walls [8]. The RV mass is only about one third of the LV mass, resulting in lower oxygen consumption of the RV myocardium [9]. Anatomically, the RV can be divided into 3 parts: (1) the inlet consisting of the tricuspid valve, chordae tendineae, and papillary muscles; (2) the trabeculated apical myocardium; and (3) the infundibulum, which is myocardial outflow region [9]. In addition, the RV structure is divided into two functionally distinct compartments, namely the sinus and the conus. The RV contraction starts with pressure generation in the sinus with a peristaltic motion that starts at the apex and moves toward the conus. In turn, the conus regulates the pressure, resulting in low pressure blood flow into the pulmonary arteries [8].

Functionally, the RV performs approximately ¼ of the cardiac stroke work overcoming pulmonary vascular resistance, which is 10-fold lower compared to that of the systemic circulation [10]. The RV ejection fraction (EF) in healthy individuals is slightly lower compared to that of the LV, while RV volume is slightly larger, resulting in similar RV and LV cardiac output. Moreover, RV is highly compliant with the prolonged peak pressure. Similarly, the RV elastance is also high. These properties of RV enable it to display an immense adaptive capacity in response to volume overload being able to increase its contractility for up to 4 to 5-fold as compared left ventricular (LV); while, RV less tolerant to the pressure overload than the LV [11, 12].

5.2 Pulmonary hypertension and right ventricular remodeling

5.2.1 Pulmonary hypertension

Pulmonary hypertension (PH) is a severe disease of the pulmonary vasculature characterized by extensive pulmonary artery remodeling due to excessive proliferation of pulmonary arterial cells such as pulmonary artery smooth muscle cells (PASMCs), adventitial fibroblasts (PAFBs) and pericytes, increased apoptosis of pulmonary artery endothelial cells (PAECs), deposition of extracellular matrix (ECM) as well as infiltration of the PA wall with various inflammatory/immune cells [13]. Hemodynamically, PAH is manifested with an increase in mean pulmonary arterial pressure (PAPm) $\geqslant$ 25 mmHg at rest as assessed by right heart catheterization (RHC) [14]. Despite extensive research in this field, the mechanisms underlying the pathogenesis of PH remain incompletely understood. However, several pathological processes have been shown to contribute to the pathobiology of PH including genetic predisposition [15], altered metabolism [16, 17], dysregulated apelin signaling [18], calcium signaling [19], DNA damage [20], mitochondrial dysfunction [21], and dysregulation of micro RNAs (miRNAs) [22]. In addition, a plethora of disease conditions are associated with development of PH including various respiratory diseases like chronic obstructive pulmonary disease (COPD) [23] and interstitial lung diseases (ILD) [24], left heart failure [25] and obesity [26]. In PH, right ventricle serves a main target organ, determining the severity and outcome of patients with PH.

5.2.2 Right ventricular remodeling

As a main resulting effect, PAH exerts an increased vascular load on the RV, leading to its structural and functional changes (RV remodeling), eventually resulting in right heart failure. RV remodeling develops in various cardiopulmonary diseases accompanied with increased pulmonary artery pressure (PAP) and pulmonary vascular resistance (PVR) [27] including left ventricular failure [28], various forms of cardiomyopathies [29, 30], congenital heart diseases [31], valvular heart diseases [32], chronic obstructive pulmonary disease (COPD) [33], interstitial lung diseases [34] and sleep apnea [35]. In these diseases, presence of RV remodeling and dysfunction determine adverse outcome.

RV remodeling is a complex rearrangement of the myocardial micro- and macro-structure, established as a result of myocardial accumulation of extracellular matrix

(ECM) (myocardial fibrosis), capillary loss, inflammatory/immune cell infiltration and cardiomyocyte hypertrophy, in response to pressure overload, which further leads to adverse alterations in the myocardial performance, eventually resulting in right heart failure and premature death [36]. The mechanisms of pressure overload induced RV remodeling are complex and remain incompletely understood. However, recent studies have demonstrated that various pathological processes may contribute to the development and pathobiology of RV remodeling including augmented myocardial fibrosis [27], inflammation [37], impaired myocardial capillarization [38], dysregulated neurohormonal homeostasis [39], altered metabolism [40], mitochondrial dysfunction [41] and increased production of reactive oxygen species (ROS) [42].

Although, an acute increase in afterload is less tolerated in the RV as compared to the LV, in the setting of PH, RV afterload increases gradually over the years thus providing enough time for the RV to adapt [43, 44]. One of the adaptive mechanisms of the RV remodeling is RV wall thickening (RV hypertrophy), which develops in the initial (adaptive) phase of RV remodeling, thus allowing for the generation of higher pressure to overcome increased afterload. Development of RV hypertrophy is mainly based on the increased synthesis of new sarcomeres and other contractile protein enabling RV cardiomyocytes to increase their length and diameter with the main purpose to increase cardiomyocyte contractility. In addition, RV adaptation to the pressure overload is also accompanied with the development of myocardial fibrosis [27], which serves as a supporting frame for the cardiomyocytes to couple their contractility to the increased RV wall stress [45]. Similarly, RV adaptation is also associated with the increased myocardial capillary density in the pressure overloaded RV, to ensure proper supply of nutrients and oxygen to the cardiomyocytes [38]. The development of myocardial fibrosis, cardiomyocyte hypertrophy and changes in myocardial capillarization, as main components of RV remodeling, occur simultaneously and involve intricate overlapping signaling pathways in the myocardial cells including cardiomyocytes, fibroblasts, resident/infiltrated immune cells and coronary artery endothelial cells through complex crosstalk mediated by various growth factors, cytokines and chemokines.

Taken together, initial changes in the RV structure upon gradual pressure overload induction aim to maintain RV function against the increased RV afterload at the expense of structural changes (adaptive RV remodeling). However, at some point over the course of the disease, the RV expires its ability to withstand against continuous

pressure overload due to inadequate/excessive myocardial fibrosis, impaired myocardial capillarization, and cardiomyocyte apoptosis (transition to maladaptive RV remodeling), ultimately resulting in right heart failure.

5.3 Osteopontin

5.3.1 Osteopontin as a member of matricellular proteins

The extracellular matrix (ECM) is a collagen-based network occupying extracellular space, that provides assembly, support and organization of the tissues. Matricellular proteins are considered as a family of non-structural matrix proteins capable of interacting with cell surface receptors, growth factors, proteases, and other inflammatory mediators, as well as with structural matrix proteins within the ECM. Accumulating evidence suggests that various matricellular proteins including CCN family of proteins, fibulins, osteopontin (OPN), periostin, SPARC family members, tenascin(s), and thrombospondins are involved in complex interactions between cardiac cells and ECM to regulate hypertrophic, fibrotic and inflammatory processes by exerting various cytokine- and chemokine-like effects on cardiac cells in homeostatic as well as stressed conditions [46-50]. Matricellular proteins are also well established as essential regulators/modulators of tissue remodeling and fibrosis [47, 48, 51, 52]. In the myocardium like in other tissues, matricellular proteins are regulated in response to various stress conditions like injury, inflammation and mechanical stretch which further might be involved in various beneficial and detrimental processes depending on the type of disease [53].

5.3.2 Osteopontin biology

Osteopontin gene is localized on chromosome 4q13 in humans and on chromosome 5 at the ric^{r} locus in mice [54, 55]. Human osteopontin protein consists of 314 amino acid residues, with a predicted molecular weight of 32 kilo Daltons (kDa). However, substantial post-translational modifications, including glycosylation and phosphorylation, increase its actual molecular weight ranging between 25 to 75 kDa on sodium dodecyl sulfate polyacrylamide gel electrophoresis (SDS-PAGE) [56, 57]. Mammals display a high degree of sequence homology of the osteopontin coding

sequence. Osteopontin is a multifunctional protein expressed in various cell types of the body including activated macrophages and T cells, osteoclasts, hepatocytes, smooth muscle, endothelial, and epithelial cells [58]. Osteopontin is also known as secreted phosphoprotein 1 (SPP1) and early T-lymphocyte activation protein 1 (ETA-1) highlighting its role in processes of inflammation and interactions with the immune system. In addition, it is involved in diverse physiological and pathological processes such as cell adhesion, migration, proliferation, inflammation and tissue repair [59] mainly by activating various cellular signaling pathways via integrin or CD44 receptors and interacting with growth factors, cytokines, chemokines and proteases which are involved in tissue repair and remodeling.

Myocardial osteopontin can be expressed by a number of cell types present in the myocardium such as cardiomyocytes, cardiac fibroblasts, resident macrophages and coronary artery endothelial cells in response to diverse stimuli including hypoxia, inflammation, toxin exposure and mechanical stretching [53].

5.3.3 Osteopontin cleavage

Osteopontin functions are influenced not only by posttranslational modifications [60], such as phosphorylation, glycosylation, but also by its cleavage mediated by thrombin and metalloproteinases. Osteopontin protein can be cleaved in its several sites with various extracellular proteases including MMP-3, -7, -9 and thrombin (Figure 1). MMP-9 cleaves osteopontin at amino acid positions 151–152, 193–194, and 195–196 yielding four distinct peptides with biological activities [61]. Combined effects of thrombin, MMPs, plasmin and cathepsin D can yield seven N-terminal fragments of osteopontin containing GRGDSVVYGLR motif [62]. Thus, osteopontin cleavage is a prerequisite for exposing some receptor binding domains, consequently influencing its activity against some of its receptors.

5.3.4 Osteopontin receptors

Majority of osteopontin functions are based on its ability to engage with various integrins and CD44 with its specific receptor binding domains [59] (Figure 1). Thrombin cleaved N-terminal fragment of osteopontin binds to a number of integrins including α4β1-, α4β7-, α5β1-, α9β1-, αvβ1-, αvβ3- αvβ5-, αvβ6-, and α5β1-integrins via its two

close located but distinct motifs within the sequence GRGDSVVYGLR (amino acid residues 158–168 on human protein) containing RGD and SVVYGLR receptor binding domains [57, 63-71]. Apart from RGD and SVVYGLR motifs, osteopontin was also able to bind α4β1 integrin with ELVTDFPTDLPAT motif [72]. However, thrombin cleavage is not required for the full adhesion to αvβ3-, αvβ5- or αvβ6-integrins as these integrins bind to RGD domain of full osteopontin [71]. In summary, osteopontin binds to a complex system of integrin receptors along with CD44 with its receptors binding domains and overall effect of osteopontin on cell functions may be the activation of several receptor signaling pathways.

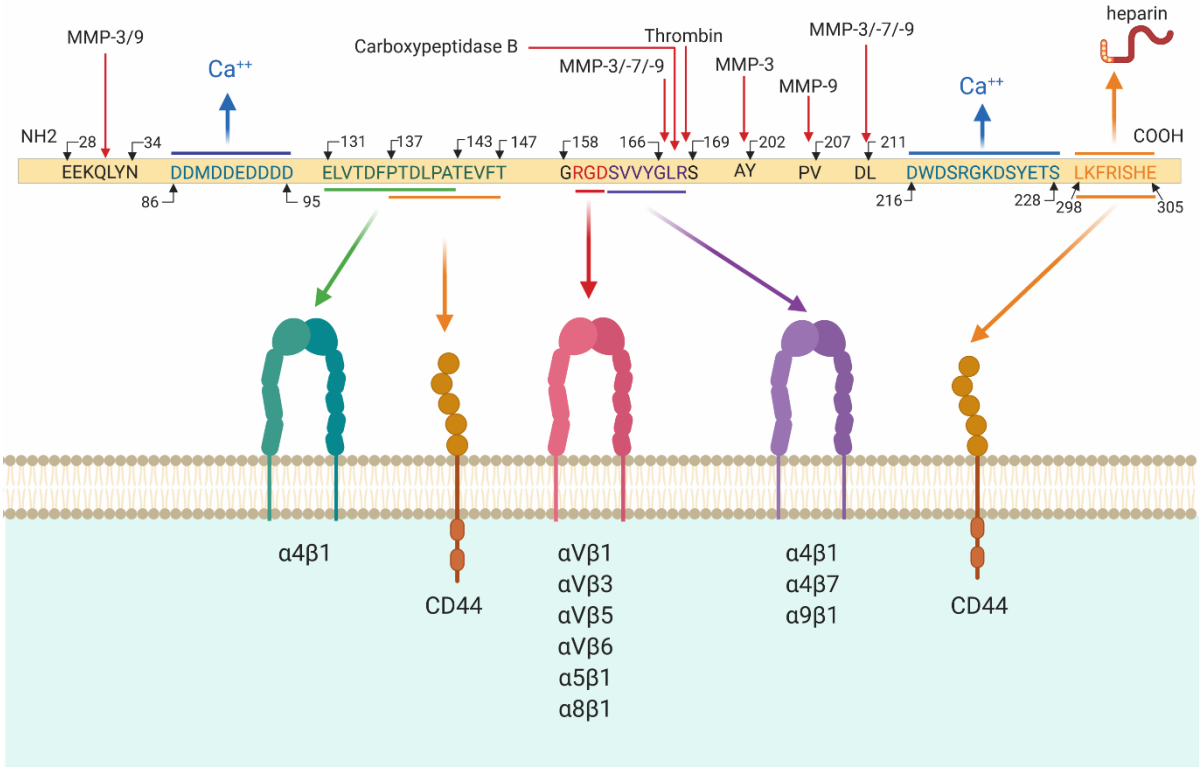

Figure 1. Osteopontin structure, cleavage sites; receptor binding domains and its receptors.

Human osteopontin consists of 314 amino acid sequences. Osteopontin can be cleaved at several sites with various proteases including with thrombin (between amino acids 168 - 169), MMP-3 (between amino acids 31 – 32, 166 – 167, 201 – 202 and 210 – 2011), MMP-7 (between amino acids 166 – 167 and 210 – 211) and MMP-9 (between amino acids 31 – 32, 166 – 167, 206 – 207 and 210 – 211). ELVVTDFPTDLPAT sequence binds to integrin α4β1. RGD sequence binds to αVβ1, αVβ3, αVβ5, αVβ6, α5β1, α8β1. SVVYGLR sequence binds to α4β1, α4β7 and α9β1. PTDLPATEVFT and LKFRISHE sequences bind to CD44 receptor. Figure was created using BioRender.com

5.4 Osteopontin in heart failure

Osteopontin expression in adult healthy myocardium is very low or undetectable [73-77]. Embryogenesis is associated with the augmented expression of osteopontin in various organs including the heart [75, 78, 79]. Despite this implied function during embryogenesis, OPN KO mice grow to maturity without any overt signs of morphological and functional cardiac abnormalities in homeostatic condition [49, 80]. This allowed scientist to exploit those mice in a number of disease models including cardiovascular diseases particularly in LV failure models including angiotensin-II (Ang II) - [80], aldosterone- [81] and transverse aortic constriction (TAC) - induced LV remodeling [82], desmin-deficient model of dilated cardiomyopathy (DCM) [83], streptozotocin-induced model of mouse diabetic cardiomyopathy [84], left anterior descending artery ligation (LAD-ligation) model of myocardial infarction (MI) [85] and brief repetitive LAD-occlusion model of ischemia and reperfusion cardiomyopathy [86].

Table 1. Summary of selected studies evaluating cardiac fibrosis and function in osteopontin knockout mice in various cardiac disease models

Authors	Cardiac disease model	Fibrosis staining method	Cardiac fibrosis*	Cardiac function*
Sam et al., 2004 [81]	Aldosterone-induced LV remodeling	TS	↓	deteriorated
Collins et al., 2004 [80]	Angiotensin II-induced LV remodeling	TS	↓	deteriorated
Matsui et al., 2004 [49]	Angiotensin II-induced LV remodeling	TS	↓	deteriorated
Lorenzen et al., 2015 [87]	Angiotensin II-induced LV remodeling	SRS	↓	deteriorated
Krishnamurthy et al., 2008	LAD-ligation-induced MI	TS	↓	deteriorated
Psarras et al., 2012 [83]	Desmin-deficient mouse dilated cardiomyopathy	TS	↓	ameliorated
Duerr et al., 2014 [86]	Brief repetitive LAD-occlusion induced ischemia and reperfusion cardiomyopathy	SRS	↑	deteriorated
Subramanian et al., 2007 [84]	Streptozotocin-induced diabetic cardiomyopathy	TS	↓	ameliorated

Abbreviations: LV, left ventricle; LAD, Left anterior descending artery; MI, myocardial infarction; TS, Trichrome staining; SRS, Sirius red staining; ↑, increased cardiac fibrosis compared to WT; ↓, decreased cardiac fibrosis compared to WT.

Various studies have documented osteopontin as a major pathogenic player in various fibrotic diseases of different tissues and organs by its ability to involve in tissue fibrogenesis. This understanding is based on the well-established fact that osteopontin induces collagen expression in a number of cell types and its expression closely associates with the collagen expression and deposition in the tissues of fibrotic diseases of different organs including liver, kidney, lung and heart [85, 87-92]. Similarly in various heart failure models, the most notable phenotype of OPN KO mice is attenuated myocardial fibrosis [93, 94] (**Table 1**).

However, despite of the fact that osteopontin deficiency leads to profound decrease of myocardial fibrosis in heart disease models, it does not necessarily lead to improved cardiac performance, in fact, in vast majority of disease models, upon exposure to the stimulus, OPN KO mice display deteriorated cardiac function, except few models, in which osteopontin deficiency leads to the improved cardiac function in mice (**Table 1**). Various cell types may express osteopontin in the myocardium depending on cardiac diseases (**Table 2**) or disease models (**Table 3**).

Table 2. Summary of selected studies evaluating the origin of myocardial osteopontin in patients with various cardiac diseases

Authors	Heart tissue	Method	Source
Graf et al., 1997 [75]	Heart tissues from explanted heart of ischemic or idiopathic cardiomyopathy patients	ISH	Cardiomyocytes
Stawowy et al., 2002	RV biopsies of DCM patients	IHC	Cardiomyocytes
Satoh et al., 2005 [88]	RV biopsies of DCM patients	ISH	Cardiomyocytes
Lo´pez et al., 2013 [89]	Septal endomyocardial biopsies of hypertensive cardiomyopathy patients	IHC	Cardiac myofibroblasts
Murry et al., 1994 [77]	Heart tissues from explanted heart of MI patient	ISH, IHC, NB	Infiltrating macrophages
Soejima et al., 2007	Blood samples of heart failure patients with different etiologies	FC	Circulating T cell
Szalay et al., 2009 [95]	Endomyocardial biopsies of chronic myocarditis patients	ISH, IHC	Infiltrating macrophages

Abbreviations: RV, Right ventricle; DCM, Dilated cardiomyopathy; ISH, In situ hybridization; IHC, Immunohistochemistry; NB, Northern blot analysis; FC, Flow cytometry.

Although, available studies have focused only on the extracellular secreted form of osteopontin as it is widely accepted that it is secreted into an extracellular environment in the context of cardiac remodeling and fibrosis, the intracellular role cannot be

ignored [96] and specific studies are required investigating the intracellular roles of osteopontin in heart diseases.

Table 3. Summary of selected studies evaluating the origin of myocardial osteopontin expression in various animal models of cardiac diseases

Authors	Model	Method	Source
Graf et al., 1997 [75]	TAC-induced LV remodeling in rats	IHC	Cardiomyocytes
Graf et al., 1997 [75]	Clipped renal artery-induced LV remodeling in rats	ISH, IHC	Cardiomyocytes
Singh et al., 1999 [97]	LV remodeling in spontaneously hypertensive rats	ISH, IHC	primarily in nonmyocytes in the interstitial and perivascular space
Trueblood et al., 2001 [85]	LAD-ligation induced MI in mice	ISH, IHC	Interstitial cells
Subramanian et al., 2007 [84]	Streptozotocin-induced diabetic cardiomyopathy in mice	IHC	Cardiomyocytes
Williams et al., 1995 [76]	hereditary cardiomyopathy in hamsters	ISH	Infiltrating macrophages
Sam et al., 2004 [81]	Aldosterone-induced LV remodeling in mice	IHC	Interstitial cells
Psarras et al., 2012 [83]	Desmin-deficient dilated cardiomyopathy in mice	ISH, IHC	Infiltrating macrophages
Duerr et al., 2014 [86]	Brief repetitive LAD-occlusion induced ischemia-reperfusion-induced cardiomyopathy in mice	PCR	Cardiomyocytes
Murry et al., 1994 [77]	Freeze-thaw induced MI in rats	ISH, IHC	Infiltrating macrophages
Weirather J et al., 2014 [98]	LAD-ligation induced MI in mice	Cell culture	monocytes/macrophages
Szalay et al., 2009 [95]	Viral myocarditis induced dilated cardiomyopathy	ISH, IHC	Infiltrating macrophages
Fan et al., 2013	Angiotensin II-induced LV remodeling in mice	IHC	Interstitial cells/extracellular localization
Nadadur et al., 2012	MCT-induced RV remodeling in mice	IHC	Interstitial cells/extracellular localization
Lorenzen et al., 2015 [87]	Angiotensin II-induced LV remodeling	IHC	Interstitial cells/extracellular localization

Abbreviations: TAC, Transverse aortic constriction; LV, Left ventricle; RV, Right ventricle; LAD, Left anterior descending artery; MI, Myocardial infarction; ISH, In situ hybridization; IHC, immunohistochemistry; OPN, Osteopontin; MCT, monocrotaline; IHC, Immunohistochemistry.

Current evidence on osteopontin biology in cardiac homeostasis and diseases state that osteopontin might represent a potential therapeutic target for the heart failure treatment. It is now widely acknowledged that inhibiting or activating osteopontin function/expression and its upstream or downstream signaling pathways by different strategies such as neutralizing antibodies, small-molecular inhibitors, and aptamers and peptide analogues of osteopontin might appear to be a promising strategy to modulate adverse cardiac remodeling in heart failure with various etiologies. However, in contrast to left heart failure, the role and function of osteopontin in right heart failure remain unknown and specific studies are still required to elucidate its exact role in right heart failure condition.

5.4.1 Osteopontin in heart failure - dilated cardiomyopathy

Dilated cardiomyopathy (DMC) is a severe disease of the myocardium characterized with progressive ventricular chamber dilatation with the genetic mechanisms of development associated with increased myocardial inflammation [99]. The link between infiltrating inflammatory/immune cells and osteopontin expression has been studied in more detail in DCM compared to pressure overload-induced cardiac remodeling.

Mice specifically overexpressing osteopontin in cardiomyocytes develop severe DCM due to increased recruitment of inflammatory cells to the myocardium along with excessive collagen accumulation, leading to chronic myocarditis, resulting in premature death [100, 101]. In desmin deficient model of DCM, desmin deficient mice develop severe LV dysfunction due to severe myocardial inflammation and fibrosis, while mice deficient for both osteopontin and desmin show improved LV systolic function, mostly due to decreased myocardial inflammation and fibrosis, suggesting central role of osteopontin in deterioration of the cardiac function in desmin KO mice [83]. In line with this finding, Papathanasiou et al., show that in desmin deficient mice displaying the signs of DCM, cardiomyocyte specific tumor necrosis factor-α (TNF-α) overexpression rescues overall cardiac inflammation, ultrastructural abnormalities and cardiac dysfunction at least in part due to significantly downregulated osteopontin [102]. In contrast to those studies, another study exploiting viral myocarditis model of DCM show that OPN KO mice are not protected from myocardial inflammation, although displayed attenuated cardiac fibrosis compared to WT counterparts [95].

Cardiomyocyte specific integrin-linked kinase (ILK) KO mice develop spontaneous DCM characterized my excessive myocardial fibrosis, cardiomyocyte apoptosis and inflammatory cell accumulation resulting in high mortality at least in part due to augmented osteopontin expression in cardiomyocytes and application of anti-osteopontin antibody mitigate heart failure in those mice [103]. However, there are also studies indicating the beneficial effects of osteopontin in DCM. For example, osteopontin-derived (SVVYGLR) SV peptide treatment improves cardiac function and inhibit LV dilatation and cardiomyocyte hypertrophy in hamster model of DCM due to myofibroblast differentiation, increased type III collagen accumulation and increased angiogenesis [104].

Patients with DCM also display significantly increased levels of myocardial osteopontin expression compared ischemic cardiomyopathy patients and osteopontin expression levels strongly correlate with collagen expression [105]. In addition, it has been documented that both the osteopontin expressing circulating CD4+T lymphocytes and circulating osteopontin levels correlate with the severity of the functional class in patients with HF and plaque instability in coronary artery disease (CAD) patients, highlighting the important role of osteopontin-expressing inflammatory cells as contributors to different heart diseases [106, 107].

As OPN KO mice display altered ECM assembly and collagen content in adult tissues, the question arises as whether the effects observed in OPN KO mice regarding inflammatory cell function derive from changes in ECM structure and/or from direct effects of osteopontin on inflammatory and immune cells. In summary, the current knowledge indicates that osteopontin is involved in the pathogenesis of DCM at least in part due to increased myocardial inflammation.

5.4.2 Osteopontin in heart failure - myocardial infarction

Myocardial infarction (MI) is an acute coronary artery atherothrombotic occlusive disease characterized by myocardial cell death due to imbalances between myocardial oxygen supply and demand [108]. Despite of the great progress of recent years in diagnosis and treatment of this condition, the overall mortality and morbidity remain high.

Studies have conclusively shown that osteopontin plays a critical role in reparative processes after myocardial infarction by promoting myocardial fibrosis in order to

prevent post-MI left ventricular dilatation and systolic dysfunction [73, 85]. Although, the exact mechanisms of beneficial effects of osteopontin in MI remain unknown, recent studies have indicated that osteopontin producing macrophages are important players in mediating those effects by removing tissue debris and promoting collagen synthesis [77, 98, 109]. The beneficial effects of osteopontin may be also explained by its ability to inhibit MMP-2 and MMP-9 activation after myocardial infarction [110]. In addition osteopontin promotes myocardial angiogenesis after myocardial infarction [111].

Taken together, osteopontin promotes healing processes after myocardial infarction by activating reparative macrophage population, promoting myocardial fibrosis and angiogenesis.

5.4.3 Osteopontin in heart failure - myocardial capillarization

In the pressure overloaded myocardium, hypertrophied cardiomyocytes are supplied with proper level of nutrients and oxygen due to increased myocardial capillarization and vascularization to maintain cardiac contractility against increased afterload [38, 112]. However, at some point of the course of the disease, myocardium fails to maintain adequate tissue capillarization marking the transition of cardiac hypertrophy to heart failure [38, 112]. The mechanisms controlling myocardial capillarization in cardiac hypertrophy and failure are not fully understood and recent studies have identified various endogenous regulators of myocardial capillarization with complex interactions between variety cell types of the myocardium [113]. Among these pro- and antiangiogenic factors, osteopontin also has emerged as an essential regulator of myocardial angiogenesis.

Osteopontin contributes to the angiogenesis by potentiating integrin-linked kinase (ILK) and NF-κB-mediated hypoxia inducible factor one alpha (HIF1-α)-dependent vascular endothelial growth factor (VEGF) expression [114]. Angiogenic response is pivotal for scar formation and cardiac repair in the setting of different cardiac diseases [115]. The effect of osteopontin deficiency on myocardial capillarization in most of the heart pathologies are not studied well except MI. Myocardial angiogenesis is significantly impaired in the absence of osteopontin in the setting of MI [111]. The decrease in *in vitro* tube formation in cardiac endothelial cells isolated from OPN KO mice is restored by treatment with purified osteopontin [111]. Thus, osteopontin may play an important

role in post-MI LV remodeling, at least in part, by promoting myocardial angiogenesis. Taken together, available studies demonstrate that osteopontin is a proangiogenic factor and its presence is essential to maintain myocardial capillarization; however, its role in the myocardial capillarization of the pressure overloaded myocardial is not known and needs to be addressed in the further studies.

5.4.4 Osteopontin in heart failure - myocardial inflammation

Inflammatory cells have been identified as making significant contributions to fibrosis in a number of different tissues and diseases. Increased expression of osteopontin by resident and recruited inflammatory cells increases collagen deposition and accumulation in various tissues [100, 106, 107]. Similarly, heart diseases are also associated with certain degree of myocardial inflammation, which may contribute to myocardial fibrosis. As main players of inflammation, various cytokines and chemokines are actively involved in the onset and progression of myocardial fibrosis.
Similarly, expression of osteopontin by various immune/inflammatory cells in the setting of different cardiac diseases, has come to light [76, 77, 83]. Osteopontin also has been shown to exert cytokine- and chemokine-like functions. In addition, in different cardiac diseases, osteopontin is expressed by various cell types of the myocardium including resident and infiltrating immune cells upon insult induction, results in hypertrophic and fibrotic cardiac remodeling [87, 88].
Moreover, osteopontin expressed in circulating leucocytes also may actively involve in inflammatory cell recruitment to the myocardium and systemic inflammation in patients with various cardiac diseases [106].
Among various inflammatory cells, macrophages represents the dominant inflammatory cell population in the pressure overloaded myocardium [116]. Macrophage infiltration of hypertrophied myocardium has been shown in various models, such as high-salt-water drinking spontaneously hypertensive rats and TAC-operated mice display increased [117, 118]. Velten et al., show that mice subjected to TAC-surgery, display increased MAC-2 positive macrophage content in time-dependent manner reaching maximum at 14 day, showing the same pattern with osteopontin expression. [119]. In addition, WT mice show increased recruitment of CD45+ monocytes to left ventricular myocardium in response to Ang-II infusion, which was completely abolished in KO mice [87], indicating the possible involvement of

osteopontin in macrophage recruitment to the pressure overloaded myocardium. Nevertheless, various macrophage populations are essential in maintaining myocardial homeostasis in health and in repairing the myocardial lesions [120]. M1 macrophages were detected at greater levels in TAC-operated myocardium *versus* M2 macrophages, indicating the involvement of macrophages to pro-inflammatory and pro-fibrotic processes [118]. Although, osteopontin expressing macrophages have been shown to be beneficial in the setting of MI, it remains unknown whether osteopontin-expressing leucocytes or its expression in resident or recruited monocyte/macrophage populations may play role in other cardiac pathologies.

5.5 Osteopontin in pulmonary hypertension

PAH is associated with the pulmonary upregulation of osteopontin in human idiopathic pulmonary arterial hypertension (IPAH) [121], hypoxia-induced PH in mice [122, 123], hypoxia-induced PH in rats [124, 125] and MCT-induced PH in rats [126, 127], which may result in increased levels of circulating osteopontin in those models [127]. Several cell types produce osteopontin within the remodeled PAs including fibroblasts in the adventitial layer in IPAH patients, bovine hypoxia-induced PH [50] and rat hypoxia-induced PH [124] and PASMC in the media in rat MCT- and hypoxia-induced PH [127, 128].

Functionally, osteopontin has been shown to be implicated in the pathogenesis of PAH by involving in recruitment and retention of macrophages and T lymphocytes to the sites of inflammation of the remodeled pulmonary arteries (PA) [124].

Several mediators have been identified to modulate osteopontin expression both *in vitro* and *in vivo* PAH models. *In vivo* studies have demonstrated that, atrial natriuretic peptide (ANP) deficient mice exhibit augmented pulmonary osteopontin upregulation [122], while mice with mutated transforming growth factor-beta (TGF-β) receptor type 2 (TGF-βR2) display blunted osteopontin expression in response to hypoxia exposure [123].

PASMCs have been widely used to study the role of osteopontin in various *in vitro* models. Several players with known roles in PAH pathogenesis, have been found to induce osteopontin expression, including acidic fibroblast growth factor (FGF1) [125], Ang-II [125], TGF-β1 [129] and hypoxia [130, 131]. In addition, several signaling pathways have been identified to induce osteopontin expression in PASMC by using

selective inhibitors in response to various stimuli, including Ras/JNK (SP-600125) and Ras/MEK1/2 (U-0126, PD-98059) signaling pathways to FGF-1 stimulation [125], ERK (U0126) and p38MAPK (SB203580) signaling pathways to hypoxia exposure [131]. Taken together, various growth factors and hypoxia induce osteopontin expression in the pulmonary artery cells, which further recruits inflammatory cells to the site of PA remodeling.

Although, more specific agents targeting osteopontin directly such as osteopontin-neutralizing antibodies and aptamers have not been tested for the efficacy in PAH models, few pharmacological agents have been shown to inhibit osteopontin expression indirectly. Amon them, pioglitazone, an activator of peroxisome proliferator-activated receptor gamma (PPAR-γ), was demonstrated to inhibit osteopontin expression, improve survival, reduce PAP and PA remodeling, improve right ventricular remodeling in MCT model of PAH along with reduced macrophage content in the lung tissues [126]. In addition, there are number of pharmacological agents shown to improve PAH along with inhibiting pulmonary expression of osteopontin in animal models of PAH, including calcium-sensing receptor antagonist NPS2390 [128] and SERT inhibitor fluoxetine [127]. To sum up, reduced osteopontin expression by the used agents in PAH models may be just overall reflection of the improved pulmonary artery remodeling and more osteopontin specific agents are warranted to test in animal models of PAH.

5.6 Aim of the study

In LV pathologies, osteopontin is actively involved in several physiological and pathological processes. Mainly, osteopontin regulates ECM homeostasis and inflammatory processes in the myocardium. As already mentioned in previous sections, the findings of osteopontin biology from the LV studies cannot be simply extrapolated to the RV physiology and pathology, based on the differences between the RV and LV. Although, there are no studies specifically investigating the role of osteopontin in RV remodeling, few studies have shown that osteopontin is upregulated in the remodeled RV myocardium in different animal models of PAH. In addition, studies have shown that osteopontin levels correlate with RV structural and functional parameters in heart failure and PAH patients. Thus, the role and functions of osteopontin in RV remodeling remain elusive and studies are required to investigate its impact on pressure overloaded RV myocardium in afterload-independent models like PAB.

Taken together, we hypothesized that osteopontin play an active role in adverse RV remodeling and dysfunction in response to pressure overload, thus it represents a potential target to treat RV remodeling and dysfunction. Therefore, we put the following two objectives to fulfill our hypothesis:

1 – to investigate RV structure and function in response to pressure overload by employing PAB surgery in OPN KO mice (osteopontin loss-of-function approach) compared to WT mice.

2 – to test if chronic osteopontin treatment influences on RV structure and function in PAB-operated OPN KO mice (osteopontin reconstitution approach) or WT mice (osteopontin gain-of-function approach).

6 METHODS

6.1 Animals

Male OPN KO (B6.129S6(Cg)-Spp1^{tm1Blh}/J) and C57BL/6J mice aged 12 – 16 weeks (n = 40 WT and n = 40 OPN KO) were used in these experiments (The Jackson Laboratory, Bar Harbor, ME, USA).
Mice were given free access to water and food and were housed under controlled temperature (22°C) and under standard light-dark cycle (12 hrs. each) throughout the experimental period. All experiments were approved by the governmental ethics committee for animal welfare (Regierungspräsidium Giessen (GI25/2018), Germany.

6.2 Experimental groups

In total 80 mice were included into the study; 40 mice for sham surgery, 40 mice for PAB surgery. Among these 80 mice, 40 mice were OPN KO, 40 mice were WT (figures). Both sham and PAB operated mice consisted of following 4 groups: WT mice treated with PBS (n=10), WT mice treated with rOPN (n=10), OPN KO mice treated with PBS (n=10) and OPN KO mice treated with rOPN (n=10) in total giving 8 groups. Intraperitoneal injection with either PBS (200µL) or rOPN (2.5µg in 200µL PBS) were started on the day of sham or PAB surgery with following injections every second day till the end the study (21 days).

6.3 Mouse intratracheal intubation

Initially, mouse was anesthetized in anesthetic chamber supplied with continuous flow of isoflurane (3 – 5 % mixed in 100% oxygen at flow rate of 1 L/min) delivered with an anesthesia system (Tabletop Laboratory Animal Anesthesia System, VetEquip Inc, Pleasanton, USA). A custom-made endotracheal tube made from an intravenous catheter (Vasofix® Safety 20Gx1¼", 1.1x33 mm, B. Braun Melsungen AG, Melsungen, Germany) with a blunted stylet as a stiff guide to facilitate the introduction of a cannula were prepared (Figure 2, Figure 3). A blunted stylet (Vasofix® Safety 14Gx2", 2.2x50 mm, B. Braun Melsungen AG, Melsungen, Germany) attached to a 50 mL syringe (Perfusor® Syringe, B. Braun Melsungen AG, Melsungen, Germany) fixed to a retort stand was used to hang the mouse with its upper incisors in a hanging position for the

intubation procedure (Figure 4).Following anesthesia induction (absence of paw reflex), mouse was positioned vertically on intubation stand (setup), with its upper incisor fixed to the blunted needle attached to the intubation stand.

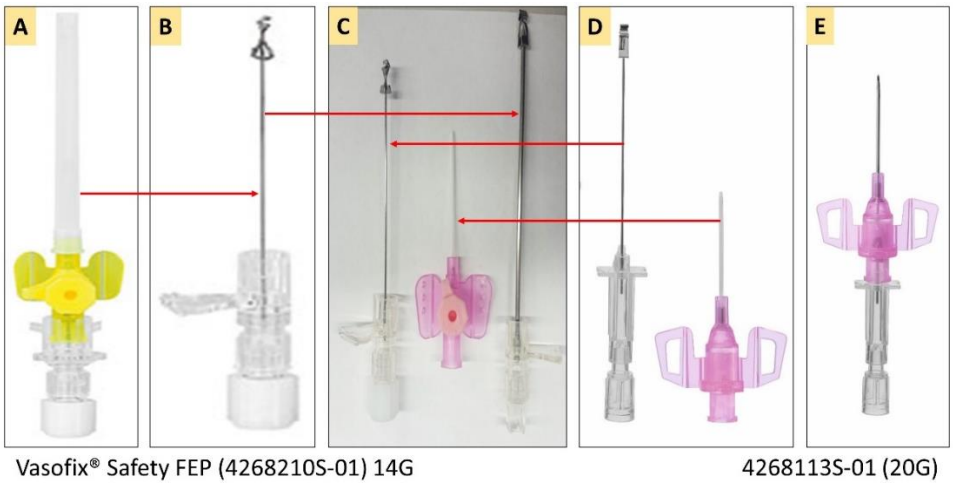

Figure 2. Required items for the preparation of customized mouse intratracheal intubating tube.

A) IV catheter - 14G, B) needle of the IV catheter - 14G, C) required parts of the IV catheters for the intubating tube preparation, D) Cannula (catheter) and needle of IV catheter - 20G, E) IV catheter - 20G.

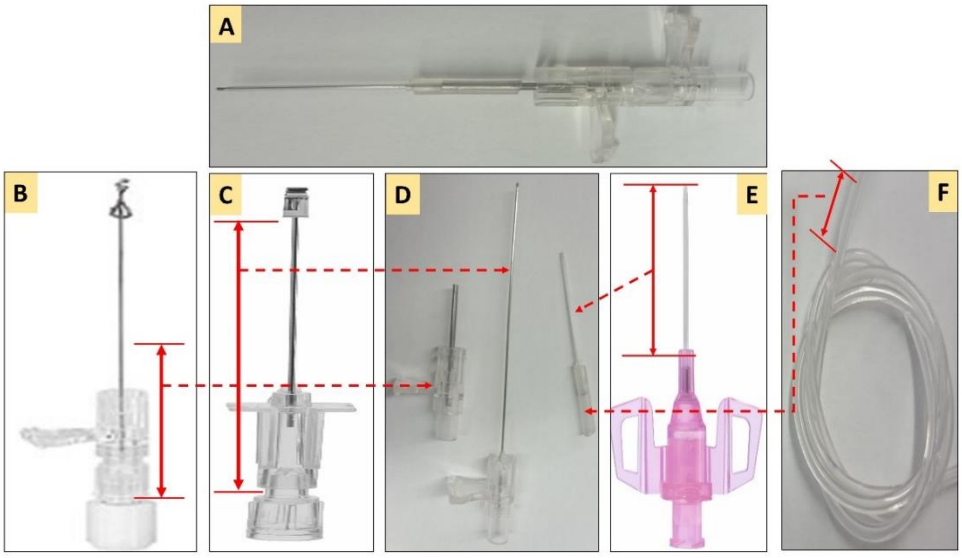

Figure 3. Preparation of customized mouse intratracheal intubating tube.

A) Complete intratracheal intubating tube, B) Selected part (red) of the needle of the IV catheter 14G, C) selected part (red) of needle of the IV catheter for the intubating tube, D) All required parts of the intubating tube, E) Selected part (red) of the cannula of the IV catheter 20G, F) tubing required for the intubating tube.

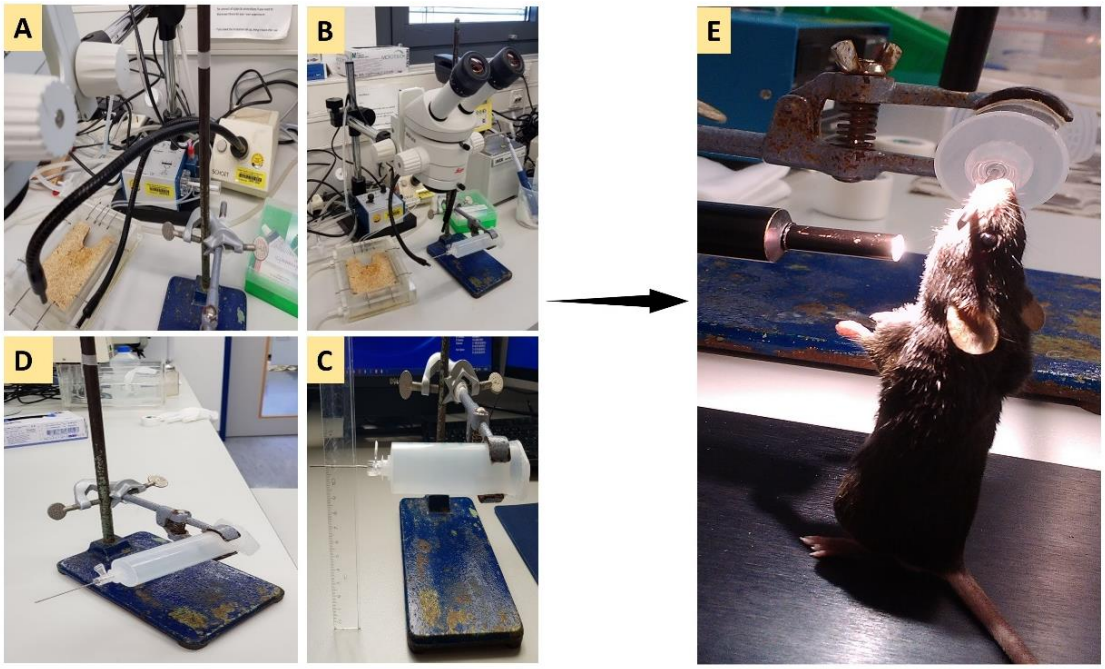

Figure 4. Surgical place and mouse positioning for the intratracheal intubation.

A) positioning of microscope, light and intubation stand ready for intubation (pictures taken from the right side), B) positioning of microscope, light and intubation stand ready for intubation (pictures taken from the left side), C) intubation stand, D) intubation stand height (11 cm).

A power light with flexible horns (KL-200, Fiber Optics Schott, Mainz, Germany) was used to illuminate the neck of the mouse to better visualize the vocal cords of the mouse during intubation. Under surgical stereomicroscope (Leica Microsystems, Wetzlar, Germany) at 8x magnification, the tongue of the mouse was taken out and fixed with the curved forceps held in the right hand, while oral cavity is widened with the teeth of second curved forceps held in the left hand to visualize vocal cords and trachea (as a light hole closing like a valve). Once vocal cords were seen well, the catheter of the intubation tube was gently inserted into the trachea with the right hand until the connector comes into the oral cavity. Once intubation tube was inserted into the tracheas, the mouse was positioned on homeothermic pad. The extender of intubation tube was detached; the connector of the intubation tube was connected to the Y-shaped connector of the small-animal ventilator (MiniVent type 845, Hugo Sachs Elektronik, March-Hugstetten, Germany). The success of the intubation was evaluated by the visual observation of the chest excursion synchronous with the ventilator. Maintenance of anesthesia was provided by continuous inhalation of 2% isoflurane mixed with oxygen. The eyes of animals were protected from drying with dexpanthenol eye ointment (Bepanthen® Bayer, Leverkusen, Germany).

6.4 Pulmonary artery banding

Throughout the experiment, mouse chest was illuminated with a power light with flexible horns. The paws of the mouse were taped down to the plate of the pad with surgical tapes. Under maintained anesthesia with isoflurane (2 – 2.5 % with 100% oxygen at flow rate of 1L/min), mouse chest wall was shaved and then applied with Braunoderm® (B. Braun Melsungen, Melsungen, Germany). A transverse incision (≈ 5 mm) of the skin was made with scissors, 2 mm away from the left sternal border, 2 mm lower than the level of the armpit. Upper layer of thoracic muscles was gently pulled cranially with two upper retractors, while lower layer muscles were pulled caudally with two lower retractors to expose the ribs. Then, a small incision was made with scissors at the level of the second intercostal space 2–3 mm from the left sternal border to open the thoracic cavity. Four retractors were gently inserted into the incision one-by-one and pulled away carefully and fixed with surgical tapes to the rib of the pad, to widen the opening of the chest wall.

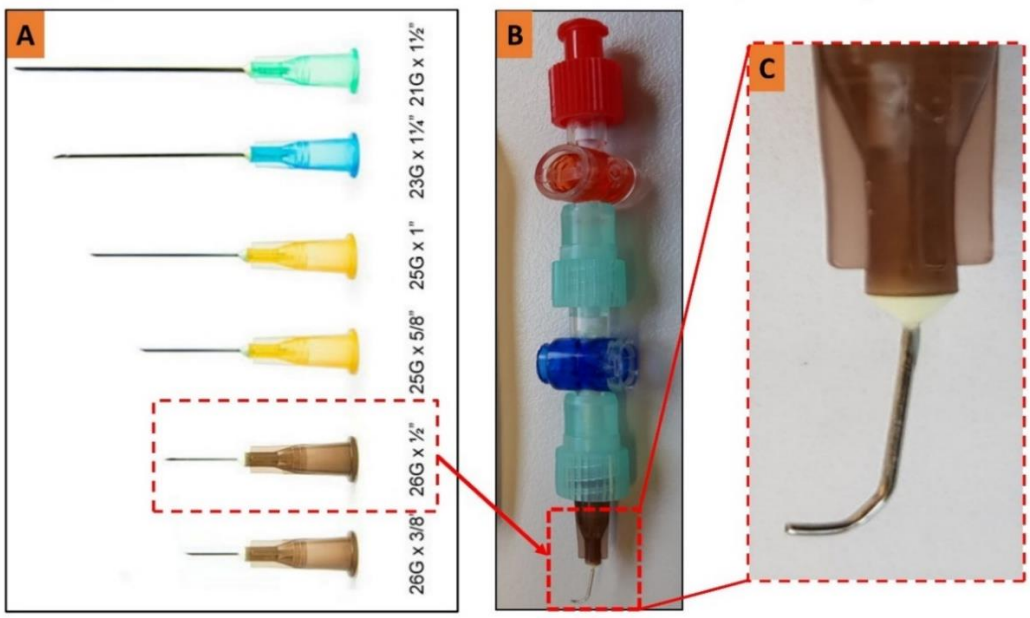

Figure 5. Vessel probe preparation.

A) needle G26½, B) curved and blunted needle attached to the holder made from attached several IV catheter cups, C) zoomed view of the curved and blunted needle

The thymus and fat were pulled away with forceps to the teeth of upper two retractors. With two forceps, the pericardial sac was gently pulled apart and attached to the teeth

of the retractors. After a mobilization of the pericardium, the pulmonary trunk was visualized. The pulmonary trunk was bluntly dissected with curved forceps from the aorta and left atrium. To create a tunnel underneath the pulmonary trunk, a vessel probe made from L-shaped 26-gauge with blunted needle (Becton Dickinson, Drogheda, Ireland) was used (Figure 4). The tip of the vessel probe was placed from the side of the pulmonary trunk closest to the left atrium and gently pushed underneath the pulmonary trunk so that the end of the probe tip appeared between the pulmonary trunk and aortic trunk. A small titanium ligating clip (Hemoclip®, Edward Weck, Research Triangle Park, NC, USA) was placed around the pulmonary trunk with specially adapted appliers (product# 523140, Hemoclip®, Edward Weck, Research Triangle Park, NC, USA) set to a width of 0.3 mm in diameter, which corresponds to approximately 75% occlusion of the luminal diameter. The chest retractor was removed, and the thymus was placed back to its physiological position.

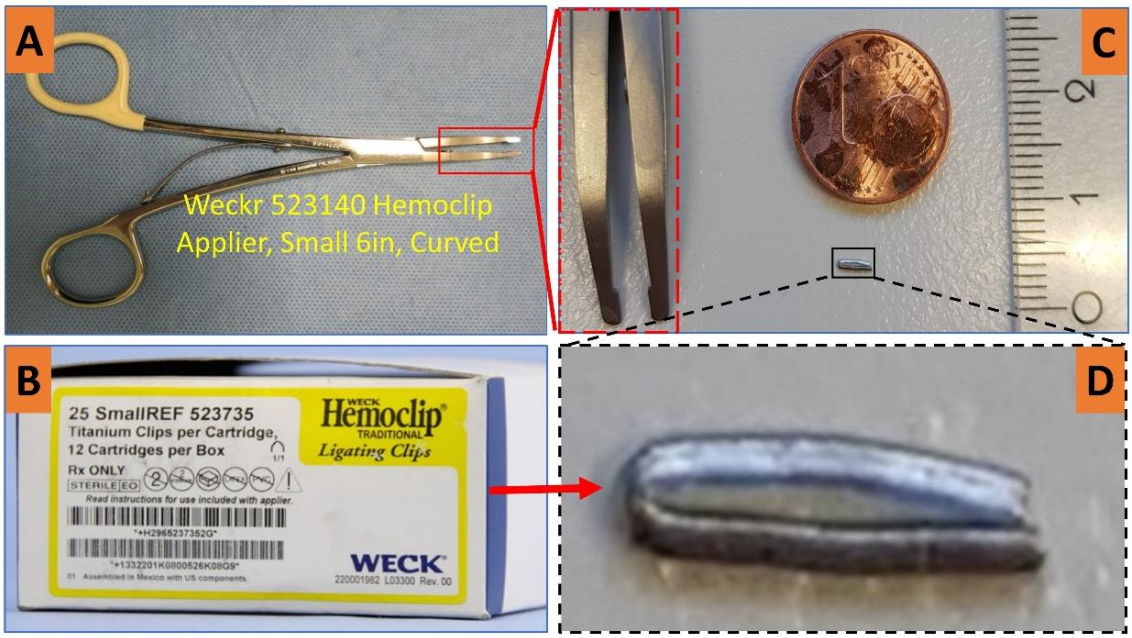

Figure 6. Clip applier and titanium ligating clip.

A) Clip applier, B) titanium ligating clip, C) clip compression in comparison to the 1 cent coin and ruler, D) zoomed picture of a compressed clip.

The lungs were then reinflated by shutting off the outflow on the ventilator for 1–2 sec using a finger. The chest cavity was closed by bringing together the second and third ribs with two 6-0 polypropylene sutures (Prolene®, Ethicon, Norderstedt, Germany). While making a knot, slight pressure was applied on the chest with the needle holder

to reduce the volume of free air in the chest cavity. All layers of muscle were moved back to their physiological positions. Then, the skin was closed with 6-0 polypropylene suture and the wound was treated with Braunoderm® (Braun, Melsungen, Germany).

Figure 7. Clip applier with inserted adjustable stop mechanism.

Adjustable stop mechanism allows to set required degree of clip constriction and maintain the same degree of constriction in all mice studied.

For the sham operation, dissection of the pulmonary trunk was performed using the vessel probe, but a ligating clip was not placed around the pulmonary trunk. The lungs were then reinflated and the wound was closed. Once spontaneous respiration resumed, mice were extubated, placed under a heating lamp and were closely monitored for 4 - 6 hours to ensure complete recovery from the anesthesia. Then, mice were housed to a standard rodent cage with free access to food and water in a room kept at 25°C. Pre- and postoperative analgesia was maintained by administration of buprenorphine hydrochloride (Temgesic®, 0.1 mg/kg, Essex Pharma GmbH, Munich, Germany) 0.05 mg/kg body weight subcutaneously every 24 hours for 3 to 5 days.

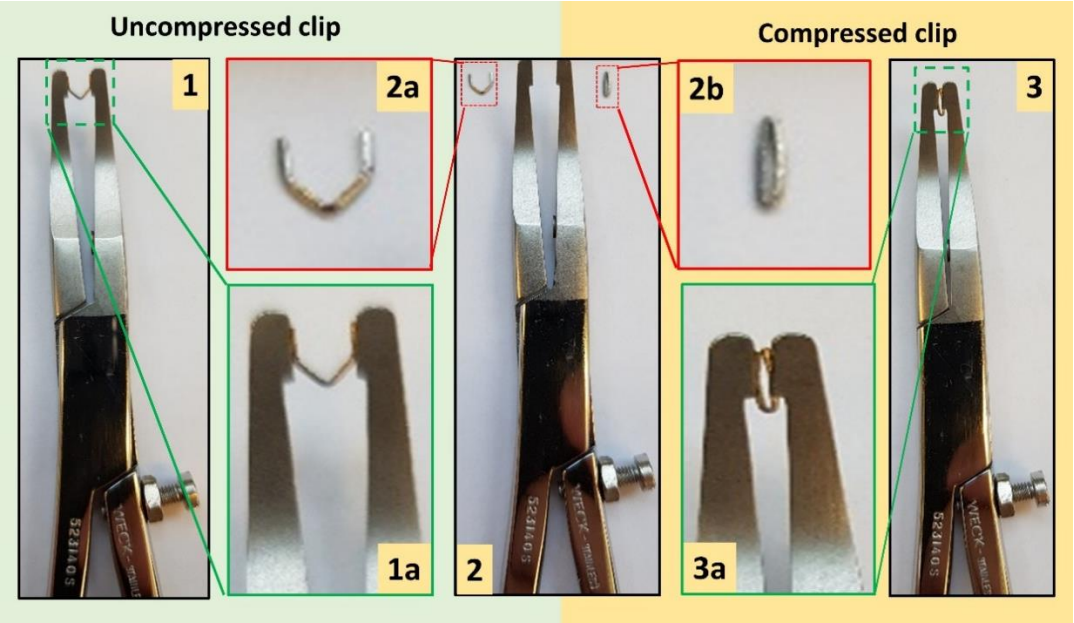

Figure 8. Titanium clip constriction using clip applier.

1) Clip applier with uncompressed in its teeth; 1a) zoomed teeth of the clip applier, 2) comparison of uncompressed vs compressed titanium ligating clip; 2a) uncompressed clip; 2b) compressed clip, 3) Clip applier with compressed clip on its teeth; zoomed compressed clip**.**

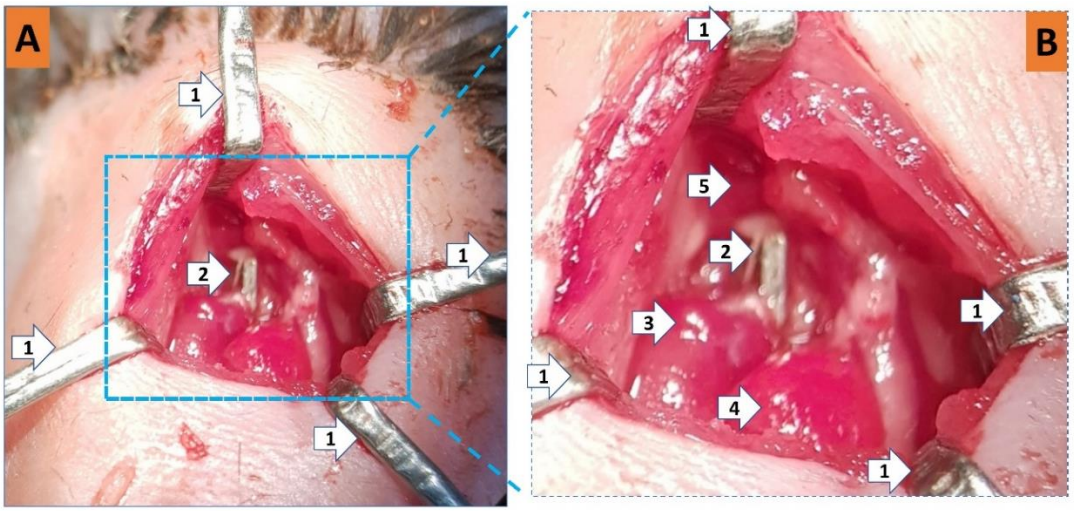

Figure 9. Intraoperative illustration of pulmonary trunk banding.

A) picture taken through the surgical microscope at 1.6 magnification, B) zoomed picture of surgical wound area. 1 – chest retractors, 2 – compressed titanium ligation clip, 3 – pulmonary trunk, 4 – left atrium, 5 – aortic arch

6.5 Osteopontin reconstitution

To investigate the effects of osteopontin gain-of-function (osteopontin administration) or reconstitution approaches in a mouse model of pressure overload induced RV remodeling, chronic treatment with mouse recombinant osteopontin (rOPN, Cat# 141-

OP, R&D systems) (2.5 µg/mouse intraperitoneally every second day) was performed. Both sham and PAB operated OPN KO and WT mice were treated intraperitoneally either with phosphate-buffered saline (PBS) or rOPN. A day before of hemodynamic measurements echocardiography examination was taken from all mice. At the end of the experiment (on day 21 of post-surgery), mice were subjected to hemodynamic measurements of systemic and pulmonary circulation. Further, the mice were sacrificed, and plasma and heart tissues were harvested for further analyses (Figure 10).

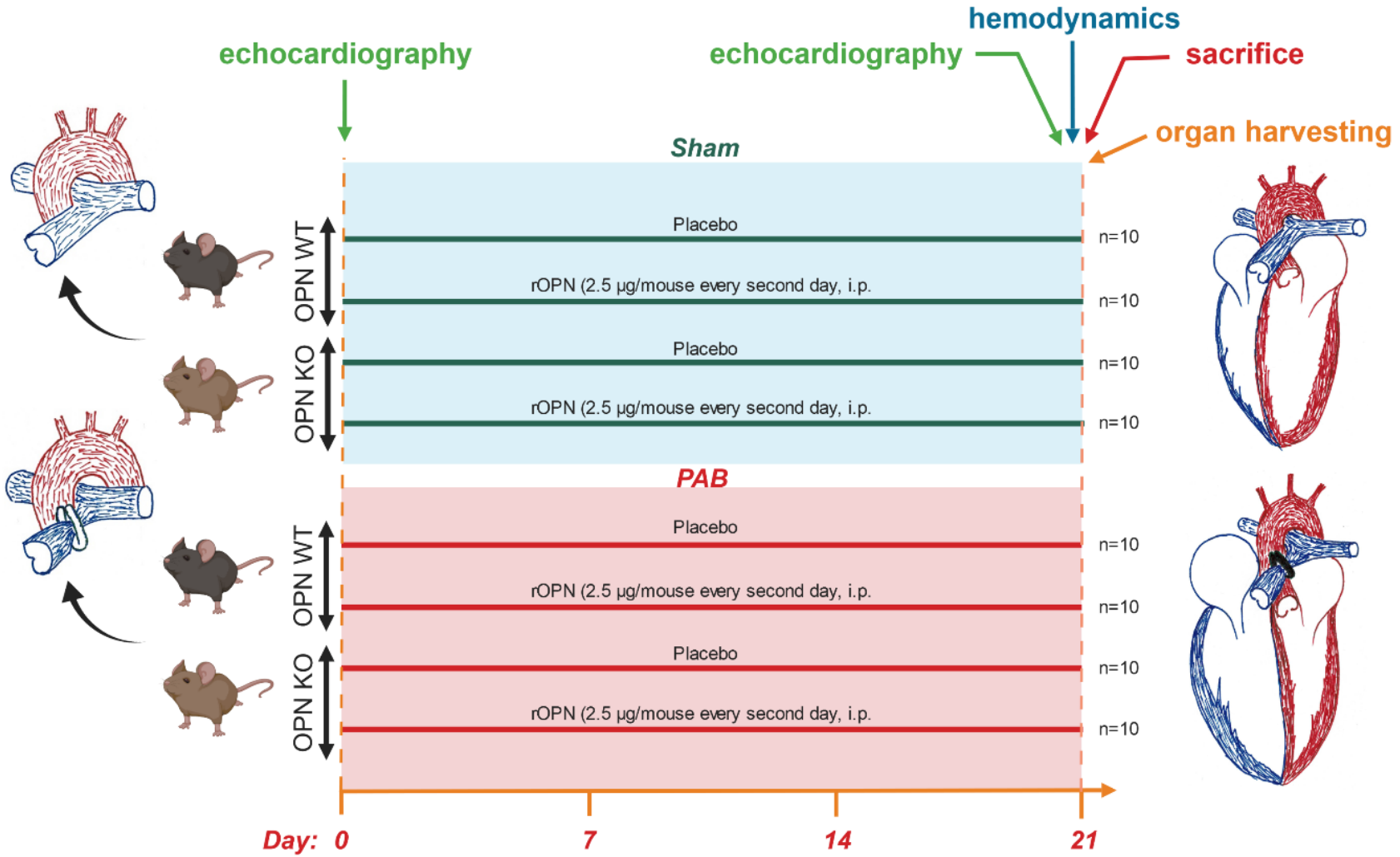

Figure 10. Experimental design.

OPN WT, osteopontin wildtype mice; OPN KO, osteopontin knockout mice; rOPN, recombinant osteopontin; PAB, pulmonary artery banding.

6.6 Echocardiography

Echocardiography was performed the VEVO2100 system equipped with a 30-MHz, 100-frame-per-second micro-visualization linier probe (MS400, mouse cardiovascular) (VisualSonics, Toronto, Canada). Initially, anesthesia was given to a mouse in an anesthesia induction chamber (Tabletop Laboratory Animal Anesthesia System, VetEquip Inc, Pleasanton, USA), with 5 % isoflurane mixed with 100% oxygen at flow rate of 1 L/min. Then, mouse was placed in a supine position on an imaging platform. Throughout the examination, the mouse snout was kept in a nose cone connected to the anesthesia system to maintain a steady-state sedation level (1 - 1.5% isoflurane mixed with 1 L/min 100% oxygen) while spontaneously breathing. Body temperature was monitored using a rectal thermometer (Indus Instruments, Houston, TX) to continuously monitor and keep body temperature at 37°C. Dexpanthenol, ophthalmic ointment (Bepanthen® Bayer, Leverkusen, Germany) was applied on both eyes to prevent drying of the sclera. Using surgical tape, the four paws of the mouse were secured to the electrocardiogram (ECG) electrodes after applying electrode gel to them to monitor heart rate (HR). To remove chest fur, depilatory cream was applied to the chest from the sternum to the diaphragm using a cotton applicator tip. The cream was removed after 2 min with a gentle rolling motion of the tissue papers and then the chest was cleaned with distill water moisturized gauze swab. A prewarmed acoustic coupling gel (Aquasonic® 100, Parker Laboratories, Inc) was applied over the chest wall of the anesthetized and immobilized mouse to overcome air attenuation.

Anesthesia was maintained with 1.5 – 2.5 % isoflurane throughout echocardiographic examination in order to maintain physiological heart rate (HR). HRs were kept consistent between experimental groups (400–550 bpm). However, if the HR was above the required range, the isoflurane concentration was temporarily increased to 4 -5 % and then decreased to 1.5 - 2 % after the HR reached the required level. While, if the HR was below the required range, the isoflurane concentration could be set at 0.5 % and then increased.

A standard 2D echocardiographic study was initially performed in the parasternal long-axis view for assessment of LV dimensions and systolic function. Image depth, width and gain settings were used to optimize image quality.

The echocardiographic measurements were recorded according to standard methods described in previously published reports [132]. RV free wall thickness (RVWT) was measured using right parasternal long-axis view with both M- and B-mode images. Cardiac output was measured either RVOT or LVOT blood flow parameters. RVOT VTI-derived CO. Two-dimensional images of the right ventricular outflow track (RVOT) were obtained from the parasternal short-axis view (with the focus on PA) at the level of the aortic valve and pulsed-wave Doppler profiling of the pulmonary blood flow was obtained. The pulsed-wave Doppler sample was positioned at the tip of the pulmonary valve leaflets and aligned to maximize laminar flow assisted with color Doppler mode. RVOT dimeter (RVOTd) was measured at the pulmonary valve levels during mid-systole using the parasternal short-axis view. RVOT VTI was measured from the pulsed-wave Doppler flow velocity profile of the RVOT. Thus, based on these echocardiographic measurements, RVOT stroke volume (SV) was calculated using the following formula: $SV= ((LVOTd)^2 \times 3.14 \times (VTI)/4)$. LVOT VTI-derived CO. The Doppler angle was modulated slightly to allow the interrogation beam almost parallel to aortic flow so that the maximum flow velocity was obtained. Left ventricular outflow tract (LVOT) flow velocity and velocity time integral (LVOT VTI) profiles were determined from a right supraclavicular view. The LVOT diameter (LVOTd) was measured using B-mode echocardiography at the middle of aortic valve during mid-systole using modified left parasternal log-axis view with the focus on LVOT. Thus, based on these echocardiographic measurements, LVOT SV was calculated using the following formula: $SV= ((LVOTd)^2 \times 3.14 \times (VTI)/4)$.

For assessment of the RV performance, tricuspid annular systolic velocity (RVS´) and tricuspid annular plane systolic excursion (TAPSE) were measured. For determination of TAPSE, M-mode cursor was oriented to the junction of the tricuspid annulus with the RV free wall using the apical four chamber view. RVS´ was measured by Tissue Doppler imaging (TDI) at the lateral part of the tricuspid annulus in the four-chamber view and the velocity was calculated.

All echocardiographic image (M-mode, 2D, and flows) measurements were performed excluding the respiration peaks and obtained in triplicate. All images were acquired within 10-25 min of anesthesia induction, and calculations were done after acquisition.

Once the imaging was completed, the chest wall was cleaned with tissue papers and paw tapes were removed. The anesthesia was turned off and the unrestrained mouse was allowed to recover on the heated ECG pad. Once the mouse was awake, it was returned to its cage.

6.7 Invasive hemodynamics measurements

Invasive hemodynamic measurements were performed in all mice following 3 weeks of sham or pulmonary artery banding surgery. Measurements were taken under isoflurane (Forene® Abbott, Wiesbach, Germany) anesthesia (Tabletop Laboratory Animal Anesthesia System, VetEquip Inc, Pleasanton, USA). Anesthesia was maintained by continuous inhalation of 1.5% isoflurane mixed with oxygen at flow rate of 1 L/min (Air Liquid, Siegen, Germany). The surgical procedures for catheterization were performed under a surgical stereomicroscope (Leica Microsystems, Wetzlar, Germany) at 8x magnification. For illumination a power light with flexible horns (KL-200, Fiber Optics Schott, Mainz, Germany) was used.

After intratracheal intubation, the mouse was placed supine on a homeothermic plate (AD Instruments, Spechbach, Germany) and connected to a small animal ventilator MiniVent type 845 (Hugo Sachs Elektronik, March-Hugstetten, Germany). The body temperature was controlled by the rectal probe connected to the control unit (AD Instruments, Spechbach, Germany) and was kept at 37°C during the catheterization. Using surgical tape, all four paws of the mouse were taped down to the heating plate. In an immobilized anesthetized animal, the neck and chest area were cleaned with Braunoderm® (Braun, Melsungen, Germany) and then an inverted T-shaped middle-neck incision from the sternum to mandible was made.

For the right ventricular catheterization, the right external jugular vein was carefully exposed by bluntly dissecting the surface of the right neck along the midclavicular line. After careful removal of the connective tissue surrounding the jugular vein, three ligatures of 6-0 polypropylene sutures were placed around the vein. The rostral ligature, placed just below the junction of the internal and external jugular vein, was ligated to prevent bleeding and then gently pulled and taped to the table. A very loose knot was placed to the middle suture. The caudal suture was gently pulled (without securing it) with a needle holder and clamped to the skin of the animal to fix it in the desired position. Drops of physiological saline were used to moisturize the vessel area

and a small incision was made in between both the rostral and middle ligatures using microincision scissors. Afterwards, the tip of the presoaked (for 30 min into physiological saline solution) high fidelity 1.4F micromanometer catheter (Millar Instruments, Houston, USA), was inserted in the caudal direction into the vein, using a bent 27-gauge needle, followed by gently securing the middle suture. Simultaneously, the caudal suture was released, and the catheter was quickly advanced into the right atrium and then RV. After stabilization of the signal, the pressure was recorded. During the data collection, the ventilator was shut off for a few seconds to acquire data without lung motion artifact. The parameters measured were heart rate, RV systolic pressure (RVSP) and end-diastolic pressure (RVEDP). At the conclusion of the measurements, the catheter was removed by gently pulling it back and was immediately placed into a syringe filled with saline to prevent clotting. Parotid glands were moved aside and the thin muscle layer around the throat were bluntly dissected with forceps to expose and isolate the right carotid artery. A suture was secured around the distal end of the artery, then gently pulled and taped to the table. An additional suture was inserted beneath carotid artery and a very loose knot was placed. A Biemer microvessel clip (Aesculap, Tuttlingen, Germany) was placed on the proximal part of the carotid artery. A couple of drops of physiological saline were put in the vessel area and a tiny incision was made near the distal end of the artery with a microincision scissors. Using a bent 27-gauge needle, the catheter tip was inserted into the vessel followed by gently securing the second suture. Simultaneously, the clip was released and the high fidelity 1.4F micromanometer catheter (Millar Instruments, Houston, USA) was quickly advanced into the left ventricle until the pressure signal was displayed in the monitor. After stabilization of the signal, the pressure was recorded. All data were collected and analyzed using PowerLab data acquisition systems and LabChart 7 for Windows software (MPVS-Ultra Single Segment Foundation System, AD Instruments, Spechbach, Germany). The parameters measured were heart rate, systolic and mean aortic pressure, left ventricular systolic pressure (LVSP) and end-diastolic pressure (LVEDP). Once measurements were taken, the catheter was removed by gently pulling it back and was immediately placed into a syringe filled with saline to prevent clotting. At the end of the experiment, the mice were sacrificed, and the hearts were harvested for further examination.

6.8 Cardiac tissue harvest and preparation

After hemodynamic measurements, whole heart was dissected from magistral arteries and veins. Further, heart was carefully separated into right ventricle, left ventricle and septum and wet weights were taken to calculate right ventricular hypertrophy index. To calculate RV to tibia length ratio, tibia was separated from either left or right legs and its length was measured. Then, cardiac tissue was snap frozen in liquid nitrogen and stored in -80ºC for molecular biology assessment. For the histological experiments, whole heart was taken arrested at end-diastole. The heart arrest at diastole was achieved by with injection of 1 mL 3M solution of KCL to RV cavity while mouse is under ventilator. Once, heart stopped beating, it was separated from main vessels and immersed in 3.5-3.7% formaldehyde in 50mL falcon tube and kept at room temperate for 24 hours. The next day heart is cut into apex, middle and base parts by blade were transferred to embedding cassettes and stored in phosphate-buffered saline (PBS, pH 7.4) for 48h changing PBS every 24h. Further, cardiac tissues were transferred to 50% ethanol for 24h and subsequently to 70% ethanol. The dehydration was performed overnight in Leica ASP 300S tissue processor. Next day, the cardiac tissues were embedded in 65°C warmed paraffin with the usage of a heated Leica paraffin embedding module. Then, the paraffin-embedded cardiac tissues were cooled down for hardening on a Leica cooling plate followed by sectioning into 3 µm-thickness on Leica fully automated rotation-microtome and mounted on positively charged glass slides. Once, cardiac tissue sections were dried on Leica heating plate at 40°C for 2 – 3 hours, they were incubated at 37°C (for 12 h) in a drying oven before commencing a staining.

6.9 Histology

6.9.1 Picrosirius red staining of right ventricular tissues

Paraffin embedded cardiac cross sections were cut into 3 µm sections onto slides. 0.1% picrosirius red was prepared by dissolving 200 mg Sirius red (Sirius rot F3B, C.I. 35780, Niepötter Labortechnik, Germany) in 200mL saturated picric acid (Picric acid solution 1.2% BioChemica, Lot: 1O004669, AppliChem GmbH, Germany). The pH was

fixed at 2. 1% glacial acetic acid was prepared by dissolving 10ml of glacial acetic acid (Essigsäure, Rotipuran R 100%, p.a., Carl Roth GmbH + Co. KG, Germany) in distilled water. Briefly, sections were deparaffinized and rehydrated in xylol and graded ethanol series (99.9%, 96%, 70%), washed with PBS and dipped in 0.1% picrosirius red solution for an hour. Afterwards, excess of picrosirius staining was washed away with 1% glacial acetic acid series, dehydrated with graded ethanol series of increasing concentration from 70% to absolute alcohol. Finally, slides were cleared in xylol series and mounted in pertex. The percentage of interstitial collagen area fraction was counted using collagen counting Leica Qwin V3 computer-assisted image analysis software (Leica Microsystem, Wetzlar, Germany).

6.9.2 Hematoxylin and eosin staining of right ventricular tissues

Paraffin embedded cardiac cross sections were cut into 3 µm sections onto slides. The sections were deparaffinized in Xylol for 10 min three time and rehydrated first in 99.6% ethanol for 5 min twice, 95% ethanol for 5 min and then in 70% ethanol for 5 min. Then, the sections were kept in distilled water for min and incubated with hematoxylin for 20 min. The slides were washed in tap water for 5 min in a glass cuvette. Further, the slides were kept in 96% ethanol for 1 min. Afterword, slides were kept in Eosin (0.1%) solution for 4 min. The stained slides were rinsed briefly in distilled water. Subsequently, the stained sections were dehydrated in 96% ethanol for 2 min twice, 100% ethanol for 5 min, 99.8% isopropanol 99.8 for 5 min and finally in xylol for 5 min three times. Mounting gel was added to the tissue sections and a cover slip was placed carefully on the gel avoiding bubbles and were left to dry overnight. To investigate cardiomyocyte size, H&E stained cardiomyocytes were measured, and the average value was calculated as the average area of myocytes per sample. All these measurements were performed using ImageJ software (National Institutes of Health, Bethesda, MD, USA).

6.10 Real Time polymerase chain reaction (RT-PCR)

6.10.1 RNA isolation

Total RNA from frozen mouse tissues was obtained using the QIAGEN RNeasy® Mini kit (QIAGEN, Hilden, Germany) following the manufacturer's instructions. The quality and concentration of RNA was measured by Nanodrop ND-1000 Spectrophotometer (Thermo Scientific, Waltham, MA) and the probes were snap frozen and kept at -80 °C till further use.

6.10.2 Complementary DNA synthesis

cDNA was synthesized by RT-PCR using Bio-Rad iScript cDNA synthesis kit according to the manufacturer's instructions. 1.0 µg RNA in 20 µl mastermix was prepared according to the protocol. The reverse transcription reactions were subjected to cDNA synthesis by firstly annealing at 25°C for 5 min and incubating at 42°C for 30 min, followed by thermal inactivation of reverse transcriptase at 85°C for 5 min. The cDNA was stored at -20°C.

6.10.3 Quantitative real time - polymerase chain reaction (qRT-PCR)

The intron-spanning primer pairs were designed using the Primer3 program were cross checked to ensure the specificity by blasting to the whole genome. The product size was within the range of 80 bp-280 bp.
qRT- PCR was performed on a Mx3000P® QPCR system machine using SYBR® iTaq SYBR Green Supermix with Rox kits according to manufacturer's instructions. The cDNA was omitted for the negative control. The annealing temperature for every gene was 59°C. By using the MxPro™ QPCR software, a dissociation curve was generated for each gene to ensure a single product amplification and the threshold cycle (Ct values) for each gene was determined.

Table 4. Primer used for RT-PCR

Gene	Forward	Reverse	Design
S18rRNA	CGTGAGTTCTCCAGCCCTCT	CTTCGCCATCACTGCCATTA	own
Spp1	ACAGGAAGAACAGAAGCAAAG	GGTCAACTAAAGAAGAGGCAA	own
Cd44	TGGTGGCACACAGCTTGGGG	GTCAGCTGCCTCAGTCCGGG	[133]
Itgb3	GGAAGCAGCGCCCAGATCAC	TTGTCCACGAAGGCCCCAAA	[133]
Itgav	CCGTGGACTTCTTCGAGCC	CTGTTGAATCAAACTCAATGGGC	[134]
Itgb1	CTACTTCTGCACGATGTGATGAT	TTGGCTGGCAACCCTTCTTT	[134]
Itgb3	CCACACGAGGCGTGAACTC	CTTCAGGTTACATCGGGGTGA	[134]
Itgb5	GAAGTGCCACCTCGTGTGAA	GGACCGTGGATTGCCAAAGT	[134]
Itgb8	CTGAAGAAATACCCCGTGGA	ATGGGGAGGCATACAGTCT	[134]
Itga1	CCTTCCCTCGGATGTGAGTCA	AAGTTCTCCCCGTATGGTAAGA	[135]
Itga2	TGTCTGGCGTATAATGTTGGC	CTTGTGGGTTCGTAAGCTGCT	[135]
Itga3	CCTCTTCGGCTACTCGGTC	CCGGTTGGTATAGTCATCACCC	[135]
Itga4	GATGCTGTTGTTGTACTTCGGG	ACCACTGAGGCATTAGAGAGC	[135]
Itga5	CTTCTCCGTGGAGTTTTACCG	GCTGTCAAATTGAATGGTGGTG	[135]
Itga7	CTGCTGTGGAAGCTGGGATTC	CTCCTCCTTGAACTGCTGTCG	[135]
Itga8	CGAAGCCGAACTCTTTGTTATCA	GGCCTCAGTCCCTTGTTGT	[135]
Itgav	CCGTGGACTTCTTCGAGCC	CTGTTGAATCAAACTCAATGGGC	[135]
Itgb1	ATGCCAAATCTTGCGGAGAAT	TTTGCTGCGATTGGTGACATT	[135]
Itgb3	CCACACGAGGCGTGAACTC	CTTCAGGTTACATCGGGGTGA	[135]
Itgb4	GCAGACGAAGTTCCGACAG	GGCCACCTTCAGTTCATGGA	[135]

6.10.4 RT-PCR data analysis

Data obtained from the PCR machine were Ct value, which referred to the cycle number where the PCR curve reached the threshold in the linear part of the curve. Higher Ct value indicates less mRNA detected. 18S ribosomal RNA (18SrRNA) or

GAPDH was used as endogenous reference, and thus expression of tested gene was normalized against S18rRNA/GAPDH expression. ΔCt referred to relative gene expression compared with S18rRNA expression. $\Delta Ct = Ct^{housekeeping\ gene} - Ct^{tested\ gene}$.

6.11 ELISA

Blood samples were collected from apical puncture of the right ventricle after terminal hemodynamic measurements, and were centrifuged and plasma fraction was separated, stored at -80 °C. Plasma osteopontin was measured by ELISA according to the instructions of the manufacturer (R&D systems, Inc., Minneapolis, USA).

6.12 Statistical analysis

Data were plotted as individual data points with mean in addition. Statistical analysis was performed in GraphPad Prism Version 7 (GraphPad Software Inc., SanDiego, CA, USA) using two-tailed unpaired Student's t-test for experiments with two groups or one-way ANOVA with Dunnett´s multiple comparison test for time-course experiments or two-way ANOVA with Sidak's correction for post-hoc multiple comparisons for experiments including multiple groups. Kaplan-Meier survival analysis was used to determine risk of mortality following the PAB procedure. A P value less than 0.05 was considered statistically significant. In the figures, asterisks denote statistical significance (*P < 0.05; **P < 0.01; ***P < 0.001; ****P < 0.0001). Figures were assembled using Adobe Illustrator CC 2017.

7 RESULTS

7.1 Osteopontin and its receptors

7.1.1 Osteopontin and its receptors in the right ventricle of PAB mice

Although, our initial motivation and hypothesis to start the current study mostly were based on the divergent role of osteopontin in other diseases, specifically in various cardiac diseases and lack of knowledge on its role in RV remodeling in afterload-independent models namely in PAB model as discussed in the introduction section. Thus, to validate our hypothesis and to start *in vivo* experiments, we performed several experiments including RT-PCR and ELISA using extra samples left from previous studies (approval number B2/244) published elsewhere in the form of original articles [136, 137].

Firstly, we performed RT-PCR experiments to evaluate expression levels of osteopontin, CD44 and various integrin receptors in RV tissues taken from sham and PAB mice at days 3, 7, 14 and 21 post-surgery (**Figure 11 and Figure 12**). The results of our experiments showed that RV osteopontin mRNA expression was increased at all time-points of PAB compared to sham, the highest expressions being detected in the initial stages of RV remodeling (day 3 after PAB). While, mRNA expressions of CD44 and integrins including α2, α4, α7, αV, β1, β5 and β8 were increased in earlier stages of PAB (days 3, 7 and 14). However, at 21 day after PAB only integrins α2, α4 and β3 remained significantly upregulated, while αV, β1, β5 and β8 returned to baseline levels and α7 downregulated (**Figure 11 and Figure 12**).

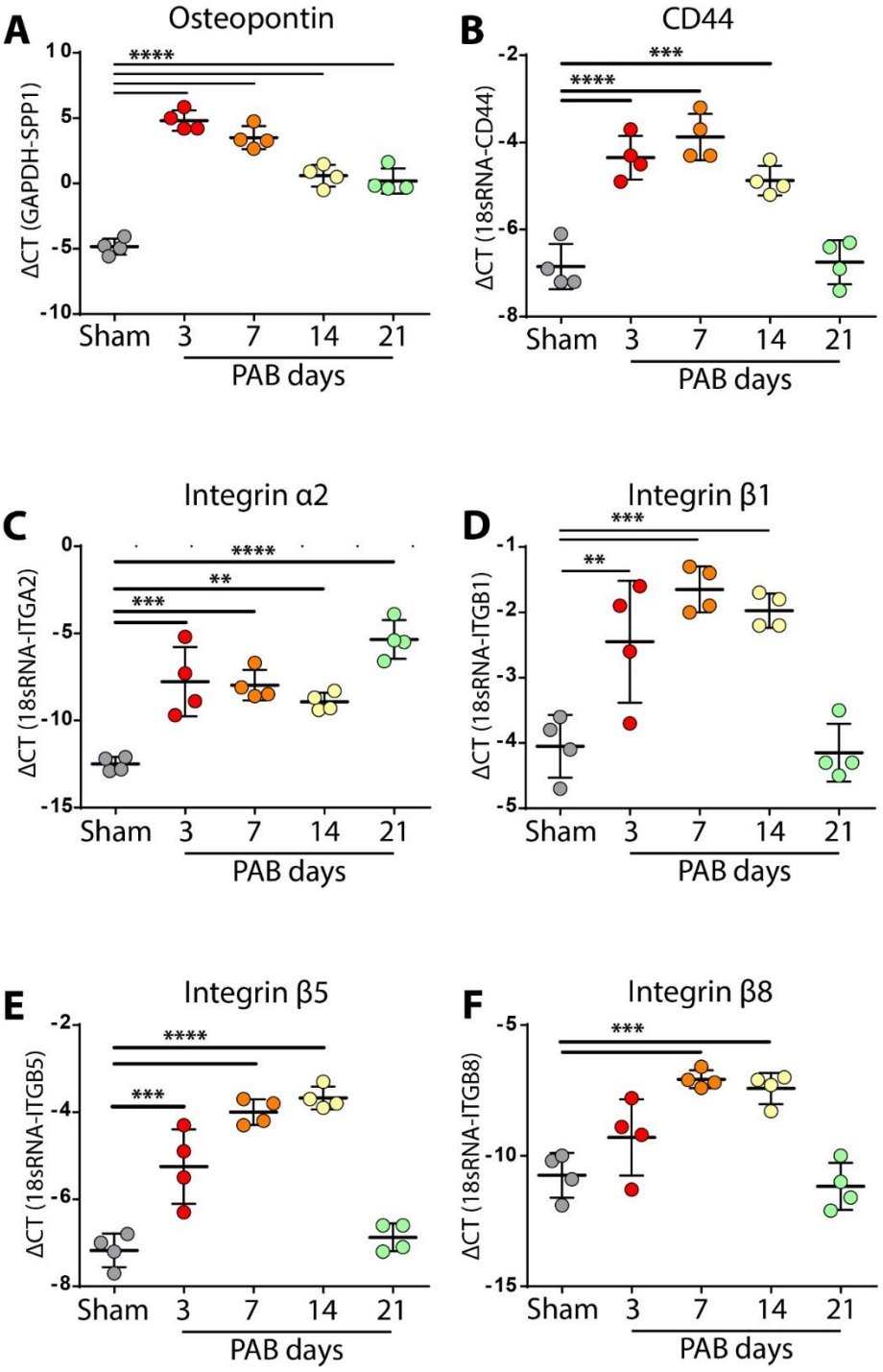

Figure 11. Time course of the right ventricular mRNA gene expression of osteopontin and its receptors in sham and PAB mice.

A) Osteopontin (SPP1), B) CD44, C) Integrin α2 (ITGA2), D) Integrin β1 (ITGB1), E) Integrin β5 (ITGB5), F) Integrin β8 (ITGB8). Data are given as scatter dot plots, and lines are means and standard deviations. Differences were assessed by one-way ANOVA and Dunnett´s multiple comparison test; **P < 0.01; ***P < 0.001; ****P < 0.0001.

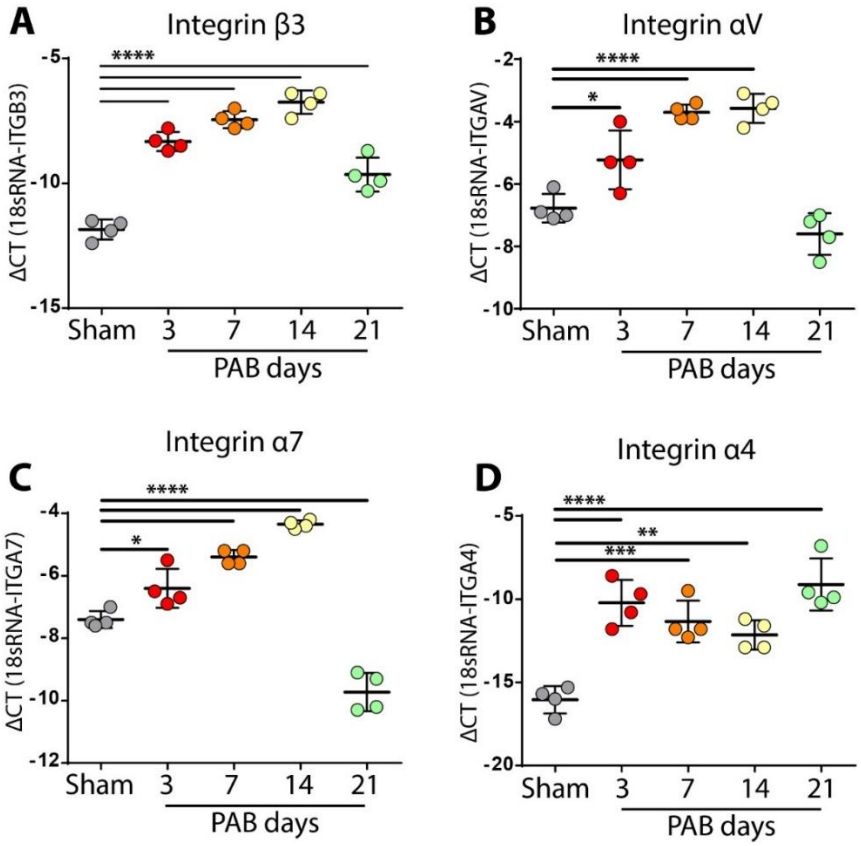

Figure 12. Time course of the right ventricular mRNA gene expression of osteopontin receptors in sham and PAB mice.

A) Integrin β3 (ITGB3), B) Integrin αV (ITGAV), C) Integrin α7 (ITGA7), D) Integrin α4 (ITGA4), E) Integrin β5 (ITGB5), F) Integrin β8 (ITGB8). Data are given as scatter dot plots, and lines are means and standard deviations. Differences were assessed by one-way ANOVA and Dunnett´s multiple comparison test; *P < 0.05; **P < 0.01; ***P < 0.001; ****P < 0.0001.

7.1.2 Circulating osteopontin in PAH and RV remodeling models

Further, we evaluated the circulating levels of osteopontin in the plasma samples taken from various rat and mouse models of pulmonary hypertension and RV remodeling (**Figure 13**). Plasma levels of osteopontin were not changed in hypoxia exposed mice (3 weeks) and rats (5 weeks) and SU5416/hypoxia exposed rats (5 weeks); however, in monocrotaline treated rats, plasma osteopontin levels were significantly decreased compared to healthy control rats. While, circulating osteopontin levels were increased PAB mice compared to sham mice reaching the peak on day 14 of post-operation (**Figure 13**).

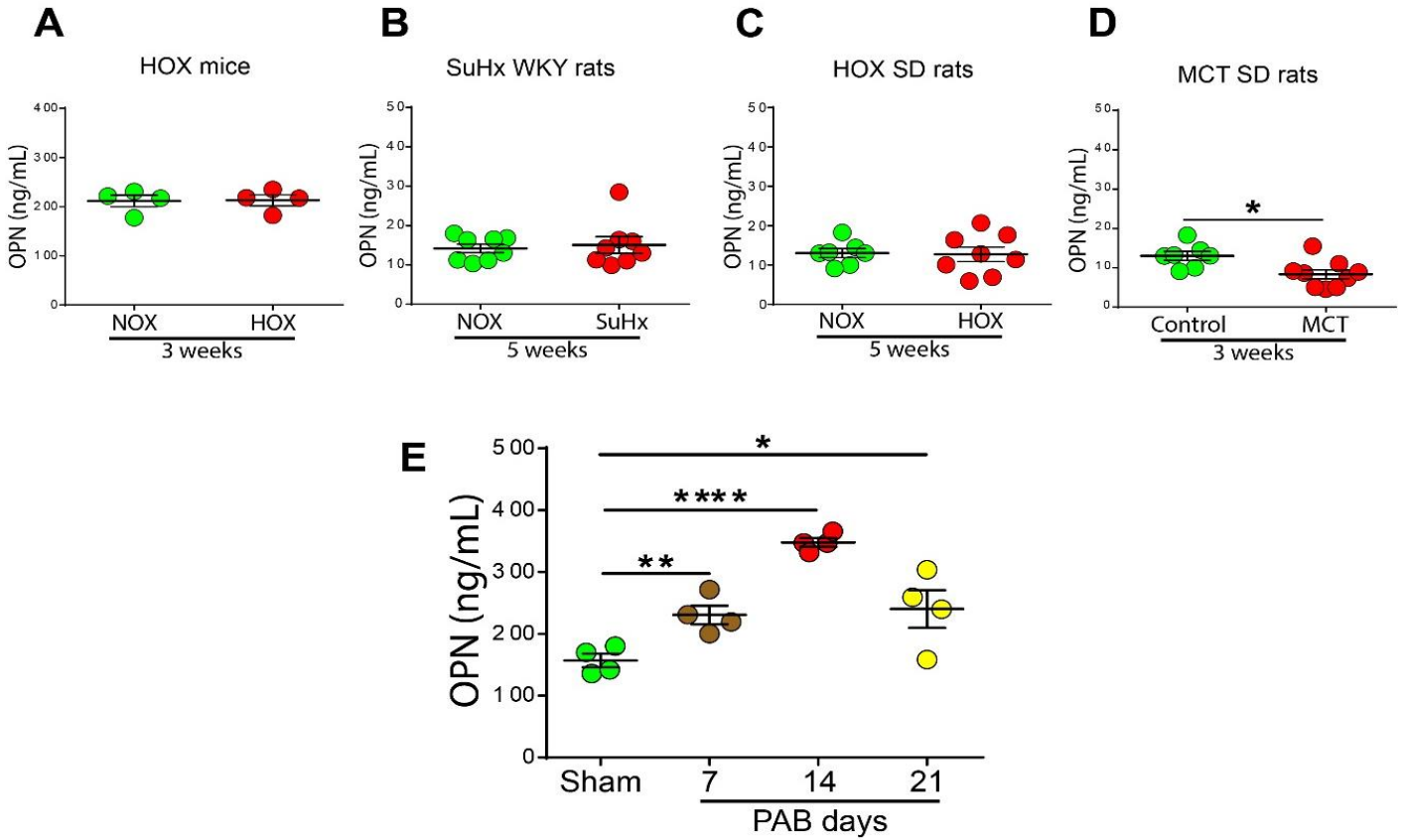

Figure 13. Plasma levels of osteopontin in various animal models of pulmonary hypertension and right ventricular remodeling.

A) Plasma osteopontin in hypoxia exposed (HOX) mice (3 weeks). B) Plasma osteopontin in SU5416/hypoxia (SuHx) rats (5 weeks). C) Plasma osteopontin hypoxia exposed (HOX) rats (5 weeks). D) Plasma osteopontin in monocrotaline treated (MCT) rats (3 weeks). E) Plasma osteopontin in sham and PAB operated mice at different time-points of 3 week. Data are given as scatter dot plots, and lines are means and standard deviations. Student's t test was performed to determine significance between two groups. Differences at various time points were assessed by one-way ANOVA with Dunnett´s multiple comparison test; *P < 0.05; **P < 0.01; ***P < 0.001; ****P < 0.0001.

7.2 Pulmonary artery banding study

7.2.1 Body weights and survival

Baseline measurements revealed that body weights (BWs) of OPN KO mice were significantly higher than that of WT mice. All PAB-operated mice, regardless of the genetic background or treatment group, drastically lost BW within the first week of post-surgery; WT mice reaching peak on day 3, KO mice reaching peak on day 6 (**Figure 15)**. Sham-operated mice showed gradual increase in their BWs over the course of the experiment, while BWs of PAB-operated mice remained on plateau over the course of the disease showing a slight trend towards increasing starting from second week of post-surgery. WBs taken on the last day of experiment before commencing hemodynamic measurements, revealed that all PAB-operated mice had significantly lower BW compared to sham-operated mice regardless genetic background or osteopontin treatment (**Figure 15**).

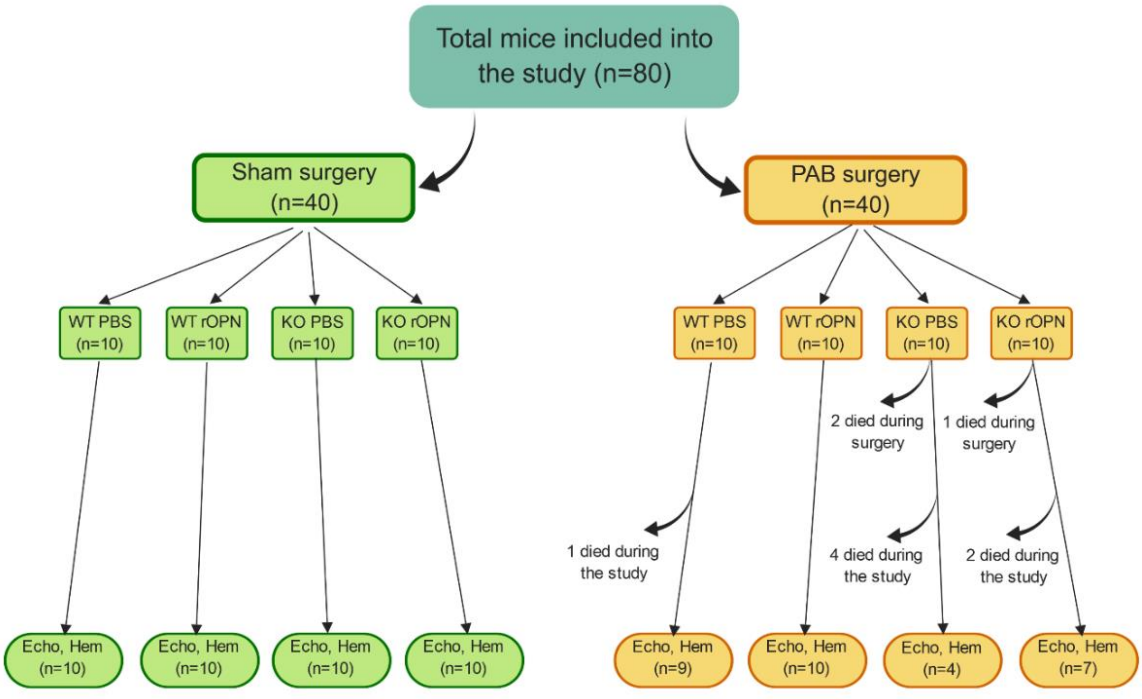

Figure 14. Flowchart of mouse allocation to different groups.

PAB, pulmonary artery banding; WT, wildtype; KO, osteopontin knockout; PBS, phosphate-buffered saline; rOPN, recombinant mouse osteopontin; Echo, echocardiographic measurements; Hem, hemodynamics measurement.

None of the sham-operated mice died during surgery and over the course of the experiment. In PAB groups, 3 OPN KO mice died during PAB surgery. During the

course of the disease development in PAB-operated mice; None of the mice died in WT mice treated with rOPN; 1 mouse died in WT mice treated with PBS; 2 mice died in OPN KO mice treated with rOPN; 4 mice died in OPN KO mice treated with PBS (**Figure 14, Figure 15**).

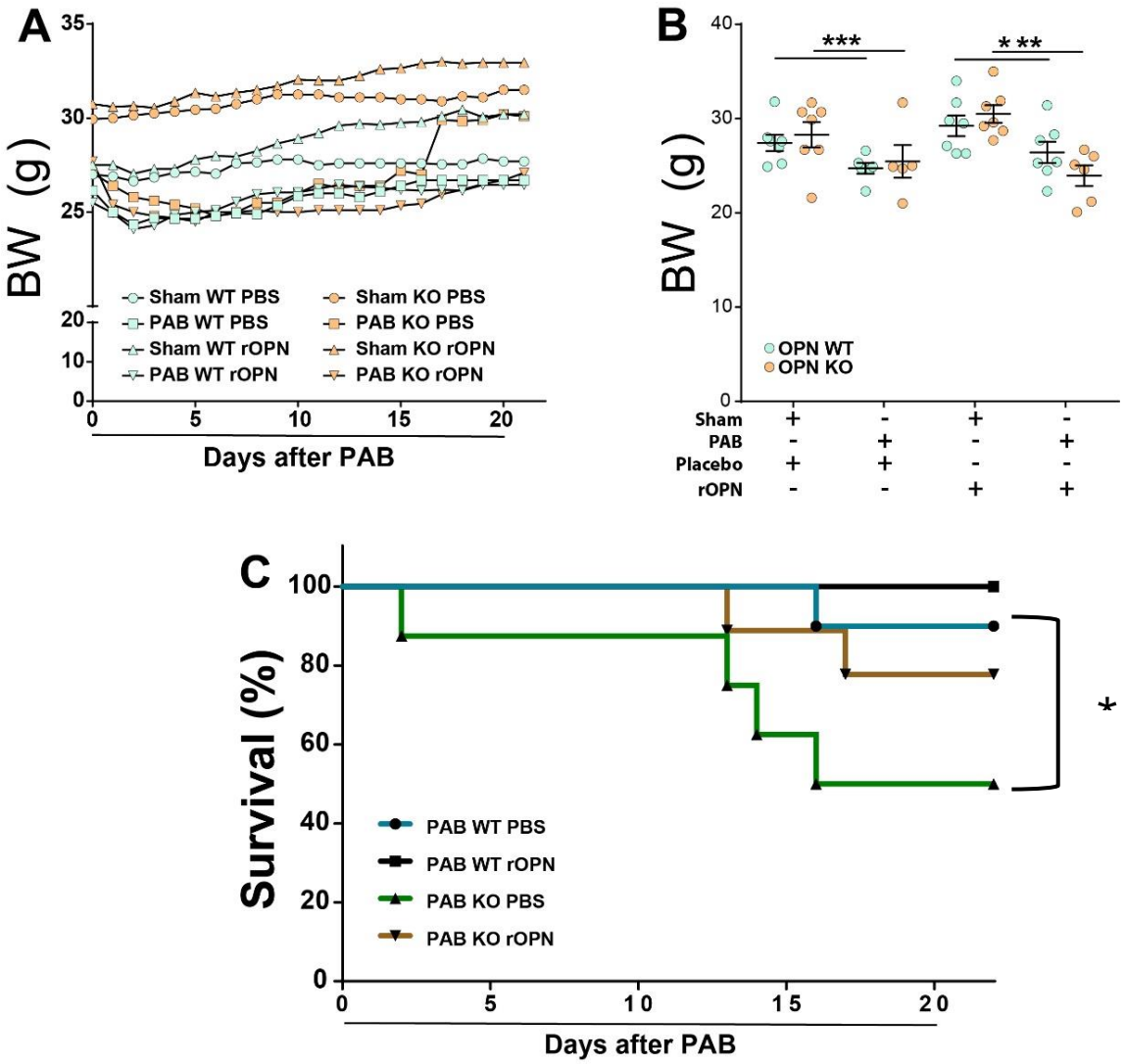

Figure 15. Body weight and survival of PAB mice.

A) Body weight of mice over the course of the study. B) Body weight of mice taken after 21 days of sham or PAB surgery. C) Kaplan-Meier survival curve demonstrates increased post-pulmonary artery banding (PAB) mortality in PBS-treated OPN KO mice compared with wildtype (WT), which was attenuated by rOPN treatment (21 day survival: WT mice treated with PBS 9 of 10; WT mice treated with rOPN 10 of 10; OPN KO mice treated with PBS 4 of 8; OPN KO treated with rOPN 2 of n=9) Data (B) are given as scatter dot plots, and lines are means and standard error of the mean. Differences were assessed by two-way ANOVA and Sidak's multiple comparison test; *P < 0.05; **P < 0.01; ***P < 0.001; ****P < 0.0001.

7.2.2 Baseline cardiac functions

Baseline measurements were taken one day before performing sham or PAB surgery. At baseline, OPN KO mice had significantly higher BWs compared to WT mice (**Figure 16, A**). Heart rate (HR) values were similar between WT and OPN KO mice (**Figure 16, B**). OPN KO mice had higher CO values compared to WT mice (**Figure 16, C**); however, when CO was corrected to either BW (**Figure 16, D**) or body surface area (BSA) (**Figure 16, E**), there were no significant differences in cardiac indexes (CI) between KO and WT mice. There were also no differences in other right ventricular structural and functional parameters such as right ventricular internal diameter (RVID) (**Figure 16, F**), right ventricular wall thickness (RVWT) (**Figure 16, G**) and tricuspid annulus plane systolic excursion (TAPSE) (**Figure 16, H**). Tricuspid annulus systolic velocity (RV S`) was significantly higher in OPN KO mice compared to WT mice (**Figure 16, I**); however, when RV S´ was corrected to BW, there was no difference between KO and WT mice (**Figure 16, J**).

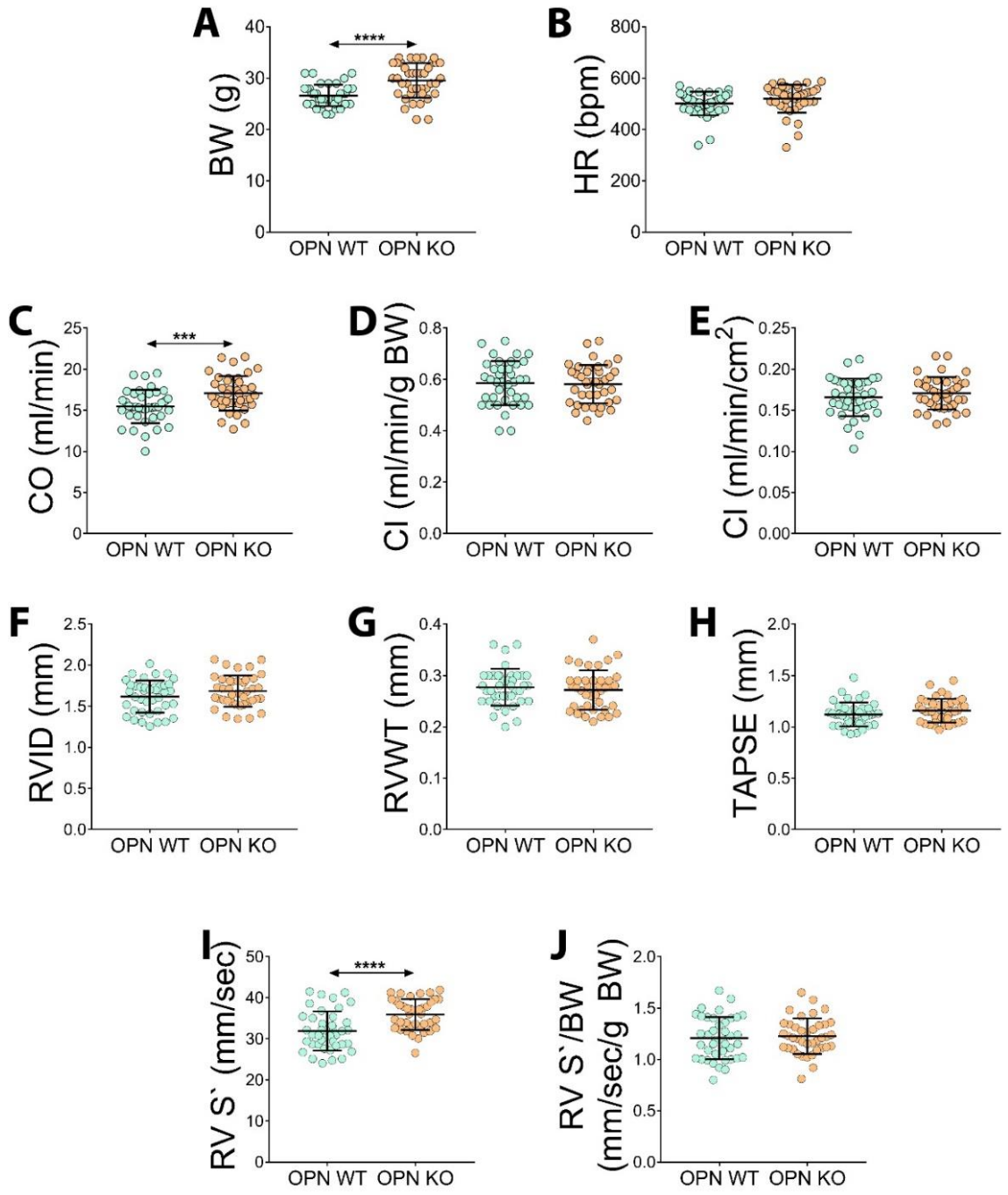

Figure 16. Baseline characteristics of osteopontin wildtype and knockout mice.

Measurements were taken one day before sham or PAB surgery. A) Body weight (BW, g), B) Heart rate (HR, bpm), C) Cardiac output (CO, ml/min), D) Cardiac index (CO corrected to BW) (CI, ml/min/g BW), E) Cardiac index (CO corrected to body surface area) (CI, ml/min/cm^2). PBS, phosphate-buffered saline; rOPN, recombinant mouse osteopontin. Student's t test was performed to determine significance; ***P < 0.001; ****P < 0.0001.

7.2.3 Systemic and pulmonary hemodynamics

Invasive hemodynamics measurements of systemic and pulmonary circulation were performed on the last day of 21-day experiment. On day 21 after sham or PAB surgery, mice from all groups had similar values of left ventricular systolic pressure (LVSP) and HR, regardless of their genetic background and osteopontin treatment (**Figure 17**, **A and B**). PAB surgery resulted in significantly increased right ventricular systolic pressure (RVSP) in both OPN KO and WT mice without being changed by osteopontin treatment (**Figure 17**, **C**). Similarly, PAB-operated mice displayed increased right ventricular end diastolic pressure (RVEDP) (**Figure 17**, **D**). However, PAB-operated OPN KO mice treated with PBS had significantly lower values of RVEDP compared to WT littermates (**Figure 17**, **D**), while osteopontin treated OPN KO PAB mice had similar RVEDP compared to WT littermates.

Echocardiographic examination showed that, PAB-surgery resulted in markedly increased pressure gradient between pre- and post-stenotic region of the pulmonary trunk with pressure gradient values being beyond the capacity of pulsed wave Doppler to detect observed blood flow velocity (**Figure 18, A and B**). Similarly, increased RVSP in PAB-operated mice from all groups resulted in marked tricuspid regurgitation shown from the apical four chamber view with both color and pulsed wave Doppler imaging (**Figure 18, C and D**).

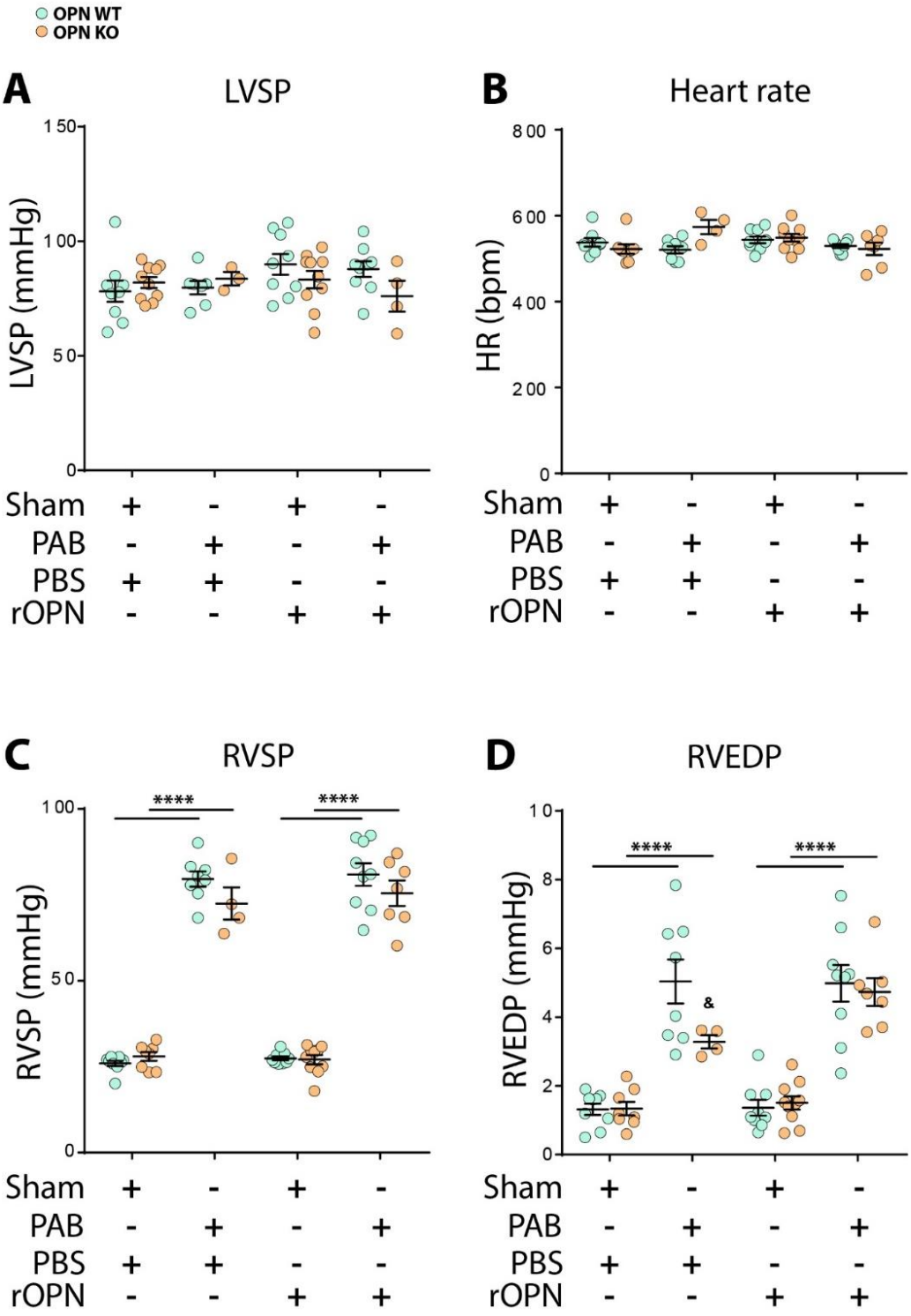

Figure 17. Invasive hemodynamic parameters.

A) Left ventricular systolic blood pressure (LVSP, mmHg), B) Heart rate (HR, beats per minute (bpm)), C) Right ventricular systolic pressure (RVSP, mmHg), D) Right ventricular end diastolic pressure (RVEDP, mmHg). PBS, phosphate-buffered saline; rOPN, recombinant mouse osteopontin; WT, wild type mice; OPN KO, osteopontin knockout mice. Data are given as scatter dot plots, and lines are means and standard errors of the mean. Differences were assessed by two-way ANOVA and Sidak's multiple comparison test; ****P < 0.0001.

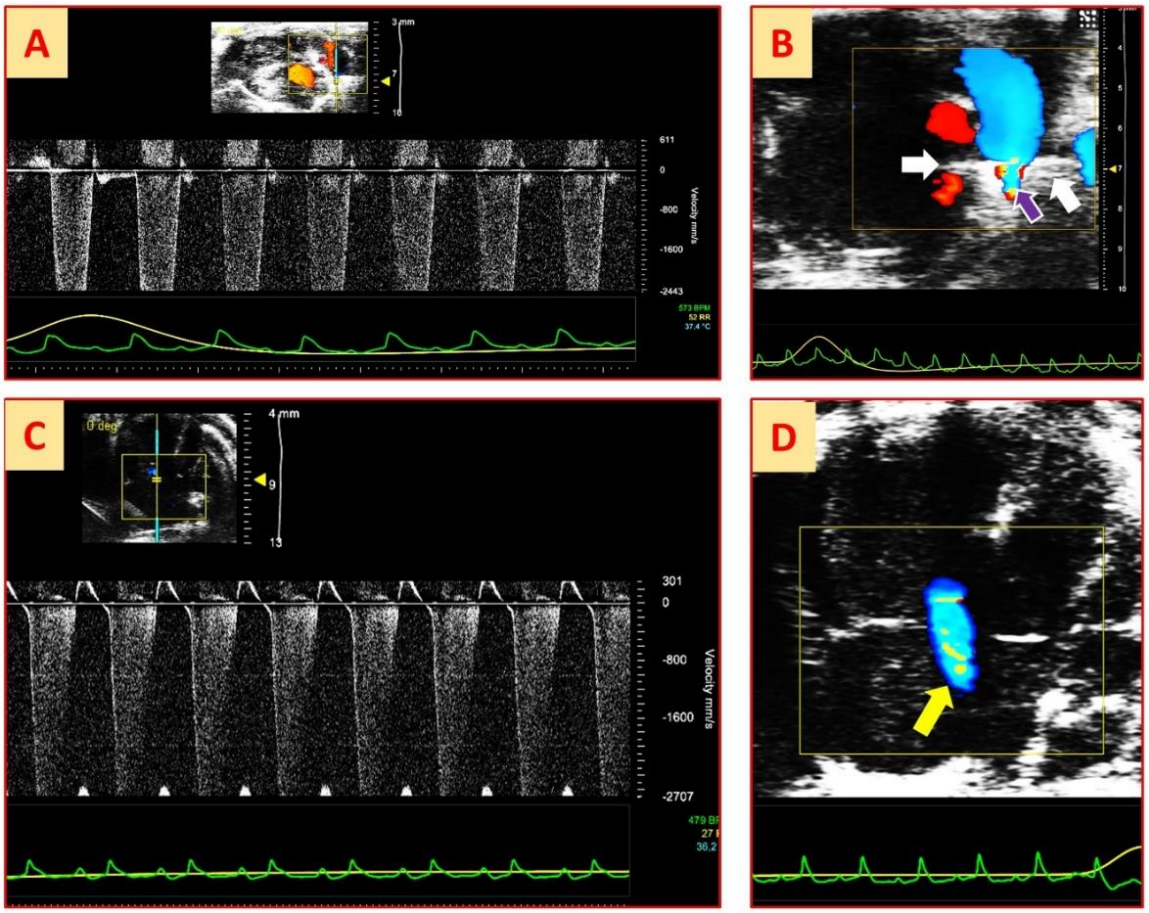

Figure 18. Pulsed wave and color Doppler Imaging of the pulmonary trunk blood flow and tricuspid regurgitation.

A) PW Doppler imaging of the blood flow through the pulmonary trunk stenosis from the parasternal short axis view, B) Color Doppler imaging of the blood flow through the pulmonary trunk stenosis from the parasternal short axis view; white arrows – echogenic shadows of the titanium clip; violet arrow – turbulent blood flow through the stenosis, C) PW Doppler of the tricuspid regurgitation from the apical four chamber view, D) Color Doppler imaging of the tricuspid regurgitation from the apical four chamber view; yellow arrow – regurgitant blood flow

7.2.4 Right ventricular remodeling and dysfunction

All PAB-operated mice developed severe right ventricular hypertrophy as evident with significantly increased Fulton index (right ventricular mass divided by left ventricular mass plus septum mass) (**Figure 19**, **A**), RV mass to tibia length ratio (**Figure 19**, B) and RV mass to BW ratio (**Figure 19**, **C**), which was not effected by the genetic background and osteopontin treatment. In addition, PAB-surgery also caused marked dilatation of right atrial (RA) as seen in open chest cavity after terminal hemodynamic measurements (**Figure 20**).

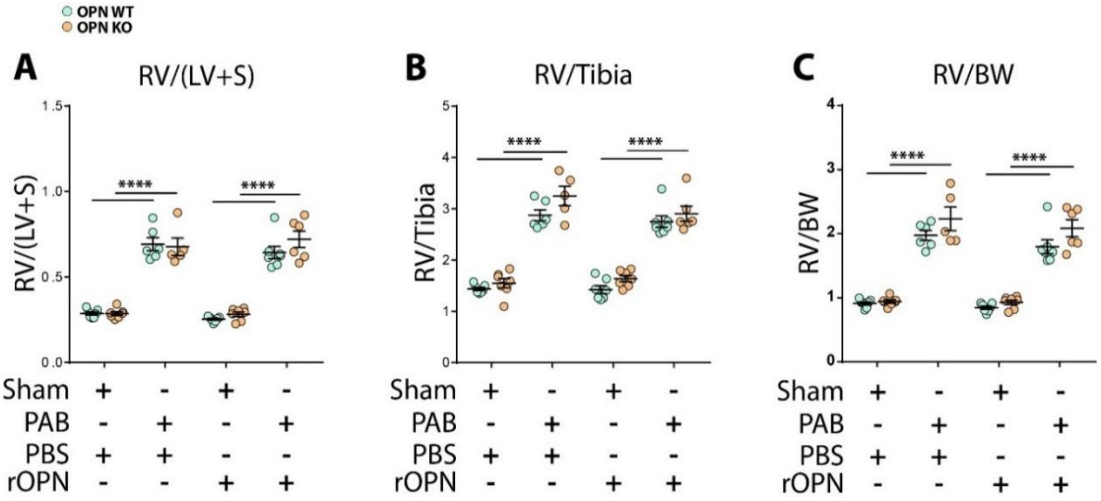

Figure 19. Right ventricular hypertrophy.

A) The ratio of right ventricular mass (mg) to left ventricular mass (mg) plus septum mass (mg). B) The ratio of right ventricular mass (mg) to tibia length (mm). C) The ratio of right ventricular mass (mg) to body weight (g). Sham, sham operation; PAB, pulmonary artery banding; PBS, phosphate-buffered saline; rOPN, recombinant mouse osteopontin; WT, wild type mice; OPN KO, osteopontin knockout mice. Data are given as scatter dot plots, and lines are means and standard errors of the mean. Differences were assessed by two-way ANOVA and Sidak's multiple comparison test; ****P < 0.0001.

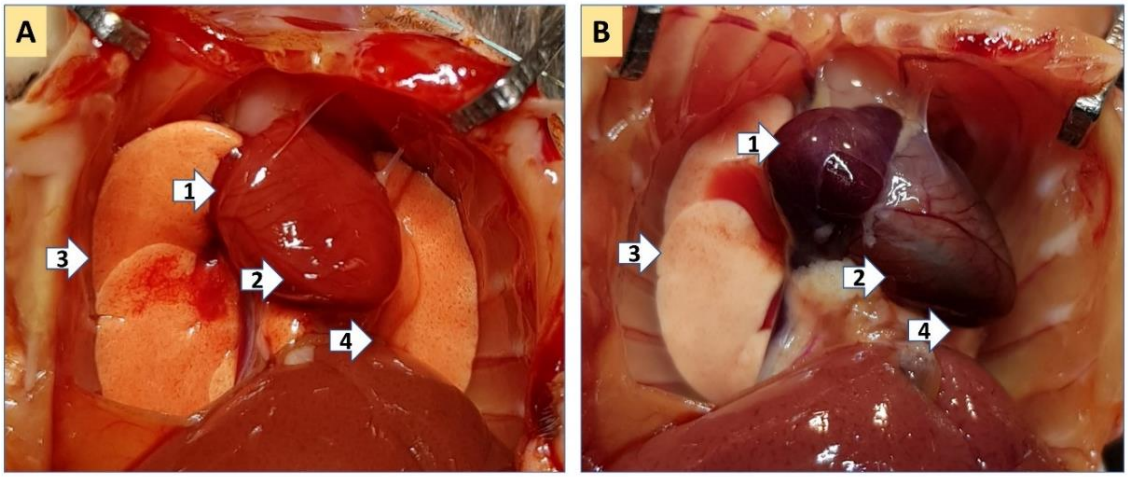

Figure 20. Macroscopic view of the chest cavities of sham- and PAB operated mice.

Chest was opened after terminal hemodynamic measurements were taken and before collecting blood samples from the heart after 21 days of sham or PAB operation. A) sham-operated mouse chest cavity, B) PAB-operated mouse chest cavity; 1 – right atrium, 2 – right ventricle, 3 – right lung and 4 – left lung.

All terminal echocardiographic examination was taken one day before hemodynamics measurements. PAB surgery also caused severe RV dilatation as shown by increased RVID measured from apical four chamber view on echocardiographic examination after 21 days of post-surgery (**Figure 21, A**). Apart from apical four chamber view (**Figure 22, A and C**), RV dilatation was also seen from other echocardiographic views such as left parasternal long axis view (**Figure 22, B and D**) and parasternal short axis views at the level of papillary muscles (**Figure 23, A and B**). Both genetic background and osteopontin treatment had no effects on RV dilatation values.

In all PAB groups, mice developed significantly increased right ventricular wall thickness (RVWT) (**Figure 21, B**) (**Figure 23, C and D**), which was not changed with neither genetic background nor osteopontin treatment.

Histological examination of right ventricular tissues with Sirius red (SR) and hematoxylin and eosin (H&E) staining revealed that all PAB mice developed marked increase of RV myocardial fibrosis and cardiomyocyte hypertrophy compared to sham mice (**Figure 24**); however, neither genetic background nor osteopontin treatment influenced on those parameters.

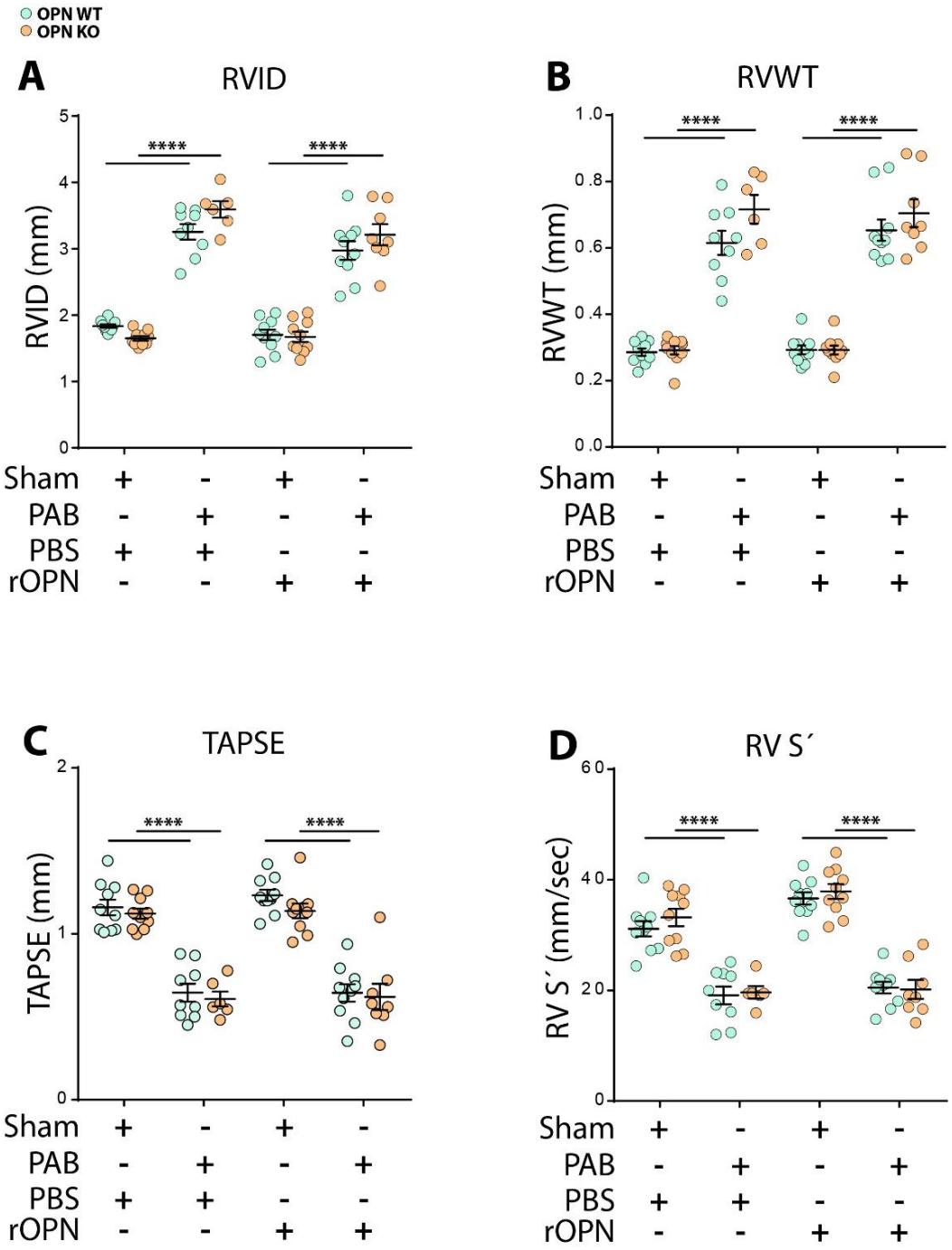

Figure 21. Echocardiographic parameters of right ventricular structure and function.

A) Right ventricular internal diameter (RVID) (mm). B) Right ventricular wall thickness (RVWT) (mm). C) Tricuspid annulus plane systolic excursion (TAPSE) (mm). D) Right ventricular annulus systolic velocity (RV S´) (mm/sec). Sham – sham operation; PAB, pulmonary artery banding; PBS, phosphate-buffered saline; rOPN, recombinant mouse osteopontin; WT, wild type mice; OPN KO, osteopontin knockout mice. Data are given as scatter dot plots, and lines are means and standard errors of the mean. Differences were assessed by two-way ANOVA and Sidak's multiple comparison test; ****P < 0.0001.

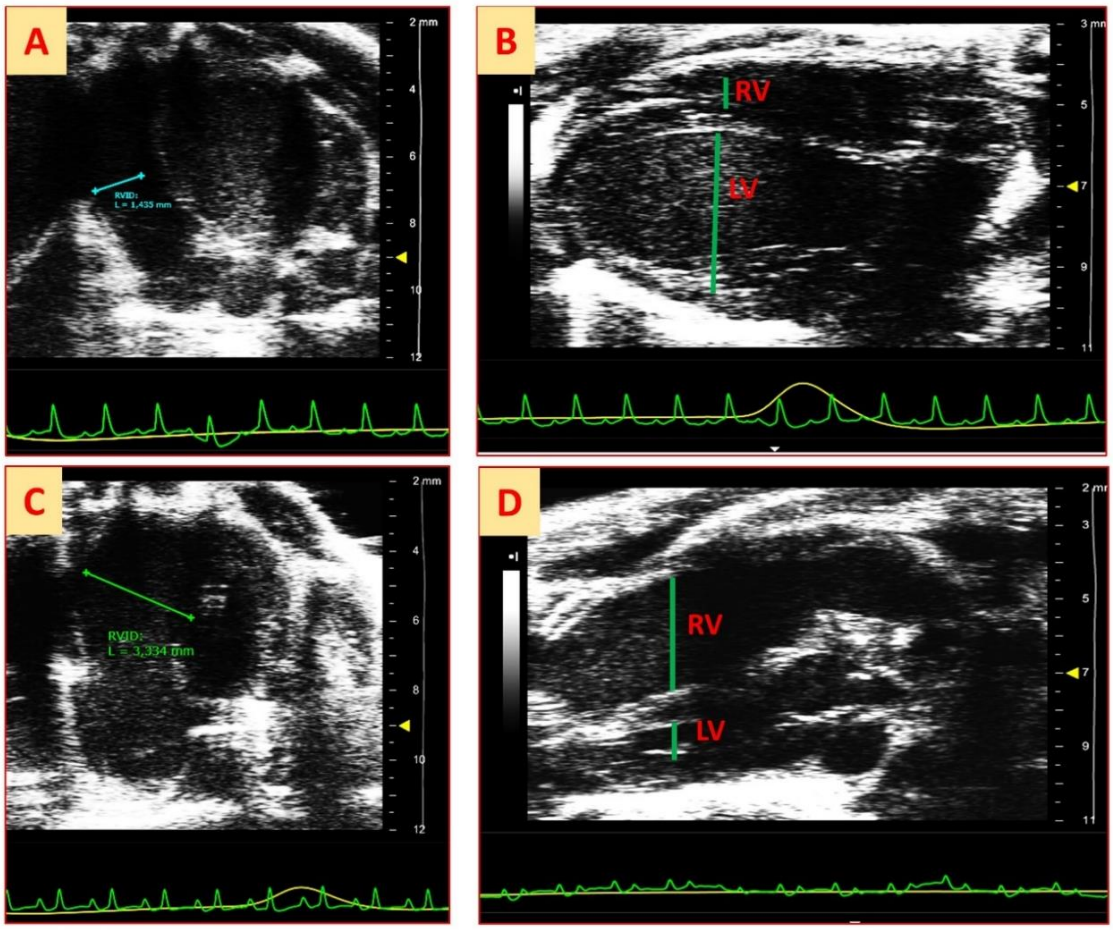

Figure 22. Measurements of right ventricular dilation.

A) Right ventricular internal diameter measured at end-diastole from the apical four chamber view in a sham-operated mouse after 21 days, B) Internal dimeters of left and right ventricles measured at end-diastole from the parasternal long-axis view in a sham-operated mouse after 21 days, C) Right ventricular internal diameter measured at end-diastole from the apical four chamber view in a PAB-operated mouse after 21 days, D) Internal dimeters of left and right ventricles measured at end-diastole from the parasternal long-axis view in a PAB-operated mouse after 21 days.

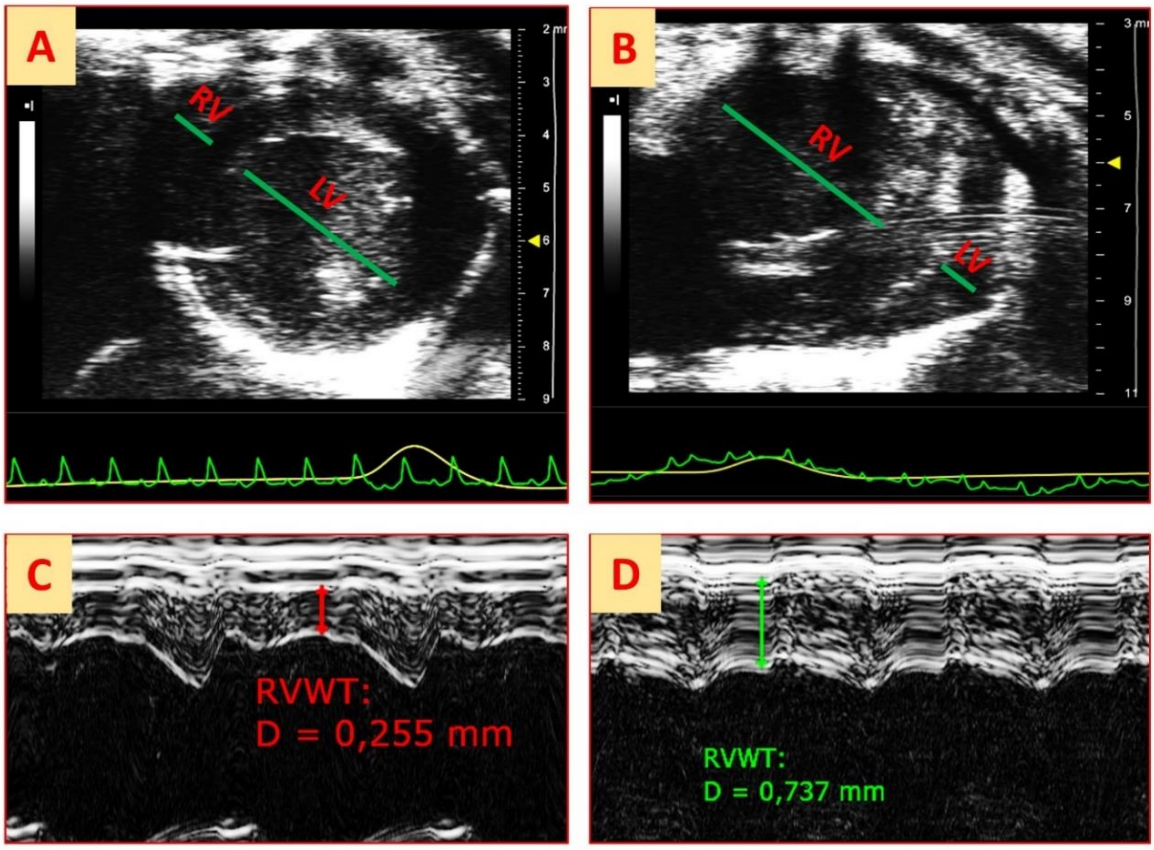

Figure 23. Measurements of right ventricular dilation and wall thickness.

A) Internal dimeters of left and right ventricles measured at end-diastole from the parasternal short-axis view at papillary muscle level in a sham-operated mouse at 3 weeks, B) Internal dimeters of right and left ventricles measured at end-diastole from the parasternal short-axis view at papillary muscle level in a PAB-operated mouse at 3 weeks, C) Right ventricular wall thickness measured at end-diastole from the right parasternal long-axis view in a sham-operated mouse, D) Right ventricular wall thickness measured at end-diastole from the right parasternal long-axis view in a PAB-operated mouse.

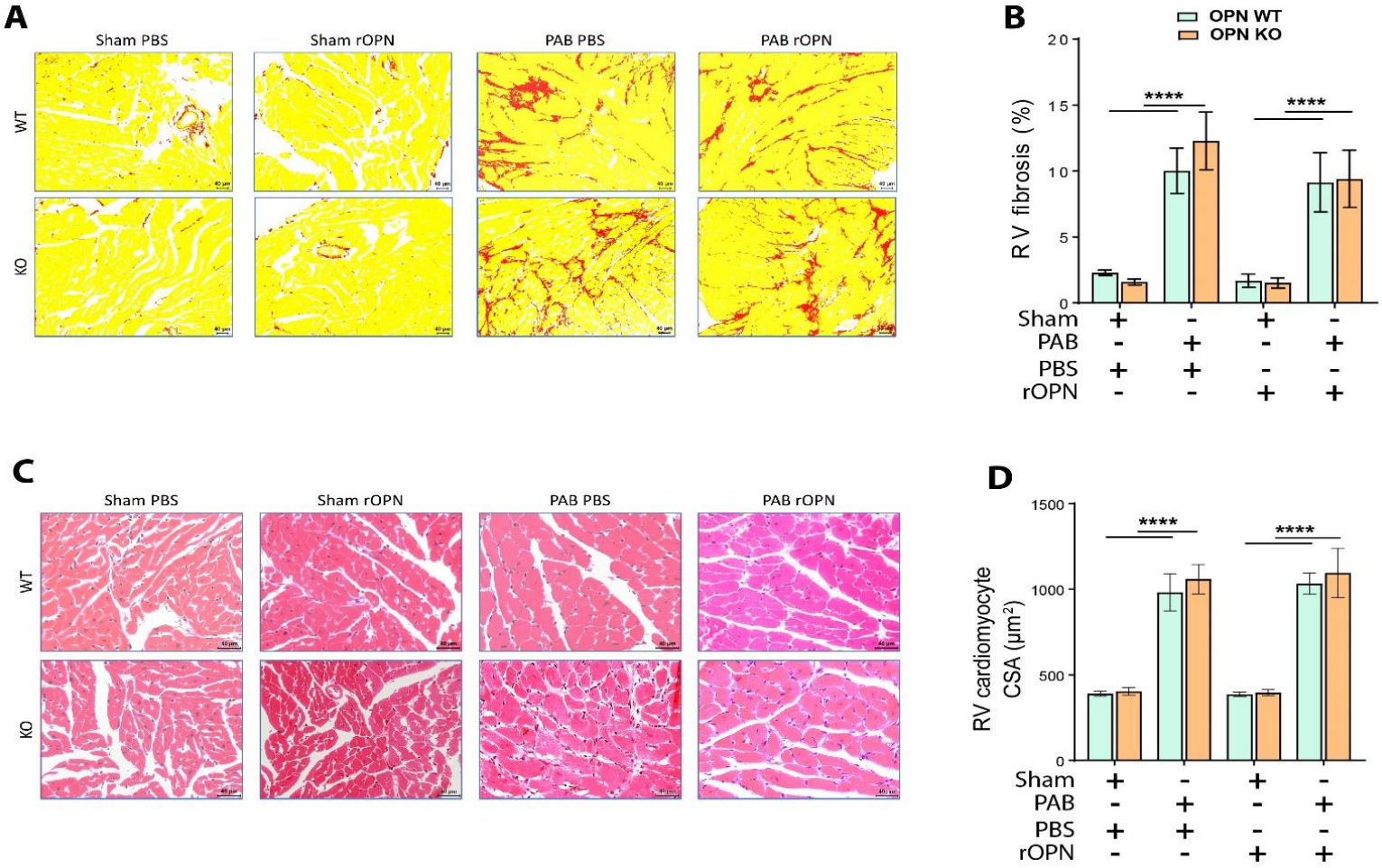

Figure 24. Measurements of right ventricular fibrosis and cardiomyocyte hypertrophy.

A) Representative pictures of the RV myocardial fibrosis. B) Quantitative results of the RV myocardial fibrosis. C) Representative pictures of the RV cardiomyocyte cross sectional area (CSA). D) Quantitative results of the RV cardiomyocyte CSA measurements. PBS, phosphate-buffered saline; rOPN, recombinant mouse osteopontin; PAB, pulmonary artery banding; RV, right ventricle; CSA, cross sectional area; WT, wild type mice; OPN KO, osteopontin knockout mice. Differences were assessed by two-way ANOVA and Sidak's multiple comparison test; ****P < 0.0001.

Cardiac output (CO) and cardiac index (CI) derived from CO correction to both BW and BSA significantly decreased in mice from all PAB-groups, which were not influenced by genetic background and osteopontin treatment (**Figure 25**). Similarly, both TAPSE (**Figure 21, C**) and RV S´ (**Figure 21, D**) were significantly decreased in mice from all PAB groups regardless of genetic background and osteopontin treatment (**Figure 26**).

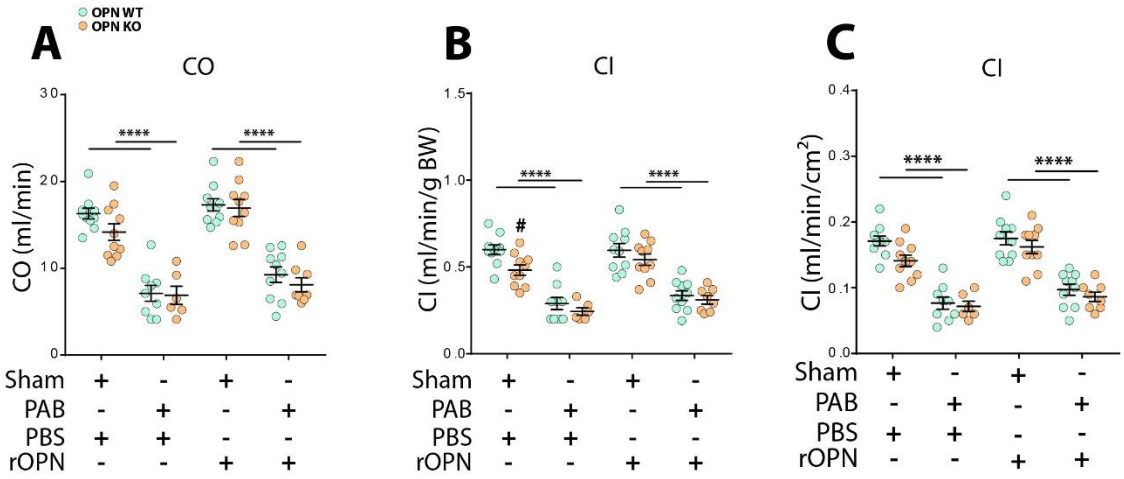

Figure 25. Cardiac output and cardiac index measured from aortic flow.

A) Cardiac output (CO, ml/min). B) Cardiac index (CI, ml/min/g BW), CO corrected to body weight (BW). C) Cardiac index ((CI, ml/min/cm²), CO corrected to body surface area (BSA); Sham, Sham surgery; PAB, Pulmonary artery banding surgery; PBS, phosphate-buffered saline; rOPN, recombinant mouse osteopontin; WT, wild type mice; OPN KO, osteopontin knockout mice. Data are given as scatter dot plots, and lines are means and standard errors of the mean. Differences were assessed by two-way ANOVA and Sidak's multiple comparison test; ****P < 0.0001.

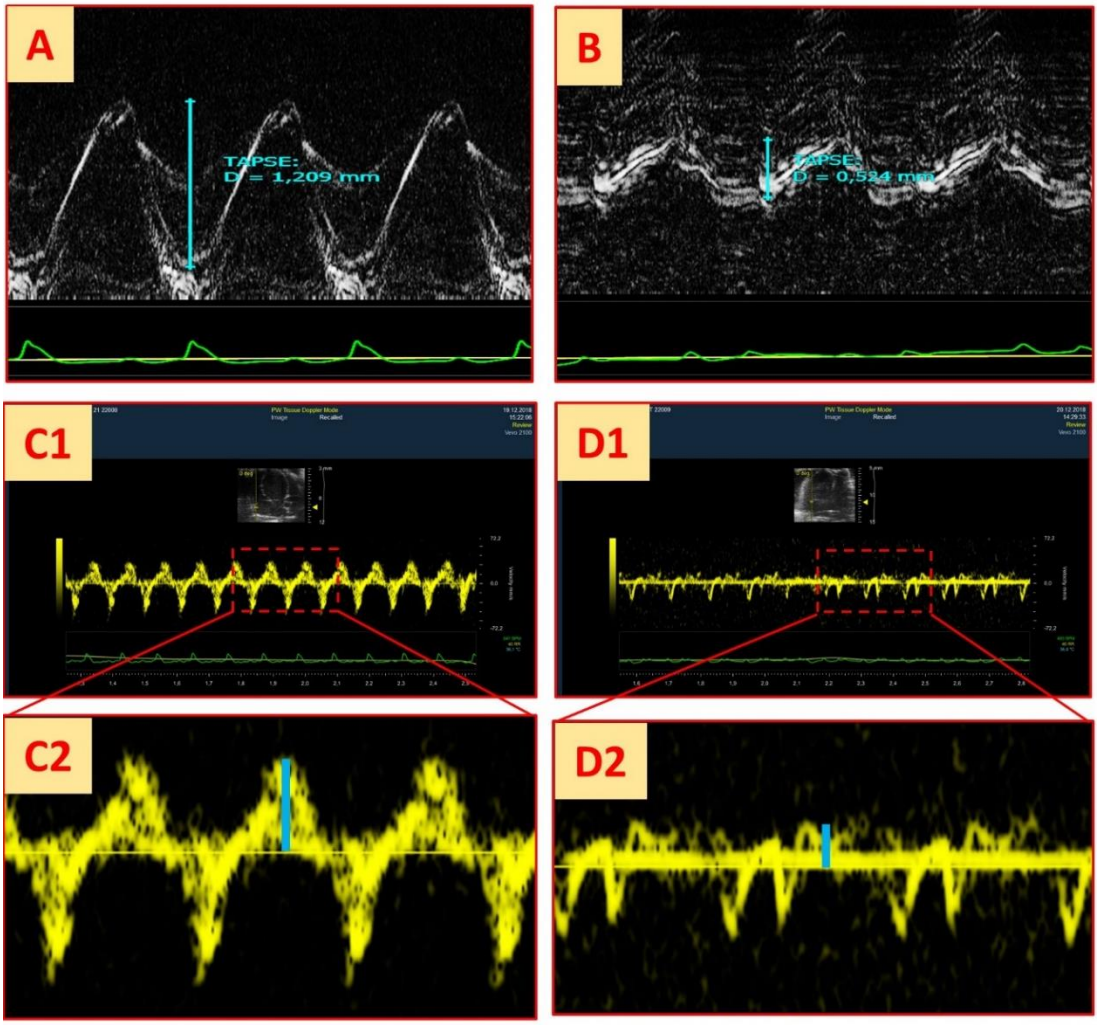

Figure 26. Measurements of tricuspid annular plane systolic excursion (TAPSE) and tricuspid annulus systolic velocity (RV S`).

A) TAPSE in a sham-operated mouse after 21 days, B) TAPSE in a PAB-operated mouse after 21 days, C1) RV S´ in a sham-operated mouse after 21 days; C2) zoomed picture of RV S´ from C1, D1) RV S´ in a PAB-operated mouse after 21 days; D2) zoomed picture of RV S´ from D1.

8 DISCUSSION

In this study, we aimed to elucidate the role of osteopontin in pressure overload-induced RV remodeling and dysfunction in mouse PAB model. To address our research questions, we employed both osteopontin loss-of-function approach using OPN KO mice as well as osteopontin gain-of-function approach using chronic administration of recombinant osteopontin to WT mice. In addition, we reconstituted osteopontin in OPN KO mice with chronic treatment of rOPN.

RV performance determines prognosis in patients with various cardiovascular and respiratory diseases. Despite its implied importance, the mechanisms underlying RV pathology remain unknown. Accordingly, deeper insights into the mechanisms underlying the RV remodeling in response to pressure overload may provide with important clues on potential therapeutic targets which would help to develop novel therapeutic strategies directed specifically at the RV and improve survival of patients suffering from RV failure.

Endothelin receptor antagonists (ERAs), phosphodiesterase type 5 (PDE5) inhibitors, prostanoids, and soluble guanylyl cyclase (sGC) activator are currently approved treatment strategies for PAH [138]. Despite the application of these therapeutic strategies the morbidity and mortality of PAH patients remain high. Although, the development of these strategies was based on the identification of key molecular events driving PA remodeling, application of them exert limited benefit to improve PA remodeling/constriction and RV adaptation to pressure overload, thus, resulting in lack of curative effects in PAH patients. These facts suggest that the pathobiology of PA remodeling and RV failure are complex and exact mechanisms remain to be identified. Thus, it is critical to understand the mechanisms underlying RV remodeling in order to develop novel and more effective PAH specific therapeutic strategies directed not only at the pulmonary vasculature but also the RV.

Studying the role of a gene in physiology and pathology by employing gain-of-function (gene overexpression) or loss-of-function (gene knockout) mice provides us with the excellent tool to gain insights into the specific roles and functions of the gene by the resulting phenotypes manifested spontaneously or upon exposure to some insults. Osteopontin expression in adult healthy myocardium is very low or undetectable [73-77]. Embryogenesis is associated with the augmented expression of osteopontin in

various organs including the heart [75, 78, 79]. Despite its importance during embryogenesis, OPN KO mice do not display any major abnormalities [49, 80], which enabled scientist to exploit those mice in a number of disease models. Similarly, OPN KO mice also have been used in various cardiovascular disease models including various LV disease models (**Table 1)**.

However, there are no studies specifically addressing the role/function of osteopontin in RV physiology and remodeling. Although, few studies have demonstrated that osteopontin is upregulated in the remodeled RV myocardium in various models of PAH including MCT rats [139, 140], PAB rats [141], SuHx rats [141] and HOX rat [142].Thus, to follow this research line, we undertook the current study.

8.1 Osteopontin as a biomarker of RV remodeling and dysfunction

Circulating osteopontin has been established as a valuable biomarker of adverse outcome in patients with various forms of heart failure [143-145]. Similarly, circulating levels of osteopontin in PH patients also have been shown to be elevated in several studies and in these studies osteopontin levels have been shown to correlate with hemodynamic parameters such as pulmonary artery dispensability index [146], the right atrial (RA) pressure [147] as well as functional parameters, including six minute walking distance (6MWD) [146, 147] and New York Heart Association (NYHA) Functional Classification (NYHA FC) [147, 148]. Moreover, baseline osteopontin levels have been demonstrated to be predictive of survival in patients with PAH [147-149]. In addition, circulating osteopontin levels have been found to predict adverse RV remodeling in patients with PAH [146, 150]. However, the origin of the elevated circulating osteopontin levels observed in PAH patients remain unknown since theoretically osteopontin can originate from both remodeled RV myocardium and pulmonary vasculature (**Table 5**).

The source of circulating osteopontin in patients with various heart diseases is usually the remodeled myocardium and its levels may reflect the pathological processes happening to the myocardium. In line with this concept, there have been several attempts to investigate the potential of osteopontin as a biomarker of RV dysfunction.

Table 5. Selected studies evaluating circulating levels of osteopontin in patients with various forms of pulmonary hypertension

Diagnosis	Subjects	Findings	Authors
PH with various etiologies	PH (n=71), Control (n=40)	Patients with severe functional class have higher levels of OPN compared to those with less severe functional class (NYHA I-II vs NYHA III-IV). OPN is a strong independent predictor of all-cause mortality within 24 months	Rosenberg et al., 2012 [148]
PH with various etiologies	PH (n=71)	OPN plasma values significantly correlated with RVEDD, TAPSE and RVS. Patients with RV dysfunction and remodeling higher levels of OPN compared to those with lower levels of OPN (956 ng/mL vs. 628 ng/mL). ROC analysis revealed that an OPN threshold of 694.2 ng⁄mL detects RV enlargement.	Rosenberg et al., 2012 [150]
IPAH	IPAH (n=95) (retrospective cohort (n=70) and prospective cohort (n=25), Control (n=40)	In both retrospective and prospective cohort, OPN levels correlated with PAP and NT-BNP. In the retrospective cohort, OPN levels also correlated with age, 6MWD, and NYHA class. Multivariate Cox analysis demonstrated that baseline OPN levels were independent predictors of mortality. Being normal or elevated at baseline (below or above 34.5 ng/mL), proportional survival rates were 100% vs 80% after 1 year and 77% vs 51% after 3 years, respectively.	Lorenzen et al., 2011 [147]
PH with various etiologies	PH (n=62), Control (n=12)	Plasma OPN levels in patients with PH were elevated in comparison with healthy control subjects. Plasma OPN levels predicted decreased 6MWD. OPN levels were associated with NT-proBNP, RVEDD (echo), and RVD (MRI) and PA distensibility index.	Kazimli et al., 2013 [146]
IPAH	IPAH (n=35)	OPN correlated with WHO functional class and 6MWD. A cut-off of OPN (53.4 ng/mL) predicted significant differences in survival in patients with IPAH at 4.0±2.2-year follow-up.	Rhodes et al., 2010 [149]
CAD-COPD patients with and without PH	CAD-COPD (n=131)	OPN levels correlated with mPAP and 6MWD. OPN levels >43 ng/mL remained statistically significant predictor of PH in patients with CAD-COPD.	Hetman et al., 2016 [151]
DCM with and without RV dysfunction	DCM (n=70) (DCM without RVD (n=15) and with RVD (n=55))	OPN levels in DCM patients correlated with RVD1, RVD2 and PAPs.	Rubis at al., 2017 [152]

Abbreviations: PH, Pulmonary hypertension; IPAH, Idiopathic pulmonary arterial hypertension; RV, Right ventricle; OPN, Osteopontin; NYHA, New York Heart Association Functional Classification; WHO, World health organization; RVEDD, Right ventricular end-diastolic diameter; TAPSE, Tricuspid annulus plane systolic excursion; RV S´, Tricuspid annulus systolic velocity; NT-proBNP, N-terminal pro b-type natriuretic peptide; 6MWD, six minute walking distance; PAP, Pulmonary artery pressure; RVD, Right ventricular dysfunction; PA, Pulmonary artery; CAD, Coronary artery disease; DCM, Dilated cardiomyopathy.

For examples, osteopontin levels in patients with DCM have been shown to correlate with pulmonary hemodynamics and RV remodeling parameters [152] suggesting the importance of osteopontin in DCM and its effect on the RV function. In addition, two preclinical studies have shown that the remodeled RV myocardium serves as a source

of circulating osteopontin in MCT [139] and HOX rats [142] based on the findings showing close dynamics of plasma osteopontin content with its expression levels in the remodeled RV myocardium. In this line, we also measured circulating levels of osteopontin in various models of PAH including HOX mice and rats, SuHx rats and MCT rats. In contrast to previous studies, MCT PAH rats displayed decreased levels of circulating osteopontin compared to controls; while, in other models osteopontin levels did not change. In order to test if pressure overloaded RV may lead to the increased circulating osteopontin levels, we determined plasma osteopontin in PAB mice over the course of 3-week experiment. The results showed that plasma osteopontin is increased at all measured time-points, reaching maximum on day 14 after PAB surgery. In summary, further preclinical and clinical studies are required to establish osteopontin as a biomarker of RV remodeling and dysfunction.

8.2 Osteopontin in pressure overloaded RV

Established systemic hypertension or aortic stenosis in humans or TAC-surgery in mice and rats cause pressure overload-induced LV remodeling. In these disease and disease models, myocardial osteopontin is upregulated which is associated with adverse changes in ECM homeostasis along with functional alterations of cardiomyocytes and fibroblasts [49, 75, 80-82, 153-155]. However, it remains incompletely understood if osteopontin upregulation is adaptive response aimed to prime myocardial tissue to cope better with the increased pressure overload or an active player driving adverse myocardial remodeling.

Evaluating the myocardial expression profiling of osteopontin over the course of the disease development in parallel with the cardiac function assessment may provide some clue whether its expression dynamics proceed or follow heart failure development or does not changes. However, available studies report controversial results in expression dynamics of osteopontin during the course of the pressure overload-induced LV failure and in its impact on heart faire progression; time-dependent upregulation of osteopontin reaching maximum expression levels at 1 month after TAC-surgery in mice [154] or rapid and dramatic increase of osteopontin within 24h after TAC-surgery with further decreasing to 7 days but still remaining elevated [155], or significant increase after 3 day of TAC-surgery with further decreasing to 7th day [119]. Despite of the same model used in these studies, the

discrepancy may indicate differences in the degree of the pressure overload or differences in mouse strains and further studies are still required if the changes of osteopontin expression over the course of the disease has some impact on heart failure development and progression. Nevertheless, robust myocardial collagen accumulation and progression of myocardial stiffness in injured myocardium coincides with the increase of osteopontin expression [97] suggesting that osteopontin may be implicated in the transition to adverse myocardial fibrosis.

However, osteopontin may also lack crucial roles in heart failure development and its expression displayed in different cardiac diseases or disease models may be a simple indicator/marker of the cardiac hypertrophy and remodeling like A-type natriuretic peptide (ANP) and B-type natriuretic peptide (BNP). As, it has been shown that there is a strong correlation between expression levels of osteopontin and ANP in the LV myocardium in both renovascular and TAC-induced LV remodeling models [75]. In addition, osteopontin expression in LV myocardium has been shown to be dependent on systemic blood pressure values in L-NAME-induced model of hypertension in rats [156]. These studies indicate that osteopontin can be used a marker of myocardial stress and hypertrophy.

Currently available preclinical studies on the role of osteopontin in pressure overloaded LV remodeling have shown that mice deficient for osteopontin display more severe LV remodeling and systolic dysfunction compared to WT mice in various pressure overload-induced LV remodeling models, including in aldosterone treated [81] and angiotensin II treated mice [49, 80, 87] mainly due to attenuated myocardial fibrosis. In contrary to these studies, OPN KO mice subjected to TAC surgery developed more severe myocardial fibrosis along with deteriorated LV dysfunction [157]. Although, there is a study stating that OPN KO mice subjected to TAC-surgery display similar degree of myocardial fibrosis as wild type counterparts [82]. Nevertheless, targeting osteopontin with specific aptamer have been found to be beneficial in treating TAC-induced LV remodeling and dysfunction [157]. Thus, complete loss of osteopontin in LV pressure overloaded mice leads to more severe cardiac dysfunction due to attenuated or exaggerated myocardial fibrosis; although, blocking osteopontin with pharmacological agents (aptamers), which does not eliminate osteopontin completely, seems to be beneficial.

However, the mechanisms underlying attenuated myocardial fibrosis in OPN KO mice in heart disease models remain elusive. And, it may be related to the cardiac fibroblast

properties but not necessarily to the ECM synthesis. For example, cardiac fibroblasts isolated from OPN KO mice, maintained their ability to produce components of ECM, despite attenuated myocardial fibrosis in Ang-II induced model of LV failure, which may be related to the decreased fibroblast proliferative and adhesive functions [80]. In addition, myocardium of OPN KO mice display disarrayed collagen deposition, implying an essential role of osteopontin in ECM assembly and organization. Therefore, elevated osteopontin levels in the myocardium in response to pressure overload likely to exert beneficial effects by contributing to the formation of tissue-stabilizing fibrosis, in order to enable cardiomyocytes to perform their contractile functions properly against increased wall stress, as demonstrated by deterioration of cardiac functions in OPN KO mice compared to WT littermates in different pressure overload-induced LV remodeling models due to decreased myocardial fibrosis [80, 106].

Deposition of insoluble collagen contributes to the increased EMC accumulation and myocardial stiffness. Osteopontin has been shown to increase lysyl oxidase expression and activity, an enzyme responsible for the formation of cross-linked insoluble collagen [89, 155]. In TAC-induced model of LV failure, osteopontin expression was positively correlated with LOX expression in the myocardium [155]. Similarly, pharmacological inhibition of osteopontin with ALK5 inhibitor SM16 in TAC mice attenuates myocardial fibrosis, resulting in LV dilatation, systolic dysfunction and increased mortality [158]. These findings highlight the potential role of osteopontin in stabilizing ECM by modulating lysyl oxidase activity, absence of which might be the cause ECM to fail to be stabilized and contribute to the rupture of aortic wall in that mice. Although, the exact mechanisms of how osteopontin activates lysyl oxidase remain elusive, the current knowledge suggests that osteopontin may directly activate lysyl oxidase in the extracellular space to facilitate excessive incorporation of collagen into ECM by cross-linking formation [89]. In fact, enzymes involved in collagen synthesis is not upregulated in the remodeled myocardium, despite the increased deposition of collagen fibrils indicating the importance of collagen stabilizing factors in accumulation of ECM in fibrotic tissue. Similarly, lysyl oxidase also lacks the ability to induce collagen synthesis, which exclusively serves as collagen-stabilizer by forming cross-links between collagen fibers [89]. In support to this notion, Fan et al., show that TIMP KO mice, subjected to Ang-II infusion displayed increased myocardial fibrosis along with significantly upregulated osteopontin expression, despite the lack of

collagen expression, indicating the importance of posttranslational processing and deposition of collagen fibers in tissue fibrosis [153]. Taken together, osteopontin is an important mediator of procollagen processing and deposition and that osteopontin may act primarily in the extracellular space to increase tissue stiffness. Although exact signaling pathways leading to lysyl oxidase activity by osteopontin remain to be elucidated.

The main effector cell type driving tissue fibrosis is myofibroblast, which is derived from resident fibroblast present within tissue that respond to various pro-inflammatory and pro-fibrotic signals [159]. Transforming growth factor-β (TGF-β) is a multifunctional cytokine mediating myofibroblast transformation and collagen synthesis. TGF-β1 fails to induce myofibroblast differentiation of osteopontin-depleted fibroblasts, as shown by the absence of alpha-actin, ED-A and CTGF expression, indicating pivotal role of osteopontin in myofibroblast differentiation. Interestingly, osteopontin operates along with HMGB1 intracellularly to form focal adhesions in the myofibroblasts in response to TGF-β1 stimulation [160]. Thus, osteopontin is an active player driving myofibroblast differentiation in heart diseases.

Various afterload-dependent small animal models of RV remodeling including hypoxia exposure (HOX), combined use of the vascular endothelial growth factor receptor 2 (VEGFR2) inhibitor SU5416 and exposure to hypoxia (SuHx), and monocrotaline (MCT) treatment are widely used in the community to study the mechanisms underlying RV remodeling and dysfunction as well as to test the effects of potential RV directed therapeutics [161]. Although, among these models, SuHx rats develop severe PAH which closely mimics the pulmonary vasculopathy observed in patients with PAH [162] including concentric- and plexiform-like lesions. Importantly, in this model, rats develop severe maladaptive RV remodeling [38] which makes it more suitable model to study pressure overload-induced RV remodeling compared to others. However, in these afterload-dependent models, the changes in the RV structure and function might be just reflection of the changes in the pulmonary hemodynamics/vasculature. Therefore, it is essential to use PAB model, which is an afterload-independent model of RV remodeling. Employing PAB model of RV remodeling enables scientists to study the role of target genes in RV remodeling as well as to test direct, afterload-independent effects of potential therapeutics on the intrinsic properties of the pressure overloaded RV [161, 163].

The concept that osteopontin may be detrimental to the RV is partly driven from the studies stating that using of various pharmacological agents improving pulmonary hemodynamics and right ventricular function also decrease osteopontin expression such as PPAR-γ activator pioglitazone [126] and estrogen receptor-β agonist 17β-estradiol [139]. Although, in these studies, decreased osteopontin expression may be just the reflection of the decreased afterload which eventually relieves the RV from the wall stress, but not due to direct effects of those agents on the RV. However, the latter cannot be excluded and needs to be proven in studies employing PAB model.

In our study, all PAB mice developed severe RV remodeling and dysfunction after 3 weeks and there were no significant influences of osteopontin deficiency and osteopontin administration/reconstitution on the RV structure and function. Although, OPN KO mice showed a trend towards more dilated, hypertrophied and dysfunctional RV compared to WT mice after pressure overload induction, there were no significant differences. In order to phenotype the RV, we have employed 2D echocardiography which has been very well established as a tool to phenotype cardiac pathologies [164]; although, having same limitation in detecting subtle changes in the RV function compared to magnetic resonance imaging (MRI) study, which is a gold standard method in imaging RV structure and function, which is superior to conventional echocardiography. Thus, employing MRI imaging in such kind of studies may be beneficial to better phenotype the RV pathologies.

However, PBS treated OPN KO mice subjected to PAB surgery displayed significantly increased mortality compared to the corresponding WT littermates. The survival of those mice became better with the administration of recombinant osteopontin (osteopontin reconstitution). These results clearly suggest that presence of osteopontin is crucial to prolong the survival of mice with RV failure condition and treatment with recombinant osteopontin might be novel therapeutic strategy in RV failure.

Although, it has been very well demonstrated that osteopontin drives pulmonary artery remodeling in PAH models and strategies aiming to block osteopontin effects on pulmonary arteries have been shown to exert benefits to the PA remodeling [165-167]. In contrast to pulmonary artery remodeling, our study demonstrates that osteopontin might play beneficial for the RV to cope better with pressure overload. Thus, osteopontin might have tissue/compartment specific roles, which must be considered in interfering osteopontin signaling.

As already discussed above, insights from pressure overloaded LV failure studies revealed that osteopontin deficiency may lead to the adverse cardiac remodeling and dysfunction despite of attenuated myocardial fibrosis. In our study, both OPN KO and WT mice displayed similar degree of RV remodeling and dysfunction upon exposure to fixed-pressure overload, which might be explained that in our study, titanium ligating clip was compressed severely compared to previously published studies as shown by the degree of RVSP increase. And, this concept was tested recently in rat PAB model of RV remodeling, which showed that severe compression of the ligating clip causes severe RV failure associated with increased mortality compared to mild or moderate clip compressions [163]. Moreover, in contrary to LV failure models, in our study, we observed PAB - surgery caused similar degree of myocardial fibrosis and cardiomyocyte hypertrophy in OPN KO mice compared to WT controls. Although, the contribution and role of myocardial fibrosis in RV remodeling and dysfunction have not been established yet [27, 168] and recent studies demonstrate that pharmacological inhibition of myocardial fibrosis does not necessarily improve RV function [169] and transgenic mice displaying increased myocardial fibrosis upon pressure overload display maintained RV function [45] in PAB models.

In addition, in our study, we did not monitor cardiac function echocardiographically over the course of the disease development and OPN KO mice displaying higher mortality might also exhibit earlier development of RV remodeling and dysfunction compared to WT littermates, which will be addressed in the future studies. As, we and others have shown that RV remodeling develops gradually after induction of fixed RV pressure overload [136, 170].

8.3 Osteopontin signaling pathways in heart failure

As discussed in previous sections, osteopontin carry divergent functions in cardiac physiology and diseases. However, the signaling pathways by which osteopontin participates in those processes remain incompletely understood. And the currently available knowledge states that osteopontin binding to its receptors, initiates various signaling pathways involved in diverse processes in the myocardium including myocardial fibrosis, inflammation, angiogenesis, cardiomyocyte hypertrophy and apoptosis.

Osteopontin induced signaling pathways are mostly studied in cardiac fibroblasts and less frequently in cardiomyocytes and myocardial resident macrophages.

In cardiac fibroblasts, Ang-II induced osteopontin upregulation in those cells causes cell proliferation and contraction mediated by osteopontin RGD domain - β3-integrin receptor signaling axis [171]. Cardiac fibroblasts isolated from OPN KO mice display decreased proliferation and adhesion to ECM [172, 173]. IL-1β-induced expression and activation of MMP2 and MMP9 in cardiac fibroblasts are mediated through osteopontin – β3-integrin - PKC-ζ signaling pathway axis [174]. Mouse cardiac fibroblasts deficient for osteopontin exhibit caspase-3-independent cell death in response to hydrogen peroxide challenge [175] indicating the protective role of osteopontin against ROS exposure. Osteopontin - CTGF axis increases lysyl oxidase expression and activity in fibroblasts [176].

In cardiac macrophages, upon myocardial infarction (MI), activation of IL-10 - STAT3 - galectin-3 axis in CD206+ macrophages leads to osteopontin upregulation which promotes cardiac reparative processes in early stages of MI which prevents adverse myocardial remodeling [177]. In cardiomyocytes, osteopontin binding to CD44 receptor causes cell apoptosis due to activation of mitochondrial apoptotic death pathway (BAX and cytochrome c) and an increase of endoplasmic reticulum (ER) stress pathway (Gadd153 and caspase-12) [101].

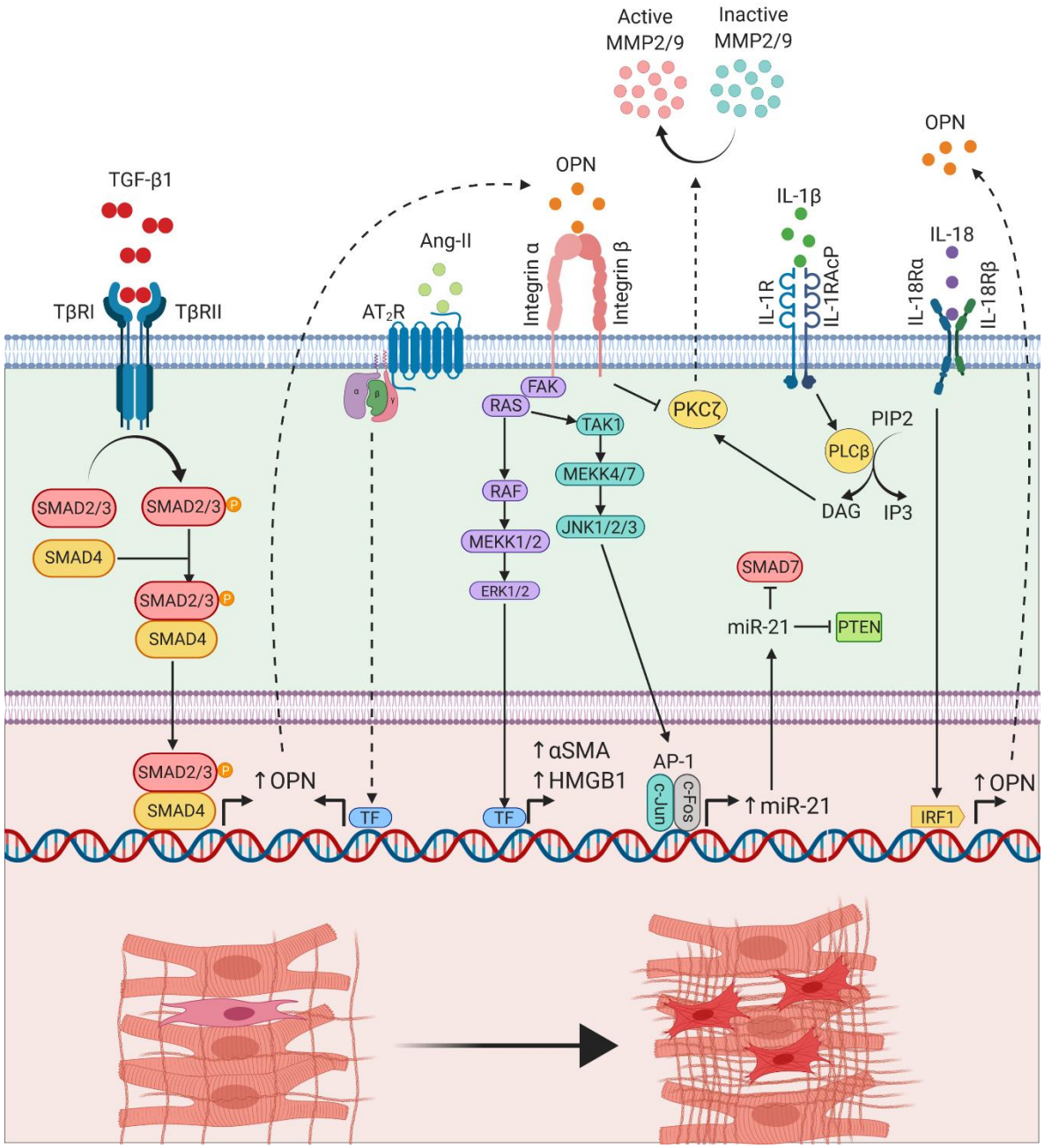

Figure 27. Overview of osteopontin upstream and downstream signaling pathways in cardiac fibroblasts.

Transforming growth factor beta one (TGF-β1) as a dimer binds to heterotetrametric receptor complex consisting two TGF-βRII and two TGF-βRI. Activated TGF-βRII - TGF-βRI receptor complex further phosphorylates SMAD2/3, which recruits SMAD4 forming SMAD2/3-SMAD4 complex leading to osteopontin transcription in the nucleus. Angiotensin II (Ang-II) binds to type 2 angiotensin receptor (AT_2R), which activates various signaling pathways to increase osteopontin transcription. Osteopontin binding to integrin receptors activates various MAPK signaling pathways leading to the myofibroblast differentiation and synthesis of extracellular matrix (ECM). Osteopontin also inhibits IL-1β-induced protein kinase Cζ (PKCζ) activation leading to MMP-2 and MMP-9 activation. IL-18 activates IRF1 transcription factor leading to osteopontin transcription. The overall consequences of the depicted signaling events are fibroblast to myofibroblast transdifferentiation and extracellular matrix synthesis. Figure was created using BioRender.com

However, all these studies have investigated osteopontin signaling pathways in the context of LV remodeling and dysfunction. Although, at cellular levels, the signaling might be the same, it must be investigated in the context of RV remodeling considering all structural and functional properties of the RV and its cell types. In the current study, we have not studied signaling pathways related to the osteopontin, which we plan to address in the future studies.

8.4 Future experimental and clinical protectives

Taken together, lack of osteopontin worsens the survival of mice with pressure overloaded RV failure despite of similar echocardiographic structural and functional changes in the RV as compared to the WT littermates. However, the results of the current study are not conclusive and further experiments are required to establish the exact structural and functional phenotypes of the RV in those mice with more frequent monitoring (every week echocardiography) of the RV structure and function over the course of disease development. Although echocardiography is widely available imaging modality, it has limited capabilities for the assessment of the RV due to its complex morphology as mentioned in previous sections [178]. Magnetic resonance imaging (MRI) has been established as the referenced standard imaging modality for the cardiac imaging based on its unique capability in providing an accurate and reproducible evaluation of the morphology, structure and function of the heart [179, 180]. Thus, using MRI would help us to better phenotyping the RV and using unbiased omics approaches including transcriptomics, proteomics, and metabolomics of both RV tissues and plasma samples would help us to identify signaling pathways determining molecular mechanisms of RV remodeling due to osteopontin deficiency.

Although, available studies show that osteopontin may activate various signaling pathways with diverse cellular effects depending on cell type and specific cardiac disease. Further studies are required to establish receptor binding domain -, receptor –, and cell type- specific activated signaling pathways of osteopontin in cardiac physiology and diseases including the RV

We strongly believe that further studies in this research line will provide with the mechanistic insights into how the RV remodels in response to pressure overload or even to interfere myocardial remodeling processes in the RV in order to increase RV adaptation

9 CONCLUSIONS

As osteopontin plays diverse roles in various biological as well as pathological processes and may have both beneficial and adverse effects on the RV remodeling and exploiting global OPN KO mice is rather a nonspecific approach to delineate its role in RV remodeling. Identifying myocardial cell type specific roles of osteopontin involved in either adaptive or maladaptive RV remodeling and selective inhibition or overexpression may represent a more specific approach to delineate the specific roles of osteopontin in RV remodeling.

In the current study, we have demonstrated that PAB surgery causes similar degree of RV remodeling and dysfunction in OPN KO mice as compared to WT mice; although, osteopontin deficiency leads to increased mortality of mice with RV failure and its recontribution improves the survival of those mice.

Based on the preliminary results of our study and data from the literature we believe that osteopontin may play beneficial role in RV remodeling at least in part due to improved survival.

Despite many studies have been performed to elucidate osteopontin biology in various organs and disease conditions, there are many aspects to establish including cell, time specific roles, as well as specific downstream and upstream signaling pathways in the setting of RV remodeling. Considering that osteopontin may exert both beneficial and detrimental effects on RV remodeling, and new therapeutic modalities and strategies need to be developed in order to keep beneficial effects while avoiding or preventing its detrimental effects.

Thus, it is of interest to utilize either myocardial cell type specific (cardiomyocyte or cardiac fibroblast) or hematopoietic cell specific OPN KO mice as well as application of pharmacological agents either inhibiting or inducing endogenous osteopontin expression to establish the exact role of osteopontin in RV remodeling.

Taken together, this study suggests that osteopontin may represent a novel player in RV remodeling and may serve a new therapeutic approach/target for the treatment of RV failure.

10 SUMMARY

Right ventricular (RV) remodeling and dysfunction determine the survival and outcome of patients with various cardiopulmonary diseases. Adaptive RV remodeling developed initially upon induction of pressure overload may eventually lead to the maladaptive RV remodeling (right heart failure). Despite the clinical importance of RV remodeling in response to pressure overload, the mechanisms of disease development remain unidentified. Moreover, there are no specific RV directed pharmacological agents improving RV function in diseases causing its dysfunction.

In several animal models of PH, osteopontin expression is increased in the RV myocardium. In addition, circulating osteopontin levels are elevated in PH patients with various etiologies and correlate with RV dysfunction in those patients. We therefor hypothesized that subjecting OPN KO mice (loss-of-function approach) to the pressure overload would provide us with insights into the role of osteopontin in RV remodeling. Furthermore, we studied the effects of osteopontin reconstitution on RV remodeling with chronic administration of recombinant osteopontin (rOPN) in either OPN KO or WT mice (gain-of-function approach) subjected to pressure overload. To induce pressure overload, we performed sham or pulmonary artery banding (PAB) surgery in OPN KO and WT mice and treated them with rOPN for 3 weeks.

We successfully demonstrated that PAB surgery caused severe increase in RV systolic pressure and RV remodeling and dysfunction in both OPN KO and WT mice as shown by echocardiographic and invasive hemodynamic measurements. rOPN treatment had no effects on the parameters of RV structure and function in both OPN KO and WT mice. Despite of similar degree of RV remodeling, PAB-operated OPN KO mice displayed increased mortality, however, treatment with rOPN improved survival of those mice.

In conclusion, lack of osteopontin led to the increased mortality of mice with RV failure indicating the crucial role of osteopontin for the survival in right heart failure condition. In addition, improved survival of OPN KO mice with rOPN treatment suggests the therapeutic potential of osteopontin for the treatment of RV failure to improve survival.

11 ZUSAMMENFASSUNG

Die strukturellen Gewebeveränderungen und eine daraus resultierende Fehlfunktion des rechten Ventrikels (RV) bestimmen letztendlich den Therapieerfolg und damit das Überleben vieler kardio-pulmonaler Erkrankungen. Adaptive zelluläre Prozesse im rechten Ventrikel mit dem Ziel der Anpassung an steigende Blutdrücke können zu einem späteren Zeitpunkt zu einem maladaptiven Zustand führen, der zum Rechtsherzversagen beiträgt. Trotz der immensen klinischen Relevanz dieser pathologischen Veränderungen sind die ursächlichen Mechanismen noch unklar. Darüber hinaus gibt es derzeit keine spezifischen pharmakologischen Wirkstoffe, die den kausalen Prozess der Fehlfunktion des rechten Ventrikels aufhalten und/oder die Funktion des rechten Ventrikels verbessern.

In verschiedenen Tiermodellen der pulmonalen Hypertonie (PH) konnte eine verstärkte Expression von Osteopontin im Myocardium des rechten Herzventrikels beobachtet warden. Zusätzlich sind auch die Spiegel an zirkulierendem Osteopontin in PH-Patienten unterschiedlichster Etiologien erhöht. Es existiert hier eine direkte Korrelation zwischen dem Osteopontin-Level und der Fehlfunktion des RV. Aus diesem Grund wurde im Rahmen der vorliegenden Arbeit der Einfluss einer gesteigerten Nachlast in Osteopontin-defizienten Mäusen untersucht (loss-of-function). Dies sollte Aufschluss über die Rolle von Osteopontin in der Gewebeveränderung des rechten Ventrikels geben. Desweiteren wurden die Effekte einer Rekonstitution von Osteopontin auf die pathologischen RV-Gewebeveränderungen analysiert. Dies wurde durch eine dauerhafte Verabreichung des rekombinanten Osteopontin-Protein (rOPN) in Osteopontin-defiziente (OPN-KO) sowie Wildtyp-Mäuse (WT) in Kombination mit einer erhöhten Nachlast ermöglicht (gain-of-function).

Als Modell für eine erhöhte Nachlast des rechten Herzventrikels wurde die Ligatur der Pulmonalarterie (engl. PAB: pulmonary artery banding) gewählt. Die Versuchsdauer nach dieser operativen Verengung der Pulmonalarterie und der anschließenden Verabreichung von rOPN betrug 3 Wochen.

Mittels Echokardiographie und hämodynamischen Messungen konnten wir einen schwerwiegenden Anstieg des rechtsventrikulären, systolischen Blutdrucks bei den PAB-operierten OPN-KO und WT-Mäusen beobachten. Im Einklang damit war die

Struktur des RV-Gewebes deutlich pathologisch verändert und es lag eine Fehlfunktion des RV vor. Rekombinantes OPN hatte keinen Effekt auf die Parameter der Gewebeschädigung und die Funktion des rechten Ventrikels unabhängig vom genetischen Hintergrund der Mäuse. Trotz ähnlich stark ausgeprägten RV-Gewebeveränderungen zeigten die PAB-operierten OPN-KO-Mäuse eine erhöhte Mortalität, die durch eine Behandlung mit rOPN unerklärlicherweise reduziert werden konnte.

Wir schlussfolgern daher, dass ein Verlust der Osteopontin-Expression mit einer erhöhten Sterblichkeit bei Mäusen mit beginnender RV-Fehlfunktion verbunden ist. Dies deutet auf die kritische Rolle von Osteopontin für das Überleben beim Rechtsherzversagen hin. Zusätzlich kann man aus der Tatsache, dass eine rOPN-Gabe das Überleben von OPN-KO Mäusen verlängert, ein mögliches therapeutisches Potential von Osteopontin für die Behandlung von Patienten mit Rechtsherzversagen ableiten.

12 REFERENCES

1. Kandathil, A. and M. Chamarthy, *Pulmonary vascular anatomy & anatomical variants.* Cardiovascular diagnosis and therapy, 2018. **8**(3): p. 201-207.
2. Horsfield, K., *Morphometry of the small pulmonary arteries in man.* Circ Res, 1978. **42**(5): p. 593-7.
3. Huang, W., et al., *Morphometry of the human pulmonary vasculature.* J Appl Physiol (1985), 1996. **81**(5): p. 2123-33.
4. Sheehan, F. and A. Redington, *The right ventricle: anatomy, physiology and clinical imaging.* Heart, 2008. **94**(11): p. 1510-5.
5. Srivastava, D. and E.N. Olson, *A genetic blueprint for cardiac development.* Nature, 2000. **407**(6801): p. 221-6.
6. Hill, J. and E. Olson, *Muscle 2-Volume Set: Fundamental Biology and Mechanisms of Disease*. 2012: Academic Press.
7. Dodou, E., et al., *Mef2c is a direct transcriptional target of ISL1 and GATA factors in the anterior heart field during mouse embryonic development.* Development, 2004. **131**(16): p. 3931-42.
8. Ho, S. and P. Nihoyannopoulos, *Anatomy, echocardiography, and normal right ventricular dimensions.* Heart, 2006. **92**(suppl 1): p. i2-i13.
9. Haddad, F., et al., *Right ventricular function in cardiovascular disease, part I: anatomy, physiology, aging, and functional assessment of the right ventricle.* Circulation, 2008. **117**(11): p. 1436-1448.
10. Zong, P., J.D. Tune, and H.F. Downey, *Mechanisms of oxygen demand/supply balance in the right ventricle.* Experimental biology and medicine, 2005. **230**(8): p. 507-519.
11. Chin, K.M., N.H. Kim, and L.J. Rubin, *The right ventricle in pulmonary hypertension.* Coronary artery disease, 2005. **16**(1): p. 13-18.
12. Chin, K.M., N.H. Kim, and L.J. Rubin, *The right ventricle in pulmonary hypertension.* Coron Artery Dis, 2005. **16**(1): p. 13-8.
13. Humbert, M., et al., *Pathology and pathobiology of pulmonary hypertension: state of the art and research perspectives.* Eur Respir J, 2019. **53**(1).
14. Hoeper, M.M., et al., *Definitions and diagnosis of pulmonary hypertension.* Journal of the American College of Cardiology, 2013. **62**(25 Supplement): p. D42-D50.
15. Morrell, N.W., et al., *Genetics and genomics of pulmonary arterial hypertension.* European Respiratory Journal, 2019. **53**(1): p. 1801899.
16. Frump, A.L. and T. Lahm, *The Basic Science of Metabolism in Pulmonary Arterial Hypertension.* Advances in Pulmonary Hypertension, 2018. **17**(3): p. 95-102.
17. Rhodes, C.J., J. Wharton, and M.R. Wilkins, *Metabolomic Insights in Pulmonary Arterial Hypertension.* Advances in Pulmonary Hypertension, 2018. **17**(3): p. 103-109.
18. Kim, J., *Apelin-APJ signaling: a potential therapeutic target for pulmonary arterial hypertension.* Molecules and cells, 2014. **37**(3): p. 196.
19. Kuhr, F.K., et al., *New mechanisms of pulmonary arterial hypertension: role of Ca2+ signaling.* American Journal of Physiology-Heart and Circulatory Physiology, 2012. **302**(8): p. H1546-H1562.
20. Ranchoux, B., et al., *DNA damage and pulmonary hypertension.* International journal of molecular sciences, 2016. **17**(6): p. 990.
21. Archer, S.L., et al., *Mitochondrial metabolism, redox signaling, and fusion: a mitochondria-ROS-HIF-1α-Kv1. 5 O2-sensing pathway at the intersection of pulmonary hypertension and cancer.* American Journal of Physiology-Heart and Circulatory Physiology, 2008. **294**(2): p. H570-H578.

22. Meloche, J., et al., *miRNAs in PAH: biomarker, therapeutic target or both?* Drug discovery today, 2014. **19**(8): p. 1264-1269.
23. Cuttica, M.J., *Pulmonary hypertension associated with lung diseases and hypoxemia.* Heart failure reviews, 2016. **21**(3): p. 299-308.
24. Caminati, A., R. Cassandro, and S. Harari, *Pulmonary hypertension in chronic interstitial lung diseases.* European Respiratory Review, 2013. **22**(129): p. 292-301.
25. Guazzi, M. and R. Naeije, *Pulmonary hypertension in heart failure: pathophysiology, pathobiology, and emerging clinical perspectives.* Journal of the American College of Cardiology, 2017. **69**(13): p. 1718-1734.
26. Ayinapudi, K., et al., *Obesity and pulmonary hypertension.* Current hypertension reports, 2018. **20**(12): p. 99.
27. Egemnazarov, B., et al., *Right ventricular fibrosis and dysfunction: Actual concepts and common misconceptions.* Matrix Biol, 2018. **68-69**: p. 507-521.
28. Gorter, T.M., et al., *Right ventricular dysfunction in heart failure with preserved ejection fraction: a systematic review and meta-analysis.* Eur J Heart Fail, 2016. **18**(12): p. 1472-1487.
29. Shah, J.P., et al., *Prevalence and Prognostic Significance of Right Ventricular Dysfunction in Patients With Hypertrophic Cardiomyopathy.* Am J Cardiol, 2018. **122**(11): p. 1932-1938.
30. Gulati, A., et al., *The prevalence and prognostic significance of right ventricular systolic dysfunction in nonischemic dilated cardiomyopathy.* Circulation, 2013. **128**(15): p. 1623-33.
31. Jensen, A.S., et al., *Impaired Right, Left, or Biventricular Function and Resting Oxygen Saturation Are Associated With Mortality in Eisenmenger Syndrome: A Clinical and Cardiovascular Magnetic Resonance Study.* Circ Cardiovasc Imaging, 2015. **8**(12).
32. Nagel, E., M. Stuber, and O.M. Hess, *Importance of the right ventricle in valvular heart disease.* Eur Heart J, 1996. **17**(6): p. 829-36.
33. Tannus-Silva, D.G. and M.F. Rabahi, *State of the Art Review of the Right Ventricle in COPD Patients: It is Time to Look Closer.* Lung, 2017. **195**(1): p. 9-17.
34. Kato, S., et al., *Prognostic value of cardiovascular magnetic resonance derived right ventricular function in patients with interstitial lung disease.* J Cardiovasc Magn Reson, 2015. **17**: p. 10.
35. Maripov, A., et al., *Right Ventricular Remodeling and Dysfunction in Obstructive Sleep Apnea: A Systematic Review of the Literature and Meta-Analysis.* Can Respir J, 2017. **2017**: p. 1587865.
36. Vonk-Noordegraaf, A., et al., *Right heart adaptation to pulmonary arterial hypertension: physiology and pathobiology.* Journal of the American College of Cardiology, 2013. **62**(25 Supplement): p. D22-D33.
37. Sydykov, A., et al., *Inflammatory Mediators Drive Adverse Right Ventricular Remodeling and Dysfunction and Serve as Potential Biomarkers.* Front Physiol, 2018. **9**: p. 609.
38. Frump, A.L., et al., *Emerging role of angiogenesis in adaptive and maladaptive right ventricular remodeling in pulmonary hypertension.* Am J Physiol Lung Cell Mol Physiol, 2018. **314**(3): p. L443-l460.
39. Viswanathan, G., et al., *The Role of G Protein-Coupled Receptors in the Right Ventricle in Pulmonary Hypertension.* Front Cardiovasc Med, 2018. **5**: p. 179.
40. Ryan, J.J. and S.L. Archer, *Emerging concepts in the molecular basis of pulmonary arterial hypertension: part I: metabolic plasticity and mitochondrial dynamics in the pulmonary circulation and right ventricle in pulmonary arterial hypertension.* Circulation, 2015. **131**(19): p. 1691-1702.
41. Piao, L., G. Marsboom, and S.L. Archer, *Mitochondrial metabolic adaptation in right ventricular hypertrophy and failure.* Journal of molecular medicine, 2010. **88**(10): p. 1011-1020.
42. Shults, N.V., et al., *Redox Biology of Right-Sided Heart Failure.* Antioxidants (Basel, Switzerland), 2018. **7**(8): p. 106.
43. Bristow, M.R., et al., *The pressure-overloaded right ventricle in pulmonary hypertension.* Chest, 1998. **114**(1): p. 101S-106S.

44. Voelkel, N.F., et al., *Right ventricular function and failure: report of a National Heart, Lung, and Blood Institute working group on cellular and molecular mechanisms of right heart failure.* Circulation, 2006. **114**(17): p. 1883-1891.
45. Esfandiary, A., et al., *Protection against pressure overload-induced right heart failure by uncoupling protein 2 silencing.* Cardiovasc Res, 2019. **115**(7): p. 1217-1227.
46. Frangogiannis, N.G., *Matricellular proteins in cardiac adaptation and disease.* Physiol Rev, 2012. **92**(2): p. 635-88.
47. Singh, M., S. Dalal, and K. Singh, *Osteopontin: At the cross-roads of myocyte survival and myocardial function.* Life Sci, 2014. **118**(1): p. 1-6.
48. Zahradka, P., *Novel role for osteopontin in cardiac fibrosis.* Circ Res, 2008. **102**(3): p. 270-2.
49. Matsui, Y., et al., *Role of osteopontin in cardiac fibrosis and remodeling in angiotensin II-induced cardiac hypertrophy.* Hypertension, 2004. **43**(6): p. 1195-201.
50. Anwar, A., et al., *Osteopontin is an endogenous modulator of the constitutively activated phenotype of pulmonary adventitial fibroblasts in hypoxic pulmonary hypertension.* Am J Physiol Lung Cell Mol Physiol, 2012. **303**(1): p. L1-l11.
51. Okamoto, H., *Osteopontin and cardiovascular system.* Mol Cell Biochem, 2007. **300**(1-2): p. 1-7.
52. Waller, A.H., et al., *Osteopontin in cardiovascular disease: a potential therapeutic target.* Cardiol Rev, 2010. **18**(3): p. 125-31.
53. Singh, M., et al., *Role of osteopontin in heart failure associated with aging.* Heart failure reviews, 2010. **15**(5): p. 487-494.
54. Patarca, R., R.A. Saavedra, and H. Cantor, *Molecular and cellular basis of genetic resistance to bacterial infection: the role of the early T-lymphocyte activation-1/osteopontin gene.* Critical reviews in immunology, 1993. **13**(3-4): p. 225-246.
55. O'Regan, A. and J.S. Berman, *Osteopontin: a key cytokine in cell-mediated and granulomatous inflammation.* International journal of experimental pathology, 2000. **81**(6): p. 373-390.
56. Sørensen, E.S., T.E. Petersen, and P. Højrup, *Posttranslational modifications of bovine osteopontin: Identification of twenty-eight phosphorylation and three O-glycosylation sites.* Protein Science, 1995. **4**(10): p. 2040-2049.
57. O'Regan, A., *The Role of osteopontin in lung disease.* Cytokine & Growth Factor Reviews, 2003. **14**(6): p. 479-488.
58. Mazzali, M., et al., *Osteopontin—a molecule for all seasons.* Qjm, 2002. **95**(1): p. 3-13.
59. Icer, M.A. and M. Gezmen-Karadağ, *The multiple functions and mechanisms of osteopontin.* Clinical biochemistry, 2018.
60. Anborgh, P.H., et al., *Pre- and post-translational regulation of osteopontin in cancer.* Journal of cell communication and signaling, 2011. **5**(2): p. 111-122.
61. Lindsey, M.L., et al., *Osteopontin is proteolytically processed by matrix metalloproteinase 9.* Canadian journal of physiology and pharmacology, 2015. **93**(10): p. 879-886.
62. Christensen, B., et al., *Osteopontin is cleaved at multiple sites close to its integrin-binding motifs in milk and is a novel substrate for plasmin and cathepsin D.* J Biol Chem, 2010. **285**(11): p. 7929-37.
63. Yokosaki, Y., et al., *The integrin α9β1 binds to a novel recognition sequence (SVVYGLR) in the thrombin-cleaved amino-terminal fragment of osteopontin.* Journal of Biological Chemistry, 1999. **274**(51): p. 36328-36334.
64. Yokosaki, Y., et al., *The integrin alpha(9)beta(1) binds to a novel recognition sequence (SVVYGLR) in the thrombin-cleaved amino-terminal fragment of osteopontin.* J Biol Chem, 1999. **274**(51): p. 36328-34.
65. Ito, K., et al., *The differential amino acid requirement within osteopontin in alpha4 and alpha9 integrin-mediated cell binding and migration.* Matrix Biol, 2009. **28**(1): p. 11-9.
66. Yokosaki, Y., et al., *Distinct structural requirements for binding of the integrins αvβ6, αvβ3, αvβ5, α5β1 and α9β1 to osteopontin.* Matrix Biology, 2005. **24**(6): p. 418-427.

67. Green, P.M., et al., *Structural elements of the osteopontin SVVYGLR motif important for the interaction with α4 integrins.* FEBS letters, 2001. **503**(1): p. 75-79.
68. Rangaswami, H., A. Bulbule, and G.C. Kundu, *Osteopontin: role in cell signaling and cancer progression.* Trends Cell Biol, 2006. **16**(2): p. 79-87.
69. Zheng, W., et al., *Role of osteopontin in induction of monocyte chemoattractant protein 1 and macrophage inflammatory protein 1beta through the NF-kappaB and MAPK pathways in rheumatoid arthritis.* Arthritis Rheum, 2009. **60**(7): p. 1957-65.
70. Barry, S.T., et al., *A regulated interaction between alpha5beta1 integrin and osteopontin.* Biochem Biophys Res Commun, 2000. **267**(3): p. 764-9.
71. Yokosaki, Y., et al., *Distinct structural requirements for binding of the integrins alphavbeta6, alphavbeta3, alphavbeta5, alpha5beta1 and alpha9beta1 to osteopontin.* Matrix Biol, 2005. **24**(6): p. 418-27.
72. Bayless, K.J. and G.E. Davis, *Identification of dual α4β1 integrin binding sites within a 38 amino acid domain in the N-terminal thrombin fragment of human osteopontin.* Journal of Biological Chemistry, 2001. **276**(16): p. 13483-13489.
73. Singh, M., et al., *Osteopontin: role in extracellular matrix deposition and myocardial remodeling post-MI.* J Mol Cell Cardiol, 2010. **48**(3): p. 538-43.
74. Denhardt, D.T. and X. Guo, *Osteopontin: a protein with diverse functions.* Faseb j, 1993. **7**(15): p. 1475-82.
75. Graf, K., et al., *Myocardial osteopontin expression is associated with left ventricular hypertrophy.* Circulation, 1997. **96**(9): p. 3063-71.
76. Williams, E.B., et al., *Osteopontin expression is increased in the heritable cardiomyopathy of Syrian hamsters.* Circulation, 1995. **92**(4): p. 705-9.
77. Murry, C.E., et al., *Macrophages express osteopontin during repair of myocardial necrosis.* Am J Pathol, 1994. **145**(6): p. 1450-62.
78. Giachelli, C.M., S.M. Schwartz, and L. Liaw, *Molecular and cellular biology of osteopontin Potential role in cardiovascular disease.* Trends Cardiovasc Med, 1995. **5**(3): p. 88-95.
79. Thayer, J.M., et al., *Expression of osteopontin in the head process late in gastrulation in the rat.* J Exp Zool, 1995. **272**(3): p. 240-4.
80. Collins, A.R., et al., *Osteopontin modulates angiotensin II-induced fibrosis in the intact murine heart.* J Am Coll Cardiol, 2004. **43**(9): p. 1698-705.
81. Sam, F., et al., *Mice lacking osteopontin exhibit increased left ventricular dilation and reduced fibrosis after aldosterone infusion.* Am J Hypertens, 2004. **17**(2): p. 188-93.
82. Xie, Z., M. Singh, and K. Singh, *Osteopontin modulates myocardial hypertrophy in response to chronic pressure overload in mice.* Hypertension, 2004. **44**(6): p. 826-31.
83. Psarras, S., et al., *Regulation of adverse remodelling by osteopontin in a genetic heart failure model.* Eur Heart J, 2012. **33**(15): p. 1954-63.
84. Subramanian, V., et al., *Lack of osteopontin improves cardiac function in streptozotocin-induced diabetic mice.* Am J Physiol Heart Circ Physiol, 2007. **292**(1): p. H673-83.
85. Trueblood, N.A., et al., *Exaggerated left ventricular dilation and reduced collagen deposition after myocardial infarction in mice lacking osteopontin.* Circ Res, 2001. **88**(10): p. 1080-7.
86. Duerr, G.D., et al., *Cardioprotective effects of osteopontin-1 during development of murine ischemic cardiomyopathy.* Biomed Res Int, 2014. **2014**: p. 124063.
87. Lorenzen, J.M., et al., *Osteopontin is indispensible for AP1-mediated angiotensin II-related miR-21 transcription during cardiac fibrosis.* Eur Heart J, 2015. **36**(32): p. 2184-96.
88. Satoh, M., et al., *Myocardial osteopontin expression is associated with collagen fibrillogenesis in human dilated cardiomyopathy.* Eur J Heart Fail, 2005. **7**(5): p. 755-62.
89. Lopez, B., et al., *Osteopontin-mediated myocardial fibrosis in heart failure: a role for lysyl oxidase?* Cardiovasc Res, 2013. **99**(1): p. 111-20.
90. Berman, J.S., et al., *Altered bleomycin-induced lung fibrosis in osteopontin-deficient mice.* Am J Physiol Lung Cell Mol Physiol, 2004. **286**(6): p. L1311-8.

91. Leung, T.M., et al., *Osteopontin delays resolution of liver fibrosis.* Lab Invest, 2013. **93**(10): p. 1082-9.
92. Sahai, A., et al., *Upregulation of osteopontin expression is involved in the development of nonalcoholic steatohepatitis in a dietary murine model.* Am J Physiol Gastrointest Liver Physiol, 2004. **287**(1): p. G264-73.
93. Nagoshi, S., *Osteopontin: Versatile modulator of liver diseases.* Hepatol Res, 2014. **44**(1): p. 22-30.
94. Wu, M., et al., *Osteopontin in systemic sclerosis and its role in dermal fibrosis.* J Invest Dermatol, 2012. **132**(6): p. 1605-14.
95. Szalay, G., et al., *Osteopontin: a fibrosis-related marker molecule in cardiac remodeling of enterovirus myocarditis in the susceptible host.* Circ Res, 2009. **104**(7): p. 851-9.
96. Inoue, M. and M.L. Shinohara, *Intracellular osteopontin (iOPN) and immunity.* Immunol Res, 2011. **49**(1-3): p. 160-72.
97. Singh, K., et al., *Myocardial osteopontin expression coincides with the development of heart failure.* Hypertension, 1999. **33**(2): p. 663-70.
98. Weirather, J., et al., *Foxp3+ CD4+ T cells improve healing after myocardial infarction by modulating monocyte/macrophage differentiation.* Circ Res, 2014. **115**(1): p. 55-67.
99. McNally, E.M. and L. Mestroni, *Dilated cardiomyopathy: genetic determinants and mechanisms.* Circulation research, 2017. **121**(7): p. 731-748.
100. Renault, M.A., et al., *Osteopontin expression in cardiomyocytes induces dilated cardiomyopathy.* Circ Heart Fail, 2010. **3**(3): p. 431-9.
101. Dalal, S., et al., *Osteopontin stimulates apoptosis in adult cardiac myocytes via the involvement of CD44 receptors, mitochondrial death pathway, and endoplasmic reticulum stress.* American journal of physiology. Heart and circulatory physiology, 2014. **306**(8): p. H1182-H1191.
102. Papathanasiou, S., et al., *Tumor necrosis factor-alpha confers cardioprotection through ectopic expression of keratins K8 and K18.* Nat Med, 2015. **21**(9): p. 1076-84.
103. Dai, J., et al., *Deep sequence analysis of gene expression identifies osteopontin as a downstream effector of integrin-linked kinase (ILK) in cardiac-specific ILK knockout mice.* Circulation. Heart failure, 2014. **7**(1): p. 184-193.
104. Mizuno, Y., et al., *Improvement of cardiac function after implanting the osteopontin-derived peptide SVVYGLR in a hamster model of dilated cardiomyopathy.* Interact Cardiovasc Thorac Surg, 2015. **21**(4): p. 506-14.
105. Cabiati, M., et al., *Myocardial expression analysis of osteopontin and its splice variants in patients affected by end-stage idiopathic or ischemic dilated cardiomyopathy.* PloS one, 2016. **11**(8): p. e0160110.
106. Soejima, H., et al., *Osteopontin expression of circulating T cells and plasma osteopontin levels are increased in relation to severity of heart failure.* Circ J, 2007. **71**(12): p. 1879-84.
107. Soejima, H., et al., *Elevated plasma osteopontin levels were associated with osteopontin expression of CD4+ T cells in patients with unstable angina.* Circ J, 2006. **70**(7): p. 851-6.
108. Thygesen, K., et al., *Fourth Universal Definition of Myocardial Infarction (2018).* Glob Heart, 2018. **13**(4): p. 305-338.
109. Shirakawa, K., et al., *IL (Interleukin)-10-STAT3-Galectin-3 Axis Is Essential for Osteopontin-Producing Reparative Macrophage Polarization After Myocardial Infarction.* Circulation, 2018. **138**(18): p. 2021-2035.
110. Krishnamurthy, P., et al., *Inhibition of matrix metalloproteinases improves left ventricular function in mice lacking osteopontin after myocardial infarction.* Mol Cell Biochem, 2009. **322**(1-2): p. 53-62.
111. Zhao, X., et al., *Impairment of myocardial angiogenic response in the absence of osteopontin.* Microcirculation, 2007. **14**(3): p. 233-40.
112. Oka, T., et al., *Angiogenesis and cardiac hypertrophy: maintenance of cardiac function and causative roles in heart failure.* Circulation research, 2014. **114**(3): p. 565-571.

113. Gogiraju, R., M.L. Bochenek, and K. Schäfer, *Angiogenic Endothelial Cell Signaling in Cardiac Hypertrophy and Heart Failure.* Frontiers in Cardiovascular Medicine, 2019. **6**(20).
114. Raja, R., et al., *Hypoxia-driven osteopontin contributes to breast tumor growth through modulation of HIF1alpha-mediated VEGF-dependent angiogenesis.* Oncogene, 2014. **33**(16): p. 2053-64.
115. Ren, G., et al., *Morphological characteristics of the microvasculature in healing myocardial infarcts.* J Histochem Cytochem, 2002. **50**(1): p. 71-9.
116. Weisheit, C., et al., *Ly6Clow and not Ly6Chigh macrophages accumulate first in the heart in a model of murine pressure-overload.* PloS one, 2014. **9**(11): p. e112710.
117. Yang, G.H., et al., *Overexpression of VEGF-C attenuates chronic high salt intake-induced left ventricular maladaptive remodeling in spontaneously hypertensive rats.* Am J Physiol Heart Circ Physiol, 2014. **306**(4): p. H598-609.
118. Weisheit, C., et al., *Ly6C(low) and not Ly6C(high) macrophages accumulate first in the heart in a model of murine pressure-overload.* PLoS One, 2014. **9**(11): p. e112710.
119. Velten, M., et al., *Priming with synthetic oligonucleotides attenuates pressure overload-induced inflammation and cardiac hypertrophy in mice.* Cardiovasc Res, 2012. **96**(3): p. 422-32.
120. Lavine, K.J., et al., *Distinct macrophage lineages contribute to disparate patterns of cardiac recovery and remodeling in the neonatal and adult heart.* Proc Natl Acad Sci U S A, 2014. **111**(45): p. 16029-34.
121. Mura, M., et al., *Osteopontin Lung Expression Is a Marker of Disease Severity in Pulmonary Arterial Hypertension.* The Journal of Heart and Lung Transplantation, 2013. **32**(4, Supplement): p. S18.
122. Chen, Y.F., et al., *Atrial natriuretic peptide-dependent modulation of hypoxia-induced pulmonary vascular remodeling.* Life Sci, 2006. **79**(14): p. 1357-65.
123. Chen, Y.F., et al., *Dominant negative mutation of the TGF-beta receptor blocks hypoxia-induced pulmonary vascular remodeling.* J Appl Physiol (1985), 2006. **100**(2): p. 564-71.
124. Burke, D.L., et al., *Sustained hypoxia promotes the development of a pulmonary artery-specific chronic inflammatory microenvironment.* Am J Physiol Lung Cell Mol Physiol, 2009. **297**(2): p. L238-50.
125. Li, P., et al., *Hypoxia-responsive growth factors upregulate periostin and osteopontin expression via distinct signaling pathways in rat pulmonary arterial smooth muscle cells.* J Appl Physiol (1985), 2004. **97**(4): p. 1550-8; discussion 1549.
126. Behringer, A., et al., *Pioglitazone alleviates cardiac and vascular remodelling and improves survival in monocrotaline induced pulmonary arterial hypertension.* Naunyn Schmiedebergs Arch Pharmacol, 2016. **389**(4): p. 369-79.
127. Wang, Y., et al., *Downregulation of osteopontin is associated with fluoxetine amelioration of monocrotaline-induced pulmonary inflammation and vascular remodelling.* Clin Exp Pharmacol Physiol, 2011. **38**(6): p. 365-72.
128. Peng, X., et al., *Involvement of calcium-sensing receptors in hypoxia-induced vascular remodeling and pulmonary hypertension by promoting phenotypic modulation of small pulmonary arteries.* Mol Cell Biochem, 2014. **396**(1-2): p. 87-98.
129. Li, P., et al., *ANP signaling inhibits TGF-beta-induced Smad2 and Smad3 nuclear translocation and extracellular matrix expression in rat pulmonary arterial smooth muscle cells.* J Appl Physiol (1985), 2007. **102**(1): p. 390-8.
130. Xing, Y., et al., *MicroRNA-30c contributes to the development of hypoxia pulmonary hypertension by inhibiting platelet-derived growth factor receptor beta expression.* Int J Biochem Cell Biol, 2015. **64**: p. 155-66.
131. Yu, X., et al., *Modulation of Pulmonary Vascular Remodeling in Hypoxia: Role of 15-LOX-2/15-HETE-MAPKs Pathway.* Cell Physiol Biochem, 2015. **35**(6): p. 2079-97.
132. Picard, F., et al., *Effect of anesthesia level on murine cardiac function.* F1000Research, 2014. **3**.

133. Abdulrahman, N., et al., *Na(+)/H(+) exchanger isoform 1-induced osteopontin expression facilitates cardiac hypertrophy through p90 ribosomal S6 kinase.* Physiol Genomics, 2018. **50**(5): p. 332-342.
134. Murray, I., et al., *αv integrins on mesenchymal cells regulate skeletal and cardiac muscle fibrosis.* Nature Communications, 2017. **8**(1): p. 1118.
135. Jia, D., et al., *Osteoprotegerin disruption attenuates HySu-induced pulmonary hypertension through integrin αvβ3/FAK/AKT pathway suppression.* Circulation: Genomic and Precision Medicine, 2017. **10**(1): p. e001591.
136. Luitel, H., et al., *Pressure overload leads to an increased accumulation and activity of mast cells in the right ventricle.* Physiol Rep, 2017. **5**(6).
137. Kosanovic, D., et al., *Therapeutic efficacy of TBC3711 in monocrotaline-induced pulmonary hypertension.* Respir Res, 2011. **12**: p. 87.
138. Galiè, N., et al., *2015 ESC/ERS guidelines for the diagnosis and treatment of pulmonary hypertension: the Joint Task Force for the Diagnosis and Treatment of Pulmonary Hypertension of the European Society of Cardiology (ESC) and the European Respiratory Society (ERS): endorsed by: Association for European Paediatric and Congenital Cardiology (AEPC), International Society for Heart and Lung Transplantation (ISHLT).* European heart journal, 2015. **37**(1): p. 67-119.
139. Nadadur, R.D., et al., *Reverse right ventricular structural and extracellular matrix remodeling by estrogen in severe pulmonary hypertension.* J Appl Physiol (1985), 2012. **113**(1): p. 149-58.
140. Imoto, K., M. Okada, and H. Yamawaki, *Expression profile of matricellular proteins in hypertrophied right ventricle of monocrotaline-induced pulmonary hypertensive rats.* J Vet Med Sci, 2017. **79**(6): p. 1096-1102.
141. Bogaard, H.J., et al., *Chronic pulmonary artery pressure elevation is insufficient to explain right heart failure.* Circulation, 2009. **120**(20): p. 1951-60.
142. Klusonova, P., et al., *Chronic intermittent hypoxia induces 11beta-hydroxysteroid dehydrogenase in rat heart.* Endocrinology, 2009. **150**(9): p. 4270-7.
143. Abdalrhim, A.D., et al., *Plasma Osteopontin Levels and Adverse Cardiovascular Outcomes in the PEACE Trial.* PloS one, 2016. **11**(6): p. e0156965-e0156965.
144. Schipper, M.E., et al., *Osteopontin: a potential biomarker for heart failure and reverse remodeling after left ventricular assist device support.* J Heart Lung Transplant, 2011. **30**(7): p. 805-10.
145. Rosenberg, M., et al., *Osteopontin, a new prognostic biomarker in patients with chronic heart failure.* Circ Heart Fail, 2008. **1**(1): p. 43-9.
146. Kazimli, A.V., et al., *Myeloperoxidase, osteopontin and asymmetrical dimethylarginine as biomarkers of pulmonary hypertension severity.* European Heart Journal, 2013. **34**(suppl 1).
147. Lorenzen, J.M., et al., *Osteopontin in patients with idiopathic pulmonary hypertension.* Chest, 2011. **139**(5): p. 1010-7.
148. Rosenberg, M., et al., *Osteopontin (OPN) improves risk stratification in pulmonary hypertension (PH).* Int J Cardiol, 2012. **155**(3): p. 504-5.
149. Rhodes, C., et al., *S96 Novel biomarkers in idiopathic pulmonary arterial hypertension.* Thorax, 2010. **65**(Suppl 4): p. A44-A44.
150. Rosenberg, M., et al., *Osteopontin predicts adverse right ventricular remodelling and dysfunction in pulmonary hypertension.* Eur J Clin Invest, 2012. **42**(9): p. 933-42.
151. Hetman, O. and O. Krakhmalova. *Osteopontin as a marker of pulmonary hypertension in patients with coronary heart disease combined with chronic obstructive pulmonary disease*. in *CARDIOVASCULAR RESEARCH*. 2016. OXFORD UNIV PRESS GREAT CLARENDON ST, OXFORD OX2 6DP, ENGLAND.
152. Rubis, P., et al., *Right ventricular morphology and function is not related with microRNAs and fibrosis markers in dilated cardiomyopathy.* Cardiol J, 2017.
153. Fan, D., et al., *Differential role of TIMP2 and TIMP3 in cardiac hypertrophy, fibrosis, and diastolic dysfunction.* Cardiovasc Res, 2014. **103**(2): p. 268-80.

154. Yu, Q., et al., *IL-18 induction of osteopontin mediates cardiac fibrosis and diastolic dysfunction in mice.* Am J Physiol Heart Circ Physiol, 2009. **297**(1): p. H76-85.
155. Herum, K.M., et al., *Syndecan-4 is a key determinant of collagen cross-linking and passive myocardial stiffness in the pressure-overloaded heart.* Cardiovasc Res, 2015. **106**(2): p. 217-26.
156. Ndisang, J.F., R. Chibbar, and N. Lane, *Heme oxygenase suppresses markers of heart failure and ameliorates cardiomyopathy in L-NAME-induced hypertension.* Eur J Pharmacol, 2014. **734**: p. 23-34.
157. Li, J., et al., *Osteopontin RNA aptamer can prevent and reverse pressure overload-induced heart failure.* Cardiovasc Res, 2017. **113**(6): p. 633-643.
158. Engebretsen, K.V., et al., *Attenuated development of cardiac fibrosis in left ventricular pressure overload by SM16, an orally active inhibitor of ALK5.* J Mol Cell Cardiol, 2014. **76**: p. 148-57.
159. Kinner, B., J.M. Zaleskas, and M. Spector, *Regulation of smooth muscle actin expression and contraction in adult human mesenchymal stem cells.* Exp Cell Res, 2002. **278**(1): p. 72-83.
160. Lenga, Y., et al., *Osteopontin expression is required for myofibroblast differentiation.* Circ Res, 2008. **102**(3): p. 319-27.
161. Borgdorff, M.A., et al., *Right ventricular failure due to chronic pressure load: What have we learned in animal models since the NIH working group statement?* Heart failure reviews, 2015. **20**(4): p. 475-491.
162. Lang, M., et al., *The soluble guanylate cyclase stimulator riociguat ameliorates pulmonary hypertension induced by hypoxia and SU5416 in rats.* PloS one, 2012. **7**(8): p. e43433.
163. Andersen, S., et al., *A Pulmonary Trunk Banding Model of Pressure Overload Induced Right Ventricular Hypertrophy and Failure.* J Vis Exp, 2018(141).
164. Lindsey, M.L., et al., *Guidelines for measuring cardiac physiology in mice.* American Journal of Physiology-Heart and Circulatory Physiology, 2018. **314**(4): p. H733-H752.
165. Mura, M., et al., *Osteopontin lung gene expression is a marker of disease severity in pulmonary arterial hypertension.* Respirology, 2019.
166. Meng, L., et al., *Osteopontin plays important roles in pulmonary arterial hypertension induced by systemic-to-pulmonary shunt.* Faseb j, 2019. **33**(6): p. 7236-7251.
167. Saker, M., et al., *Osteopontin, a Key Mediator Expressed by Senescent Pulmonary Vascular Cells in Pulmonary Hypertension.* Arterioscler Thromb Vasc Biol, 2016. **36**(9): p. 1879-90.
168. Andersen, S., et al., *Right Ventricular Fibrosis.* Circulation, 2019. **139**(2): p. 269-285.
169. Crnkovic, S., et al., *Disconnect between Fibrotic Response and Right Ventricular Dysfunction.* Am J Respir Crit Care Med, 2019. **199**(12): p. 1550-1560.
170. Koop, A.M.C., et al., *Right ventricular pressure overload alters cardiac lipid composition.* Int J Cardiol, 2019. **287**: p. 96-105.
171. Ashizawa, N., et al., *Osteopontin is produced by rat cardiac fibroblasts and mediates A(II)-induced DNA synthesis and collagen gel contraction.* The Journal of clinical investigation, 1996. **98**(10): p. 2218-2227.
172. Collins, A.R., et al., *Osteopontin modulates angiotensin II- induced fibrosis in the intact murine heart.* Journal of the American College of Cardiology, 2004. **43**(9): p. 1698-1705.
173. Lenga, Y., et al., *Osteopontin expression is required for myofibroblast differentiation.* Circulation research, 2008. **102**(3): p. 319-327.
174. Xie, Z., et al., *Osteopontin Inhibits Interleukin-1β-stimulated Increases in Matrix Metalloproteinase Activity in Adult Rat Cardiac Fibroblasts ROLE OF PROTEIN KINASE C-ζ.* Journal of Biological Chemistry, 2003. **278**(49): p. 48546-48552.
175. Zohar, R., et al., *Increased cell death in osteopontin-deficient cardiac fibroblasts occurs by a caspase-3-independent pathway.* American Journal of Physiology-Heart and Circulatory Physiology, 2004. **287**(4): p. H1730-H1739.
176. López, B., et al., *Osteopontin-mediated myocardial fibrosis in heart failure: a role for lysyl oxidase?* Cardiovascular research, 2013. **99**(1): p. 111-120.

177. Shirakawa, K., et al., *IL (Interleukin)-10–STAT3–Galectin-3 Axis Is Essential for Osteopontin-Producing Reparative Macrophage Polarization After Myocardial Infarction.* Circulation, 2018. **138**(18): p. 2021-2035.
178. Valsangiacomo Buechel, E.R. and L.L. Mertens, *Imaging the right heart: the use of integrated multimodality imaging.* Eur Heart J, 2012. **33**(8): p. 949-60.
179. Marcu, C.B., A.M. Beek, and A.C. Van Rossum, *Cardiovascular magnetic resonance imaging for the assessment of right heart involvement in cardiac and pulmonary disease.* Heart, Lung and Circulation, 2006. **15**(6): p. 362-370.
180. Alfakih, K., et al., *Assessment of ventricular function and mass by cardiac magnetic resonance imaging.* European radiology, 2004. **14**(10): p. 1813-1822.

13 DECLARATION

“I declare that I have completed this dissertation single-handedly without the unauthorized help of a second party and only with the assistance acknowledged therein. I have appropriately acknowledged and referenced all text passages that are derived literally from or are based on the content of published or unpublished work of others, and all information that relates to verbal communications. I have abided by the principles of good scientific conduct laid down in the charter of the Justus Liebig University of Giessen in carrying out the investigations described in the dissertation.”

_____

Mamazhakypov, Argen

Giessen 2019

14 ACKNOWLEDGMENTS

I would like to express my sincere gratitude to all my colleagues and friends for their help and support during my PhD study.

Firstly, I would like to thank my supervisor Prof. Dr. Ralph Schermuly for allowing me to pursue PhD study in his laboratory, for the help and support during my PhD work in the laboratory.

My special gratitude goes to Dr. Akylbek Sydykov for helping me in both scientific and private life during my PhD study. Without his optimism and understanding, I would never be able to start and complete my PhD.

I also send many acknowledgements to many colleagues and friends that I have worked with over the years who offered great support. Of note, Djuro Kosanovic, Xia Tian, Astrid Weiss, Aleksandar Petrovic, Christina Vroom, Balram Neupane, Kabita Pradhan, Changwu Lu, Nabham Rai and Swathi Veeroju Sophia Bernhardt, Ewa Bieniek, Zaneta Sibinska, Gayu Viswanathan.